LBNL-41258
UC-404

ERNEST ORLANDO LAWRENCE
BERKELEY NATIONAL LABORATORY

Optical Constants of Materials in the EUV/Soft X-Ray Region for Multilayer Mirror Applications

Regina Soufli
Materials Sciences Division

RECEIVED
FEB 25 1998
OSTI

December 1997
Ph.D. Thesis

MASTER

19980427 107

DTIC QUALITY INSPECTED 3

DISCLAIMER

This document was prepared as an account of work sponsored by the United States Government. While this document is believed to contain correct information, neither the United States Government nor any agency thereof, nor The Regents of the University of California, nor any of their employees, makes any warranty, express or implied, or assumes any legal responsibility for the accuracy, completeness, or usefulness of any information, apparatus, product, or process disclosed, or represents that its use would not infringe privately owned rights. Reference herein to any specific commercial product, process, or service by its trade name, trademark, manufacturer, or otherwise, does not necessarily constitute or imply its endorsement, recommendation, or favoring by the United States Government or any agency thereof, or The Regents of the University of California. The views and opinions of authors expressed herein do not necessarily state or reflect those of the United States Government or any agency thereof, or The Regents of the University of California.

Ernest Orlando Lawrence Berkeley National Laboratory
is an equal opportunity employer.

LBNL-41258
UC-404

Optical Constants of Materials in the EUV/Soft X-Ray Region for Multilayer Mirror Applications

Regina Soufli
Ph.D. Thesis

College of Engineering
Department of Electrical Engineering and Computer Sciences
University of California, Berkeley

and

Materials Sciences Division
Ernest Orlando Lawrence Berkeley National Laboratory
University of California
Berkeley, CA 94720

MASTER

December 1997

DISCLAIMER

This report was prepared as an account of work sponsored by an agency of the United States Government. Neither the United States Government nor any agency thereof, nor any of their employees, makes any warranty, express or implied, or assumes any legal liability or responsibility for the accuracy, completeness, or usefulness of any information, apparatus, product, or process disclosed, or represents that its use would not infringe privately owned rights. Reference herein to any specific commercial product, process, or service by trade name, trademark, manufacturer, or otherwise does not necessarily constitute or imply its endorsement, recommendation, or favoring by the United States Government or any agency thereof. The views and opinions of authors expressed herein do not necessarily state or reflect those of the United States Government or any agency thereof.

DISTRIBUTION OF THIS DOCUMENT IS UNLIMITED

This work was supported in part by the ARPA Advanced Lithography Program and the Director, Office of Energy Research, Office of Basic Energy Sciences, Materials Sciences Division, of the U.S. Department of Energy under Contract No. DE-AC03-76SF00098.

Optical constants of materials in the EUV/soft x-ray region for multilayer mirror applications

by

Regina Soufli

Diploma (National Technical University of Athens, Greece) 1992

A dissertation submitted in partial satisfaction of the
requirements for the degree of
Doctor of Philosophy

in

Engineering-Electrical Engineering and Computer Sciences

in the

GRADUATE DIVISION
of the
UNIVERSITY of CALIFORNIA at BERKELEY

Committee in charge:

Professor David T. Attwood, Chair
Professor Michael A. Lieberman
Professor Daniel S. Chemla

Fall 1997

Optical Constants of Materials in the EUV/Soft X-Ray Region for Multilayer Mirror Applications

Copyright © 1997

by

Regina Soufli

The Government reserves for itself and others acting on its behalf a royalty free, nonexclusive, irrevocable, world-wide license for governmental purposes to publish, distribute, translate, duplicate, exhibit, and perform any such data copyrighted by the contractor.

The U.S. Department of Energy has the right to use this document for any purpose whatsoever including the right to reproduce all or any part thereof

Abstract

Optical constants of materials in the EUV/soft x-ray region for multilayer mirror applications

by

Regina Soufli

Doctor of Philosophy in Engineering-Electrical Engineering and Computer Sciences

University of California at Berkeley

Professor David T. Attwood, Chair

The response of a given material to an incident electromagnetic wave is described by the energy dependent complex index of refraction $n = 1 - \delta + i\beta$. In the extreme ultraviolet (EUV)/ soft x-ray spectral region, the need for accurate determination of n is driven by activity in areas such as synchrotron based research, EUV/x-ray lithography, x-ray astronomy and plasma applications. Knowledge of the refractive index is essential for the design of the optical components of instruments used in experiments and applications. Moreover, measured values of n may be used to evaluate solid state models for the optical behavior of materials. The refractive index n of Si, Mo and Be is investigated in the EUV/soft x-ray region. In the case of Si, angle dependent reflectance measurements are performed in the energy range 50 - 180 eV. The optical constants δ, β are both determined by fitting to the Fresnel equations. The results of this method are compared to the values in the 1993 atomic tables. Clean surfaces, which are critical for the studies, were obtained by UV irradiation and HF:ethanol dipping to H-passivate the surface. It is found that the values of δ in the 1993 atomic tables, which are derived through dispersion (Kramers-Kronig) calculations, are 8% to 15% high in the region 50 - 90 eV. This is attributed to missing oscillator strength

in the tabulated absorption coefficient for Si. The energy region below the Si edge is significant for the optimization of the performance of Si-based multilayer mirrors operating in this range. It is found that the method of least squares fitting reflectance data to obtain optical constants is most effective for energies well below the edge where $\delta > \beta$, while for a range of energies around and above the edge where $\delta < \beta$ the optical constants are determined with large uncertainties. Photoelectric yield measurements for Si are performed and evaluated as an alternative to the reflectance method, in the energy range where the latter becomes inefficient.

Photoabsorption measurements for the optical constants of Mo are performed on C/Mo/C foils, in the energy range 60 - 930 eV. These absorption results are combined with previous experimental data and calculations, in order to obtain the imaginary (absorptive) part of the refractive index for molybdenum in the range 1 - 30,000 eV. The real (dispersive) part of n was calculated through the Kramers-Kronig relations, using the above absorption data. Partial sum rules demonstrate that this new compilation provides an improved set of values for n covering a wider energy range, compared to the current tabulated values.

Photoabsorption measurements on Be thin films supported on silicon nitride membranes are performed, and the results are applied in the determination of the absorption coefficient of Be in the energy region 111.5 - 250 eV. More measurements are needed for the optical constants of this material, especially in the energy region of interest for EUV lithography applications, i.e. below the Be K edge (111.5 eV), where there are large discrepancies between previous experimental data.

The new results for Si and Mo are applied to the calculation of normal incidence reflectivities of Mo/Si and Mo/Be multilayer mirrors. These calculations show the importance of accurate knowledge of δ and β in the prediction and modeling of the performance of multilayer optics.

Professor David T. Attwood
Dissertation Committee Chair

All those who maintain a vacuum are more influenced by imagination than by reason. When I was a young man, I also gave in to the notion of a vacuum and atoms; but reason brought me back to the right path ...

Gottfried Wilhelm Leibniz (1646-1716)

Contents

List of Figures vi

List of Tables xiv

1 Introduction 1

2 Theory 8
- 2.1 Interactions of Radiation with Matter 8
- 2.2 Electromagnetic Description of Wave Propagation: Transmission, Reflectance and Photoemission 13
- 2.3 Dispersion Relations 23
- 2.4 Sum Rules 26

3 Instruments 31

4 Silicon 36
- 4.1 Introduction 36
- 4.2 Contamination 39
- 4.3 Sample Preparation and Surface Analysis 45
- 4.4 Reflectance Measurements 57
- 4.5 Discussion of Reflectance Data 63
- 4.6 Photoelectric Yield Measurements 68
- 4.7 Conclusions 72

5 Molybdenum 74
- 5.1 Introduction 74
- 5.2 Sample Preparation 77
- 5.3 Transmission measurements 77
- 5.4 Discussion 81
- 5.5 Mo-based Multilayer Mirrors 85
- 5.6 Conclusions 89

6 Beryllium **90**
6.1 Introduction 90
6.2 Sample Preparation 92
6.3 Transmission measurements 94
6.4 Conclusions 99

Bibliography **100**

List of Figures

1.1 Normal incidence reflectivities for Al, SiO_2 and Au are shown, calculated for unpolarized radiation in the range 30 eV - 4 keV and plotted on logarithmic axes. The reflected intensity is very small for all three materials, and decreases rapidly with energy, making it practically impossible to use common mirrors as imaging elements at near normal incidence in the EUV/soft x-ray region. 2

1.2 Bragg reflectance vs. wavelength, at near normal incidence ($\theta = 85°$), for: (a) A Mo/Be multilayer mirror with $N = 55$ layer pairs, measured at the Center for X-ray Optics (CXRO) (beamline 6.3.2, Advanced Light Source). Mo/Be mirrors are designed to operate in the energy region just below the Be K edge (111.5 eV), i.e. at wavelengths λ just longer than 11.12 nm, where Be exhibits low absorption. The peak measured reflectance for this sample is $R = 66\%$ at $\lambda = 11.57$ nm, while $R_{th} = 78\%$ is predicted by the theoretical model for a multilayer with ideal interfaces [1]. (b) A Ge/C multilayer mirror with $N = 100$ layer pairs, annealed at 550° C to enhance the reflectance. This mirror was measured using CXRO's laser-plasma source reflectometer. Ge/C mirrors are designed for the energy region just below the C K edge (284.2 eV), i.e. for wavelengths λ just longer than 4.36 nm, where the absorption of C is low. The peak measured reflectance is $R = 4.25\%$ at $\lambda = 5.01$ nm, while $R_{th} = 13\%$ is predicted by theory [2]. Due to imperfections at the layer interfaces, the measured reflectance values for both mirrors are smaller than the theoretically predicted values. Nevertheless, the measured reflectances of these multilayer mirrors are at least two orders of magnitude higher than those of a single-layer optic in the same energy range (see Fig. 1.1). 5

2.1 A schematic diagram of the incident ($\mathbf{k}$), reflected ($\mathbf{k}_r$) and refracted ($\mathbf{k}_t$) field wavevectors, for a wave traveling from vacuum to a material with refractive index $n = 1 - \delta + i\beta$. 16

2.2 Calculated reflectivity curves for s-polarized radiation and a range of β/δ values: $\beta/\delta = 0$ (solid), $\beta/\delta = 10^{-3}$ (dash), $\beta/\delta = 10^{-2}$ (dash-dot), $\beta/\delta = 10^{-1}$ (short dash), $\beta/\delta = 5 \times 10^{-1}$ (dash-dot-dot), $\beta/\delta = 1$ (triple dash), $\beta/\delta = 10$ (long dash). On the horizontal axis, the grazing angle (θ) is normalized to the critical angle $\theta_c = \sqrt{2\delta}$. Similar results for the behavior of the reflectivity as a function of β/δ can be obtained in the case of p-polarized radiation. 20

2.3 The values of (a) δ, (b) β, for Si from 30 to 30,000 eV, published in the 1993 atomic tables [3] (the β-axis scale is logarithmic). The sign reversal of δ in the region around the $L_{2,3}$ edge is shown in (a) (see Sec. 2.1). In the inset of plot (b), photoelectric yield measurements of β [4] reveal fine structure above the Si $L_{2,3}$ edge, possibly due to electron transitions from the 2p to conduction band states. Such details in the structure of β were omitted in the tabulated values. 25

2.4 Calculated sum rules for a Drude metal in the low frequency range, from ref 5. For $\omega < \omega_{p,c}$, eqs. (2.14), (2.15) have been used for the dielectric function, with $\gamma = 0.1\ \omega_{p,c}$. For $\omega > \omega_{p,c}$, $\epsilon_b = 1.05$ has been used. The frequency axis is normalized with respect to $\omega_{p,c}$ and the results for N_{eff} are normalized with respect to the number of conduction electrons $N_c = \omega_{p,c}^2 n_a e^2/m\epsilon_0$ (see eq. (2.12)). 29

3.1 A schematic diagram of the EUV/soft x-ray reflectometer operating with radiation from a laser-plasma source [6], at the Center for X-ray Optics (CXRO). 32

3.2 A schematic diagram of CXRO's beamline 6.3.2. reflectometer [7] at the Advanced Light Source (ALS). 33

3.3 Absorption spectra [4] from various gases, aiming to demonstrate the resolution capabilities of beamline 6.3.2. Data were obtained using a gas-cell detector mounted in the reflectometer chamber, and are plotted as ion current vs. photon energy. UPPER LEFT: Xe gas at 100 mTorr. The ionization lines in the spectrum represent two Rydberg series, converging to the Xe 4d absorption edge ($4d_{5/2}$ at 67.5 eV, $4d_{3/2}$ at 69.5 eV). The resolution of the experimental data was $E/\Delta E = 550$, while $(E/\Delta E)_{theoretical} = 586$. LOWER LEFT: Kr gas at 100 mTorr. The lines compose two Rydberg series, converging to the Kr 3d absorption edge ($3d_{5/2}$ at 93.8 eV, $3d_{3/2}$ at 95 eV). $E/\Delta E = 970$, $(E/\Delta E)_{theoretical} = 1098$. UPPER RIGHT: N_2 gas at 30 mTorr. The $1s \rightarrow 1\pi^*$ spectrum of N_2 is shown. The resolution in this measurement was $E/\Delta E$=7000, limited by the source size only, and was achieved with an exit slit width of 5 μm. $(E/\Delta E)_{theoretical}$ is around 9000. LOWER RIGHT: Ar gas at 80 mTorr. The Rydberg series is converging to the Ar 2p edge ($2p_{3/2}$ at 248.4 eV, $2p_{1/2}$ at 250.6 eV). $E/\Delta E = 1675$, $(E/\Delta E)_{theoretical} = 1960$. The aforementioned instrumental resolutions are considered more than adequate for the type of experiments performed at beamline 6.3.2. . 34

4.1 Calculation of $N_{eff,\beta}$ vs. photon energy for Si according to the partial sum rule of eq. (2.71), using the data for β from the 1993 atomic tables [3]. The result is $N_{eff,\beta}(\hbar\omega \rightarrow 0) = 0.2$, indicating a missing oscillator strength of 0.2 electrons. This lack in oscillator strength should cause overestimation of δ at low energies. 37

4.2 The effect of SiO_2 overlayers on the determination of the optical constants of Si is calculated for two energies: (a) 60eV and (b) 130eV. The error in the fitting of δ and β is expressed as a persentage of the tabulated values δ_0 and β_0 at each energy, and is plotted vs. SiO_2 thickness. These results are also presented in Tables 4.1, 4.2. Note that the y-axis scale in (a), (b) is different: the effect of SiO_2 surface contamination at 130 eV is much more pronounced than at 60 eV. . 43

4.3 The effect of C overlayers on the determination of the optical constants of Si is calculated for two energies: (a) 60eV and (b) 130eV. The error in the fitting of δ and β is expressed as a persentage of the tabulated values δ_0 and β_0 at each energy, and is plotted vs. C thickness. These results are also presented in Tables 4.1, 4.2. Note that the y-axis scale in (a), (b) is different: the effect of C surface contamination at 130 eV is much more pronounced than at 60 eV. 44

4.4 Outline of the x-ray photoelectron spectroscopy (XPS) method. . . . 48

4.5 Measured XPS analysis results and inferred overlayer thicknesses for a Si(111) wafer, "as received". 52

4.6 Measured XPS analysis results and inferred overlayer thicknesses for an amorphous Si sample, "as received". 53

4.7 Measured XPS analysis results and inferred overlayer thicknesses for a Si(111) wafer after UV treatment is applied. 53

4.8 Measured XPS analysis results and inferred overlayer thicknesses for a H-passivated Si(111) wafer. 54

4.9 Measured XPS analysis results and inferred overlayer thicknesses for a H-passivated Si(100) wafer. 54

4.10 Measured XPS analysis results and inferred overlayer thicknesses for a H-passivated amorphous Si sample. 55

4.11 Electron yield measurements (arbitrary units) on a Si(100) wafer at $\theta = 3$ deg (grazing angle), performed at the ALS beamline 6.3.2. Before cleaning (dashed line), there is a pronounced peak at the oxygen K edge (543.1 eV) due to the presence of the silicon oxide on the surface; the peak becomes barely visible after surface cleaning is applied (solid line). 56

4.12 The optical constants δ (◯), β (□), for a Si(100) sample measured at the ALS beamline 6.3.2. The values for δ, β (dash) from the atomic tables [3], are also shown. 58

4.13 Contour plots of S from eq. (4.1) generated with data on a Si(100) sample measured at the ALS. The energies shown are 60, 70, 80, 95, 105, 130, 150 and 180 eV in a $\delta - \beta$ axis system. Each contour area encloses the optical constant pairs fitted by the least squares algorithm within $\pm 1\sigma$ of their actual values. This is equivalent to drawing the contours containing the (δ, β) fitted with $S \leq S_{min} + 2.3$, where S_{min} is the least squared error, at each energy [8,9]. Small contour areas indicate high confidence data, while large areas indicate that a wide range of (δ, β) values meet the fitting criteria, leading to significant uncertainty. The line $\beta/\delta = 0.5$ indicates the boundary between regions of reliable and uncertain fitting. As an example, the reflectivity curves corresponding to two distant points inside the 105 eV contour, labeled 105H, 105L, are shown in Fig. 4.14. 59

4.14 Reflectivity curves calculated for s-polarized light and (i) δ = -0.00725, $\beta = 0.0105$, (dash-dot), shown as point 105H in Fig. 5, (ii) δ = -0.015, $\beta = 0.001$, (dash), shown as point 105L in Fig. 4.13. The reflectance data at 105 eV for a Si(100) sample measured at the ALS beamline 6.3.2, are also shown. 60

4.15 Fitted values of β determined from reflectance measurements at the laser-plasma source for (a) Si(111), (b) Si(100) and (c) an amorphous Si sample. Corrections ($\leq 10\%$) for the presence of residual contamination were applied. The dashed line in (a), (b), (c), represents transmission data for Si(111) from ref. 10. 65

4.16 Partial sum rules for Si, derived from the new compilation of optical constants including the experimental data presented in this work. The results demonstrate that accurate absorption data have been used and dispersion calculations have been performed self-consistently. 66

4.17 Fitted values of δ determined from reflectance measurements on a Si(111) sample measured at the laser-plasma source in the region 55 - 90 eV are shown to be in agreement with the new Kramers-Kronig calculations for δ (solid line), using a revised set of absorption data which satisfy the β-sum rule (see Fig. 4.16). Consistent experimental results for δ in this energy range were obtained from measurements on several Si(100) and Si(111) samples using both the laser-plasma source and the ALS. The Kramers-Kronig calculations from the tables in ref. 3 (dashed line) appear to overestimate the values for δ by 8 - 15%. Theoretical calculations using a linear response approximation model [11] (dash-dot line) are also shown. 67

4.18 Photoelectric yield data from a Si(100) wafer at 130 eV, taken at beamline 6.3.2 at the ALS. The y-axis is the current from the sample, normalized by its value at $\theta = 90°$. 68

4.19 (a) The results of the fitting of δ, β from the present photoelectric yield measurements on Si.The data are in quite good agreement with the revised atomic tables for Si, after the new Kramers-Kronig (KK) calculations were performed (see previous section). (b) The results of (a) are shown in detail in the region 60 - 200 eV, and photoelectric yield data from ref. 12 are superimposed. The agreement is good for data points around 95, 100, 120 and 190 eV. 71

5.1 Calculation of $N_{eff,\beta}$ vs. photon energy for Mo according to the partial sum rule of eq. (2.71), using a collection of previous experimental data and calculations for β [3,13]. The formulation of eq. (2.71) imposes that $N_{eff,\beta}(\omega \rightarrow \infty) = Z^*$ (for Mo, from eq. (2.52), $Z^* = Z - \Delta = 42 - 0.2 = 41.8$), independently of the values used for β. On the other hand, eq. (2.71) gives $N_{eff,\beta}(\omega \rightarrow 0) = 0$ only if accurate data are used, thus, the result $N_{eff,\beta}(\omega \rightarrow 0) = 2.3$ implies inaccuracies in the values for β in refs. 3, 13. 76

5.2 Transmission data from the five C/Mo/C films are shown, corresponding to molybdenum layers of 305, 460, 925, 1510 and 1900 Å each, deposited between two 145 Å thick carbon layers. 78

5.3 Fitting procedure for μ at 4 energies. The data points represent the transmission of the C/Mo/C foils plotted vs. Mo thickness. At 400 eV, high absorption prevented reliable measurements from the thick samples, so, only data from the foils with 305, 460 and 925 Å Mo thickness were used. The dashed lines represent the fit to the experimental results at each energy which yields the values of μ (cm^2/g) and T_0. . . . 79

5.4 The results for T_0 are plotted vs. photon energy. The most prominent feature is the carbon K edge at 284.2 eV. The small edge at the Ar $2p_{3/2}$ energy (248.4 eV) indicates the presence of argon in the samples. The oxygen K edge feature at 543.1 eV is attributed to a layer of photoresist left on the samples. The experimental results are fitted to a calculated transmission of 290 Å of $C_{98}Ar_2$ with 400 Å of photoresist, shown with the dashed line. 80

5.5 The new set of data for the Mo absorption coefficient from 1 eV to 30 keV is shown with the solid line. The values of μ in the range 60 - 930 eV are obtained from the present measurements. Data from refs. 13–15 are used in the low energy region (1 - 35 eV). In the rest of the spectrum, the values of the 1993 atomic tables are used with small corrections around the energy region of the present work. In the inset, the molybdenum $M_{2,3}$ structure and its deviation from the smoothed tabulated values are shown in detail. 81

5.6 The optical constants δ, β of the refractive index $n = 1 - \delta + i\beta$ are plotted vs. photon energy, using the new absorption data in the complete spectrum. (a) δ is calculated from dispersion analysis and (b) β is derived directly from μ. The values in the 1993 atomic tables [3] are also shown (dashed line) for comparison. 83

5.7 (a) The β - sum rule is shown for the new Mo absorption data (solid line) and for the data from the 1993 atomic tables (dashed line). As the photon energy approaches 0, there is an oscillator strength deficiency of 2.3 electrons in the tabulated values. The new data give the correct result of zero electrons. (b) The sum rules for ϵ_2, β, $\mathrm{Im}\{-\epsilon^{-1}\}$ are shown, using the values from the new set of data. In the low energy region, they behave exactly as predicted by the theoretical model discussed in Sec. 2.4, Fig. 2.4. The agreement of all three sum rules at the energies above the first Mo core absorption level demonstrates self-consistency among all the calculations performed. 84

5.8 The new experimental values for μ (solid line) are shown in comparison with previous reflectance data from refs. 16–18 in the wavelength range of interest for Mo/Si and Mo/Be multilayer mirror applications. The values in the 1993 atomic tables (dashed line) in this range were based on refs. 16, 17 combined with theoretical calculations [11]. 85

5.9 The envelope of peak (Bragg) reflectivities at normal incidence for an infinite multilayer stack of Mo/Si and Mo/Be is plotted vs. wavelength. The ratio of the Mo thickness to the multilayer period was 0.4 and the period was optimized for each wavelength point. The Bragg peak is shown in detail for a Mo/Si mirror with 6.87 nm period and for a Mo/Be mirror with 5.75 nm period. These theoretical calculations predict the reflectance to be 2% higher for Mo/Si and 1.8% lower for Mo/Be, compared to calculations using the values in the 1993 tables [3]. 87

5.10 Fitting of the measured reflectivity vs. wavelength (solid line), for a Mo/Si mirror (40 layer pairs) at normal incidence. This optic was fabricated by C. Montcalm and measured by C. Montcalm and D. Gaines (Lawrence Livermore National Lab), at the ALS and at the BESSY synchrotron source. The difference in the absorption values around the Bragg peak in the two sets of optical constants used for the fitting, led to two different estimates for Γ and d. A simplified model of the multilayer structure was used, just to demonstrate the effect of optical constants in the fitting of Γ and d. 88

6.1 Calculation of the sum rule of eq. (2.71) for Be, using data for β from ref. 3,19 in the range 0.06 - 30,000 eV. At $\omega \to 0$ the sum rule yields -0.05 electrons, which means there is excess oscillator strength in the absorption values for Be in some region of the spectrum. 91

6.2 Fitting of experimental reflectance data (o-points) at 90 eV from a Be/$Si_{10}N_{11}$ film deposited on a Si(111) wafer, aiming in the determination of the thickness and density of Be. The nominal thicknesses of the two layers, as reported by their manufacturers, were 632 Å for Be and 500 Å for $Si_{10}N_{11}$. The results of the fit are: For Be, thickness d = 627 Å, density ρ = 1.65 g/cm^3. For $Si_{10}N_{11}$: d = 450 Å, ρ = 2.9 g/cm^3. A BeO layer was assumed on top of Be, fitted at d = 35 Å, ρ = 1.6 g/cm^3. Native oxide SiO_2 was assumed on top of the Si wafer, fitted at d = 10 Å, ρ = 2.2 g/cm^3. For the Si wafer, ρ = 2.33 g/cm^3 was used. An interface roughness of 2 Å was assumed for all layers. The "fringes" of the reflectance curve are the result of interference among reflected rays from the various layers in the sample. 93

6.3 Transmission measurements on 4 Be samples, 90, 202, 300 and 627 Å thick respectively, supported on a silicon nitride membrane. 35 - 40 Å BeO is also expected to be present on top of Be. The presence of these additional layers in the Be samples cancels out in the determination of the absorption coefficient of Be, as explained in Sec. 5.3. Feature A in the transmission curves is attributed to the Si $L_{2,3}$ edge, B is the Be K edge, C is a feature of the silicon nitride absorption spectrum, D is the Si L_1 edge and E is the nitrogen K edge. 97

6.4 Values of the absorption coefficient of Be from different experimenters are shown, and the data from the 1993 tables are also used for comparison. All data shown in this figure are normalized, using eq. (2.23), to correspond to the tabulated value 1.8 g/cm^3 for the density of Be. The values from ref. 19 are compiled from previously published transmission measurements on evaporated Be samples [20, 21]. The measurements denoted by the solid line were performed by E. M. Gullikson at CXRO's laser-plasma source, on sputtered Be foils provided by the authors in ref. 1. 98

List of Tables

1.1 A comparison of the methods most frequently used for the determination of the optical constants δ, β is shown above. Difficulties and additional parameters involved in each method are summarized. The requirement for thin free-standing samples for the measurements and the sensitivity to the smallest amounts of contamination on the material under consideration, are problems associated with the high absorption of materials in the EUV/soft x-ray range (2nd and 3rd columns). The "surface roughness" parameter in the 4th column, refers to the sample under investigation. Some of the methods require determination of the exact thickness of the sample (6th column). In the photoelectric yield method, the energy-dependent electron escape depth (also known as "attenuation length") of the material, is an additional unknown in the fitting process, apart from δ, β. The transmission, reflectance and photoelectric yield methods are further discussed in later chapters of this thesis. 6

4.1 The effects of various thicknesses of SiO_2 and C in the determination of the optical constants of Si are calculated at 60 eV. The sixth column contains the values of the least squared error from eq. (4.1), which determines the best fitted (δ, β). The results presented in this table are also illustrated in Figs. 4.2(a), 4.3(a). 40

4.2 The effects of various thicknesses of SiO_2 and C in the determination of the optical constants of Si are calculated at 130 eV. The 3rd and 5th columns show the error in the fitting of δ and β respectively, expressed as a persentage of the tabulated values δ_0 and β_0. The sixth column contains the values of the least squared error from eq. (4.1), which determines the best fitted (δ, β). The results presented in this table are also illustrated in Figs. 4.2(b), 4.3(b). 42

Acknowledgements

This page is dedicated to the people who contributed in making this work possible:

First and foremost, my deepest gratitude goes to Eric Gullikson. During the past 4 years Eric has spared no time or effort in order to teach me everything I know today about x-ray optics. His character, talent and dedication to science have been the greatest source of inspiration for me and I consider myself really fortunate to have worked with such a gifted individual.

I would like to express my most sincere appreciation to my graduate adviser, Prof. David Attwood, for providing infinite support and guidance throughout the course of my graduate studies. I am truly indebted to Prof. Kenneth Gustafson for kindly serving in my qualifying exam committee and to Profs. Daniel Chemla and Michael Lieberman for kindly sitting in both my qualifying exam and thesis committees.

Thanks are due to Steve Irick, Frank Ogletree and Nick Palaio at LBNL for their assistance in various stages of my experimental work. I gratefully acknowledge Chris Walton for his instrumental contribution in the deposition of the molybdenum samples.

I am thankful to everyone at the Center for X-ray Optics. I could not wish for a more stimulating and enjoyable environment for me to spend my graduate years. I am especially grateful to James Underwood for many useful discussions and feedback; Paul Denham, for providing with the technique for thin foil removal; Everett Harvey and Ron Tackaberry, for their help with software; Pat Butler, Mary Holloway and Ron Sabaroff in the administrative offices as well as Mary Byrnes and Heather Brown in the EECS graduate department, for always being so kind and efficient when dealing with the paperwork; all of my office-mates, especially Raul Beguiristain and his wife Debra, Ken Goldberg and Chris Walton for their encouragement and for endless fun discussions.

This paragraph is for my friends; people whose presence has sustained me through difficult times and whose company has filled my life with great memories. I wish I could thank each of them separately, but, had I done this, the size of this section would outgrow that of my thesis! Nevertheless, I can not resist mentioning a few names.

From the UC Berkeley and Stanford campuses: Steve Delis, Yannis Kakridis, John Lygeros, Constantinos Papadias, George Pappas, Dimitris Vayanos. A very special thanks to Spyros Papadakis, for his continuing moral support and sound advice. Thanks are due to the old gang from Athens, currently scattered all over the US and overseas: Alina, Antonis, Apostolos, Eleni, Gina, Kostas, Nikos, Yannis, for their love and for always being close to me, despite the thousands of miles between us.

Finally, I would like to thank from the depths of my heart my family: my parents, Paraskevi and Nikolaos Souflis and my sister Elianna. My parents have made my journey into the world a truly exciting one and have provided for my well-being and education so far beyond their means, by sacrificing so much from themselves. They have always been my best friends, and their unconditional love remains a "constant" in the rather complicated equation of my life. For these reasons, this thesis is dedicated to my mother and to the memory of my father.

This work was supported in part by the ARPA Advanced Lithography Program and by the Office of Basic Energy Sciences, U. S. Department of Energy under Contract No. DE-AC03-76SF00098.

Chapter 1

Introduction

There has been renewed interest in recent years in the area of applications of extreme ultraviolet (EUV)/soft x-ray radiation. This energy range extends roughly from 30 eV to about 4 keV, or, in wavelength units, from λ = 400 Å down to 3 Å (these boundaries are not rigorous, since a standardized division of the spectrum does not exist). There is a wealth of research topics and applications within this regime, including microscopy, astrophysics, plasma and solid state physics, laser fusion, synchrotron related studies and lithography. The latter is a rapidly developing area of technology, aiming in the patterning and fabrication of objects with dimensions in the micron scale, such as micro-motors, zone plates (diffracting elements) and computer circuits. The current explosion of activity in the aforementioned areas has been fueled by recent advances in the development of photon sources of high brightness and spectral resolution, such as synchrotron and laser-plasma sources. Moreover, new technologies have lead to improvements in the performance of detectors, monochromator gratings, mirrors, diffractive lenses and other optical components used in this energy regime.

Since the EUV/soft x-ray portion of the spectrum coincides with the region of core electron binding energies for all materials, the main characteristic of the optical behavior of matter in this regime is strong absorption. Thus, the refractive index n has to be expressed as a complex quantity $n = 1 - \delta + i\beta$, with its imaginary (absorptive) part β comparable in magnitude to the increment δ of the real (dis-

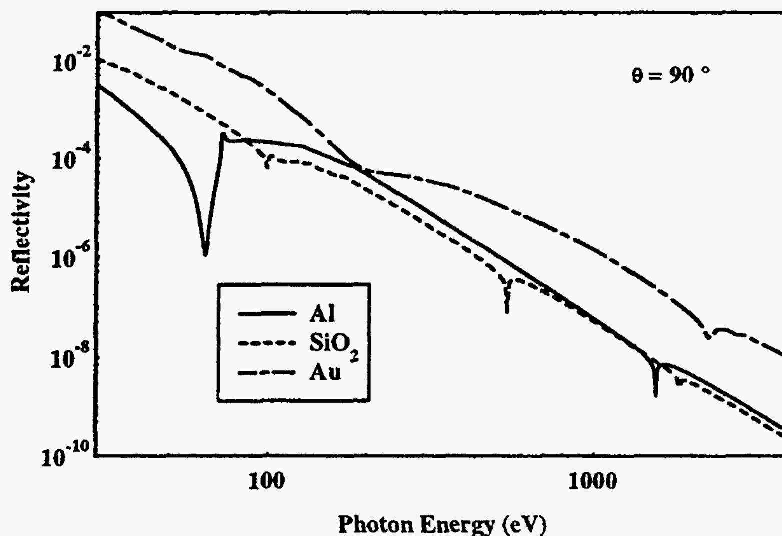

Figure 1.1: Normal incidence reflectivities for Al, SiO_2 and Au are shown, calculated for unpolarized radiation in the range 30 eV - 4 keV and plotted on logarithmic axes. The reflected intensity is very small for all three materials, and decreases rapidly with energy, making it practically impossible to use common mirrors as imaging elements at near normal incidence in the EUV/soft x-ray region.

persive) part. Furthermore, the dispersive part $1 - \delta$ is very close to 1 (δ is very small), i.e. refraction is small. Therefore, it becomes practically impossible to utilize the conventional refractive elements, such as lenses, which are used for the focusing of visible light. Instead, diffractive elements (gratings, mirrors) have to be implemented. The intensity reflectance R for radiation incident at a grazing angle θ on a perfectly smooth surface of a material with refractive index n, is given by the Fresnel equations, presented in Sec. 2.2. These equations demonstrate that the reflectance at angles θ close to 0° (grazing incidence) is close to 1, while as θ approaches 90° (normal incidence) the reflectance becomes $R = (\delta^2 + \beta^2)/4$, which is a very small number, decreasing rapidly with increasing energy to several orders of magnitude below 1, for any material in the EUV/soft x-ray regime. As an example, the normal incidence reflectivities vs. energy of Al, SiO_2 and Au are calculated in Fig. 1.1. In addition,

real surfaces suffer from imperfections (roughness) which reduce even further the theoretically predicted reflectivity. Thus, it would seem impossible to utilize reflective optics at normal incidence and the only feasible solution for imaging would be to implement them at grazing angles. However, grazing incidence systems are plagued by severe imaging defects, such as astigmatism, spherical aberration and coma. In order to correct for these problems, various optics configurations have been invented over the years, for example Kirkpatrick-Baez pairs of orthogonally placed spherical mirrors. Most of these systems involve highly aspherical surfaces, such as paraboloids and hyperboloids in Wolter-Schwarzchild systems and toroidal mirrors [22]; precise fabrication of such surfaces is considered an extremely tedious task, and often partially successful. Furthermore, dealing with roughness is particularly an issue for aspherical optics by today's manufacturing standards. On the other hand, spherical surfaces are much easier to fabricate and it can be shown that they have greatly improved imaging capabilities at normal incidence, compared to grazing incidence systems. Since a common mirror made of a single material can not reflect considerable amounts of radiation at angles θ near 90°, as shown in Fig. 1.1, there had been a quest for reflective elements with enhanced reflectivity at normal incidence. The answer to this problem came in the form of multilayer mirrors, composed of alternating layer pairs of materials with contrasting density and refractive index [23]. These mirrors operate according to the Bragg condition $n\lambda = 2d\sin\theta$, with d being the thickness of each individual layer pair. For a multilayer composed of N such pairs, the reflected field amplitude is enhanced N times due to constructive wave interference and therefore the reflected intensity is multiplied by N^2 compared to a mirror composed of a single layer pair. Today, multilayer stacks of $N \sim 10^2$ layers are routinely fabricated using magnetron sputtering and evaporation techniques, achieving intensity enhancements of 10^4 and thus approaching intensity reflectivities close to 1. In reality, the theoretically predicted values for the Bragg reflectivity can be reduced due to roughness, interdiffusion and chemical reaction between the layers (examples of reflectance measurements for two multilayer mirrors, are shown in Fig. 1.2). Therefore, by depositing these elements on spherical substrates, it became possible to utilize them efficiently for imaging purposes at normal incidence. Furthermore, due to their wavelength

selectivity (see Bragg condition), multilayer mirrors became useful as dispersive elements in x-ray spectrometers [24]. Multilayers are the optics of choice for imaging in the wavelength region 11 - 14 nm for EUV lithography. To date, the best candidates for this technology are Mo-based multilayers such as Mo/Be [1,25] and Mo/Si [26].

In order to successfully predict the performance of a multilayer mirror or any other optical element, precise knowledge of the refractive index n of its constituent materials is required. Moreover, measured values of n are needed in order to evaluate solid-state models for the optical behavior of matter. Various methods have been used by investigators for the determination of δ, β (also known as "optical constants") of materials, such as angle dependent reflectance, angle dependent electron yield, photoabsorption (transmission measurements), interferometry and ellipsometry. A database composed of experimental values for the absorption (β) taken from the literature, combined with dispersion calculations for δ, has been published in 1993 [3] and is cited throughout this work as the "1993 atomic tables"; its updated version is currently available on the World Wide Web [27]. However, there are often discrepancies among data reported by different workers on the same material. This is because measurements of the optical constants are subject to a number of difficulties inherent to the EUV/soft x-ray range. For instance, the aforementioned high absorption, which is particularly pronounced in the regions above absorption edges, prevents reliable transmission measurements unless very thin unsupported films can be fabricated and a radiation source with high photon flux and spectral purity is available. Extreme caution must be taken during the preparation of the samples under investigation, since any contamination inside the material or in the form of overlayers would seriously modify the results of the measurements, leading to errors. Furthermore, in the case of surface sensitive methods such as reflectance, it is important to use smooth and flat samples, or treat the surface roughness as an additional parameter in the fitting of experimental curves. The presence of extreme roughness would cause a great amount of the reflected signal to be scattered in non-specular directions, resulting in reflectance curves of poor quality. For all these reasons, the reported values for n in the literature often suffer from errors or uncertainties. This can be demonstrated by means of the f-sum rules, a set of integral constraints used to test the accuracy

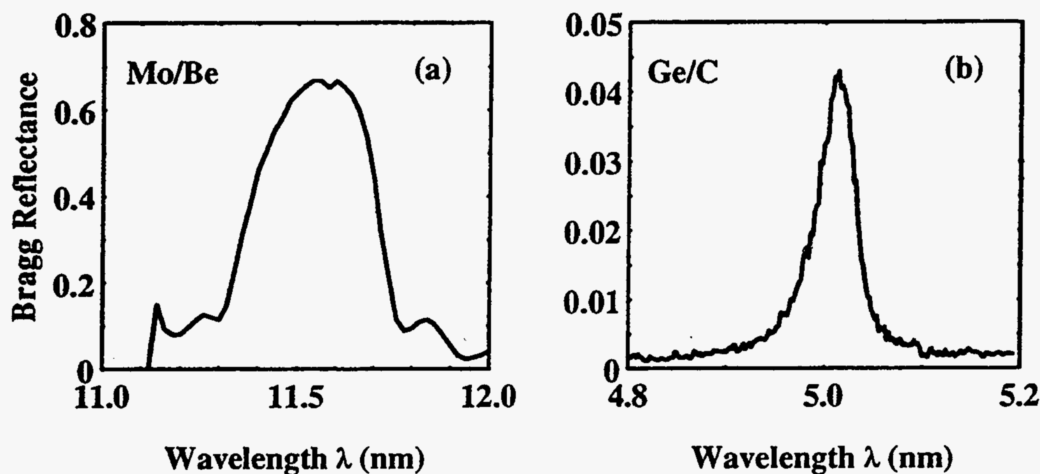

Figure 1.2: Bragg reflectance vs. wavelength, at near normal incidence ($\theta = 85°$), for: (a) A Mo/Be multilayer mirror with $N = 55$ layer pairs, measured at the Center for X-ray Optics (CXRO) (beamline 6.3.2, Advanced Light Source). Mo/Be mirrors are designed to operate in the energy region just below the Be K edge (111.5 eV), i.e. at wavelengths λ just longer than 11.12 nm, where Be exhibits low absorption. The peak measured reflectance for this sample is $R = 66\%$ at $\lambda = 11.57$ nm, while $R_{th} = 78\%$ is predicted by the theoretical model for a multilayer with ideal interfaces [1]. (b) A Ge/C multilayer mirror with $N = 100$ layer pairs, annealed at 550° C to enhance the reflectance. This mirror was measured using CXRO's laser-plasma source reflectometer. Ge/C mirrors are designed for the energy region just below the C K edge (284.2 eV), i.e. for wavelengths λ just longer than 4.36 nm, where the absorption of C is low. The peak measured reflectance is $R = 4.25\%$ at $\lambda = 5.01$ nm, while $R_{th} = 13\%$ is predicted by theory [2]. Due to imperfections at the layer interfaces, the measured reflectance values for both mirrors are smaller than the theoretically predicted values. Nevertheless, the measured reflectances of these multilayer mirrors are at least two orders of magnitude higher than those of a single-layer optic in the same energy range (see Fig. 1.1).

METHOD	HIGH ABSORPTION		ADDITIONAL PARAMETERS		
	Thin films required	Sensitive to contamination	Surface roughness	Polarization	Other
Transmission	●	●			thickness
Interferometry	●	●			thickness
Reflectance		●	●	●	
Ellipsometry		●	●	●	thickness
Photoelectric Yield		●		●	escape depth

Table 1.1: A comparison of the methods most frequently used for the determination of the optical constants δ, β is shown above. Difficulties and additional parameters involved in each method are summarized. The requirement for thin free-standing samples for the measurements and the sensitivity to the smallest amounts of contamination on the material under consideration, are problems associated with the high absorption of materials in the EUV/soft x-ray range (2nd and 3rd columns). The "surface roughness" parameter in the 4th column, refers to the sample under investigation. Some of the methods require determination of the exact thickness of the sample (6th column). In the photoelectric yield method, the energy-dependent electron escape depth (also known as "attenuation length") of the material, is an additional unknown in the fitting process, apart from δ, β. The transmission, reflectance and photoelectric yield methods are further discussed in later chapters of this thesis.

and self-consistency of the values for the optical constants of a material in the entire energy range. These tools are in fact implemented in this work, in order to evaluate the data in the 1993 atomic tables combined with published values for n in lower portions of the spectrum (visible and infrared) [13,28] and with the new measurements for n presented in this thesis. Table 1.1 summarizes the pitfalls and the additional adjustable parameters required for the determination of the refractive index, for the most common experimental methods.

The materials under investigation in this work are Si, Mo and Be; emphasis is given in the energy region 11 - 14 nm, which is of interest for EUV lithography. Sum rule tests reveal deficiencies in the available experimental data for these elements, thus demonstrating a need for improved measurements of their refractive index. The goal of this thesis is to construct an accurate, self-consistent set of values for the optical constants of these materials in a wide energy range. In the process of achieving this,

the methods of angle-dependent reflectance, angle-dependent photoelectric yield and transmission are implemented and evaluated. Furthermore, since sample quality plays a crucial role for the reliability of the measurements, a number of techniques of sample preparation and surface passivation are applied and their results are analyzed.

Chapter 2 contains the theoretical foundation for all the issues addressed in this work; a summary of the principles of interactions of radiation with matter is presented, in both the microscopic (Sec. 2.1) and the macroscopic (Sec. 2.2) domain. Special attention is given to the dispersion (Kramers-Kronig) relations (Sec. 2.3) and the sum rules (Sec. 2.4), due to their importance in the analysis of the experimental results. Chapter 3 gives an outline of the instruments utilized for the measurements and describes their capabilities. In Chapter 4, reflectance measurements for the refractive index of Si are presented. Section 4.2 gives an example of the effects of surface contamination in the results of reflectance measurements. In Section 4.3 the surface passivation procedure is described in detail; quantitative results are given through analysis of the samples with the x-ray photoelectron spectroscopy technique. In Sections 4.4, 4.5, the reliability of the reflectance data is evaluated as a function of the ratio β/δ, which emerges as an important parameter determining the effectiveness of the reflectance method. Section 4.6 contains a short series of photoelectric yield measurements in the energy region above the Si $L_{2,3}$ edge. Chapter 5 presents photoabsorption measurements for the optical constants of Mo in the range 60 - 930 eV and Chapter 6 presents Be photoabsorption measurements in the energy range from above the Be K-edge to 250 eV. For each of Si, Mo, Be the deficiencies in previously existing experimental data for n are determined by means of the sum rules. In the cases of Si and Mo, a revised set of optical constants in a wide energy range is constructed after introducing the new measurements in the existing database. The sum rules are then repeated, in order to assess the success of the new compilation.

Chapter 2

Theory

2.1 Interactions of Radiation with Matter

When radiation with photon energy $\hbar\omega$ (or wavelength $\lambda = 2\pi c/\omega$) propagates inside a medium, the response of the material depends strongly on the energy region of the interaction. For energies up to a few tens keV, electromagnetic coupling between photons and electrons is the predominant process. In this regime, the photon momentum is transferred to the atom through one of the following processes: 1) Photoelectric absorption, in which all of the photon energy is transferred to a bound electron and 2) Rayleigh (bound-electron) or Thompson (free-electron) coherent scattering, in which bound or free electrons oscillate in the presence of the incident field. At photon energies exceeding the highest characteristic absorption level (K-shell) of the material, photoelectric absorption decays and Rayleigh scattering becomes free-electron like (Thompson scattering). Above 30 - 50 keV is the region of Compton (incoherent) scattering, where the electron takes a portion of the photon momentum. Above 1 MeV, the Coulomb field of the nucleus becomes the dominant absorption mechanism and electron-positron pair creation takes place. At even higher energies, photon interactions with the nucleus become the predominant processes. Although the region of interest for EUV/x-ray optics applications extends from a few tens of eV to a few tens of keV, all the processes outside this regime must be taken into account when applying dispersion theory in order to calculate the optical properties

of a material, as is explained in Sec 2.3.

The energy range from 0 up to about 50 keV is the aforementioned region of photoelectric absorption and Rayleigh scattering. In this regime, the electrons in the atom of a material can be modeled as a collection of negatively charged oscillators bound to the nucleus through Coulomb forces. In the presence of an incident electric field $\mathbf{E}(\mathbf{r},t) = \mathbf{E}_0 \exp[-i(\omega t - \mathbf{k}\cdot\mathbf{r})]$, these particles execute harmonic motion, each having a characteristic frequency ω_j. This results in a complex dielectric function for the material having the form

$$\epsilon(\omega) = \epsilon_1(\omega) + i\epsilon_2(\omega) = 1 - \frac{4\pi r_0 n_a c^2}{\omega^2} f(\omega), \tag{2.1}$$

where n_a is the atomic density of the material, $r_0 = e^2/4\pi\epsilon_0 mc^2 = 2.818 \times 10^{-13}$ cm is the classical electron radius, m being the electron mass, and

$$f(\omega) = f_1(\omega) - if_2(\omega) = \sum_j \frac{g_j\, \omega^2}{\omega^2 - \omega_j^2 + i\gamma\omega} \tag{2.2}$$

is known as the forward atomic scattering factor. $f(\omega)$ is defined as the multiplicative correction to the field amplitude scattered by a free (Thompson) electron, applied to obtain the total amplitude coherently scattered by the whole atom; $f(\omega)$ will be expressed in units of electrons/atom throughout this work. The quantity γ in eq. (2.2) is a damping coefficient accounting for the energy loss during the harmonic motion of the electrons. g_j represents the number of electrons having resonant frequency ω_j and is known as the "oscillator strength" associated with that frequency. In the classical limit, obviously g_j is always an integer number and the sum of the oscillator strengths over all characteristic frequencies in the atom yields

$$\sum_j g_j = Z, \tag{2.3}$$

where Z is the atomic number, expressing the total number of electrons per atom. A generalization of the above law in the quantum mechanical limit states that, after the interaction of the atom with the electromagnetic field, the integral over all possible final states (including continuum states) yields

$$\int_0^\infty g(\omega)\, d\omega = Z, \tag{2.4}$$

where $g(\omega)$ here represents the oscillator strength. Eq. (2.4) is known as the Thomas-Reiche-Kuhn rule.

It is important to note that the definition of the atomic scattering factor f is meaningful only under the independent atom approximation, i.e: the assumption that the individual atoms in the material scatter independently and the total coherently scattered field amplitude is the the vector sum of the individually scattered amplitudes. This model breaks down in the low energy region (below about 50 eV) and in the vicinity of absorption edges. At the low photon energies, the optical properties are dominated by the electronic structure of the outer shells (valence or conduction bands). Around absorption thresholds, the configuration of the local environment of each atom influences its optical properties. In the regions of validity of the independent atom description, the atomic scattering factor f is in general dependent on the angle of scattering as well as the frequency ω. However, eq. (2.2) holds only for the special case of long wavelengths compared to the atomic dimensions and/or small scattering angles. In this regime, the atoms scatter as dipoles i.e. the only constructive wave interference occurs in the direction of forward and backward scattering angle. Thus, f becomes independent of the scattering angle and is equal to the forward atomic scattering factor, as given by eq. (2.2). In this limit, the concept of the atomic scattering factor can be extended to include compound materials as well. This is achieved by expressing the atomic density n_a as the sum of the atomic densities of the constituent groups of atoms

$$n_a = \sum_k n_k, \tag{2.5}$$

where n_k represents the atomic density for the atoms of type "k" in the material. Since the purpose of this work does not require otherwise, n_a in eq. (2.1) is assumed to represent only a single type of atoms. For incident photon energies $\hbar\omega$ lying between, but well separated from two absorption edges, the contribution to $f(\omega)$ comes from electrons with binding energies $\hbar\omega_j < \hbar\omega$, which respond to the incident field as if they were "free", while the contribution of electrons with $\hbar\omega_j > \hbar\omega$ is negligible ("bound electrons"). For incident photon energies well above the highest binding energy of the material (the K-shell binding energy), all electrons in the atom

respond in the same way as a system of an equal number of free electrons. Then, from eqs. (2.2), (2.3)

$$f(\omega) = \sum_j g_j = Z, \qquad \text{when } \omega \gg \omega_j \text{ for all } j, \tag{2.6}$$

i.e: the forward atomic scattering factor approaches Z in the high energy limit. These results can also be obtained using quantum mechanical calculations, where more subtle effects can be included such as exchange of oscillator strength between various absorption levels.

As a result of the phase difference between the incident and forward scattered waves, both the velocity and the amplitude of the wave transmitted from the material are altered. Macroscopically, these processes are described by the complex refractive index

$$n(\omega) = 1 - \delta(\omega) + i\beta(\omega), \tag{2.7}$$

where δ, β are known as the "optical constants" of the material at frequency ω (an electromagnetic description of the refractive index and of the role of δ, β in expressing the dispersion and absorption of a wave propagating into matter, is given in Sec. 2.2). $n(\omega)$ is defined through the dielectric function $\epsilon(\omega)$,

$$n^2(\omega) \equiv \epsilon(\omega) \Rightarrow \left\{ \begin{array}{lcl} Re\{\epsilon(\omega)\} & = & (1-\delta)^2 - \beta^2 \\ Im\{\epsilon(\omega)\} & = & 2(1-\delta)\beta \end{array} \right\} \tag{2.8}$$

and substituting $\epsilon(\omega)$ from eq. (2.1),

$$n^2(\omega) = 1 - \frac{4\pi r_0 n_a c^2}{\omega^2} f(\omega). \tag{2.9}$$

In the x-ray range (approximately above 100 eV) where $1-\delta \approx 1$ and $\beta \ll 1$, eq.(2.7) yields $n^2 \approx 1 - 2i\delta + 2i\beta$, so, from eqs. (2.2), (2.7), (2.9) the optical constants can be obtained from the real and imaginary parts of the forward atomic scattering factor through the expressions

$$\delta \approx \frac{2\pi r_0 n_a c^2}{\omega^2} f_1. \tag{2.10}$$

$$\beta \approx \frac{2\pi r_0 n_a c^2}{\omega^2} f_2. \tag{2.11}$$

It should be noted that eqs. (2.10), (2.11) are valid only within the constraints imposed for the forward atomic scattering factor, i.e. the long wavelength/small scattering angle regime and the independent atom approximation. Thus, eqs. (2.10), (2.11) are not meaningful in the low energy region, i.e. less than about 50 eV, and around absorption thresholds.

At energies below 10-20 eV, the behavior of the material is determined by its conduction or valence electrons. A strong, broad absorption is present for frequencies up to the characteristic conduction/valence electron plasma frequency

$$\omega_{p,c} = \left(\frac{n_c e^2}{m\epsilon_0}\right)^{1/2} = \left(\frac{n_a N_c e^2}{m\epsilon_0}\right)^{1/2}, \tag{2.12}$$

where n_c is the conduction/valence electron density and N_c the number of conduction/valence elecrons per atom. In this very low energy range, the single-mode Lorentz model for insulators gives a good approximation of the dielectric function [29]

$$\epsilon(\omega) \approx 1 + \frac{\omega_{p,c}^2}{\omega_0^2 + \omega^2}, \tag{2.13}$$

where the values of the parameters $\omega_{p,c}$, ω_0 can be obtained through fitting of experimental data. In the case of metals, according to the Drude model, the conduction electrons perform collective oscillations around the atom with characteristic frequency $\omega_{p,c}$ and the dielectric function is given by

$$Re\{\epsilon(\omega)\} = (1-\delta)^2 - \beta^2 \approx 1 - \frac{\omega_{p,c}^2}{\omega^2 + \gamma^2}, \tag{2.14}$$

$$Im\{\epsilon(\omega)\} = 2(1-\delta)\beta \approx \frac{\gamma\, \omega_{p,c}^2}{\omega\,(\omega^2 + \gamma^2)}. \tag{2.15}$$

For energies above $\hbar\omega_{p,c}$, as the limit of small damping losses ($\gamma \rightarrow 0$) is reached, the dielectric function of eqs. (2.14), (2.15), becomes

$$Re\{\epsilon(\omega)\} = (1-\delta)^2 \approx 1 - \frac{\omega_{p,c}^2}{\omega^2}, \tag{2.16}$$

$$Im\{\epsilon(\omega)\} \approx 0. \tag{2.17}$$

By substituting eq. (2.12) for $\omega_{p,c}$ in eq. (2.16), one recovers eq. (2.10) for δ. Thus, eq. (2.10) is consistent with the Drude model in the regime of validity of the approximations $1-\delta \approx 1$ and $\beta \ll 1$.

For energies $\hbar\omega > \hbar\omega_{p,c}$ the absorption falls off until the the region of core electron resonances is reached. In the vicinity of absorption edges, resonant Rayleigh scattering effects must be taken into account. Such effects include strong anomalous dispersion below the absorption edge, which in some cases results in a sign reversal of f_1 (and therefore δ). This is due to contributions to the total polarization of the atom coming from near-edge transitions of "bound" electrons, which are in-phase with the incident field. Favorable materials for this phenomenon must have a strong absorption edge with a sharp onset, sufficiently isolated from lower energy transitions. Furthermore, absorptions at lower energies must have sufficiently small oscillator strengths so that their out-of-phase "free electron" contribution to the polarization is overcome by the in-phase component of "bound electron" transitions. The above discussion suggests that the $L_{2,3}$ edges of the 3rd period elements such as Al, Si, P are favorable candidates for this effect. Indeed, negative f_1 (and δ) has been observed for Al [30] and Si, which is one of the materials considered in this work (see also Fig. 2.3 in Sec. 2.3).

2.2 Electromagnetic Description of Wave Propagation: Transmission, Reflectance and Photoemission

Further insight in the meaning of the refractive index $n(\omega)$ as a macroscopic quantity may be obtained through the wave equation

$$\left[\frac{\partial^2}{\partial t^2} - \frac{c^2}{n^2(\omega)}\nabla^2\right]\mathbf{E}(\mathbf{r},t) = 0, \tag{2.18}$$

having as solution a transverse electromagnetic wave of the form

$$\mathbf{E}(\mathbf{r},t) = \mathbf{E}_0 \exp\{-i(\omega t - \mathbf{k}\cdot\mathbf{r})\} \tag{2.19}$$

propagating in a material with refractive index n. From eqs. (2.18), (2.19) it is obvious that the wave propagates in the material having a complex phase velocity $\omega/k = c/n = c/(1-\delta+i\beta)$, so that the magnitude of the wavevector k is

$$k = \frac{\omega}{c}(1-\delta+i\beta). \tag{2.20}$$

After substituting the last equation into eq. (2.19) and using the fact that in the propagation direction: $\mathbf{k} \cdot \mathbf{r} = k\ r$, the expression for the propagating wave becomes

$$\mathbf{E}(\mathbf{r},t) = \mathbf{E}_0\ \exp\left\{-i\omega\left(t - \frac{r}{c}\right)\right\}\ \exp\left\{-i\frac{2\pi\delta}{\lambda}r\right\}\ \exp\left\{-\frac{2\pi\beta}{\lambda}r\right\}. \tag{2.21}$$

It is interesting to notice that, in the above equation, the term $\mathbf{E}_0 \exp\{-i\omega[t-(r/c)]\}$ represents a wave propagating in vacuum; $\exp\{-i\ 2\pi\delta r/\lambda\}$ is the phase shift due to the presence of the medium (dispersion) and $\exp\{-2\pi\beta r/\lambda\}$ is the wave amplitude decay as the wave propagates in the material (absorption). In this way, it is shown that the real $(1-\delta)$ and imaginary (β) parts of the refractive index n express the dispersive and absorptive behavior of the medium, respectively. Interferometry is the method utilizing the phase shift of an interference ("fringe") pattern between two coherent beams, in order to determine δ. However, obtaining fringes of high quality (visibility, contrast) in the x-ray range presents a number of practical difficulties, therefore, measurements of δ using the aforementioned method are often plagued by noise, which leads to uncertainties in the experimental results. On the other hand, it is quite straightforward to obtain β through the wave amplitude decay term of eq. (2.21), by means of photoabsorption (transmission) measurements. According to this method, the intensity of radiation $I \sim |E^2|$ is measured before and after photons of wavelength λ propagate inside a material of thickness r. From eq. (2.21),

$$I = I_0\ \exp\left\{-\frac{4\pi\beta}{\lambda}r\right\}, \tag{2.22}$$

where I_0 is the intensity of radiation in vacuum and the quantity $4\pi\beta/\lambda$ is termed the "linear absorption coefficient" μ_l (cm^{-1}). Another quantity widely used to express absorption is the "mass-dependent absorption coefficient"

$$\mu = \frac{\mu_l}{\rho} = \frac{4\pi\beta}{\lambda\rho} \qquad (\text{cm}^2/\text{g}), \tag{2.23}$$

where ρ (g/cm^3) is the mass density of the material. Thus, from eqs. (2.22), (2.23), in a photoabsorption measurement the fraction T of the transmitted intensity through a foil of thickness r would be given by

$$T = \frac{I}{I_0} = \exp\{-\mu\rho r\}. \tag{2.24}$$

Thus, μ can be determined through the experimental values for T and β is then obtained from eq. (2.23), assuming the mass density and the thickness of the material under consideration are accurately known. If β is known in a wide energy range, then δ may be obtained through dispersion analysis, as is discussed in the next section.

During transmission measurements, is often necessary to prevent the sample from getting exposed to air, in order to avoid degrading factors such as surface oxidation and contamination. This is achieved by depositing the film between two layers of another material, known to behave well under atmospheric conditions. In other cases, the sample has to be supported on a membrane, for stability purposes. Therefore, one needs to modify eq. (2.24) to include a many-layer system:

$$T = \exp\left\{ -\sum_i \mu_i \rho_i r_i - \mu\rho r \right\}, \tag{2.25}$$

where the subscript "i" refers to any layers present in the foil, other than the material under investigation. Eq. (2.25) can be written in a simplified form

$$T = T_0 \ \exp\{-\mu\rho r\}, \tag{2.26}$$

and will be implemented, combined with eq. (2.23), in transmission measurements of β for Mo and Be in the EUV/soft x-ray range presented in Chapters 5 and 6 of this thesis.

When radiation falls upon the interface of two materials, reflection and refraction of the incident field take place. In this paragraph, these phenomena are discussed in the x-ray domain, and the most important relations governing the electromagnetic fields are outlined. In general, let us assume a field of the form of eq. (2.19), repeated below

$$\mathbf{E}(\mathbf{r}, t) = \mathbf{E}_0 \ \exp\{-i(\omega t - \mathbf{k}\cdot\mathbf{r})\},$$

incident from vacuum ($n = 1$) on a material with $n = 1-\delta+i\beta$ at an angle of incidence θ measured from the plane of the interface ($x - y$ plane), as shown in Fig. 2.1. Then, a portion of the field will be transmitted inside the medium (refracted field) at an angle θ_t and will have the form

$$\mathbf{E}_t(\mathbf{r}, t) = \mathbf{E}_{t0} \ \exp\{-i(\omega t - \mathbf{k}_t\cdot\mathbf{r})\} \tag{2.27}$$

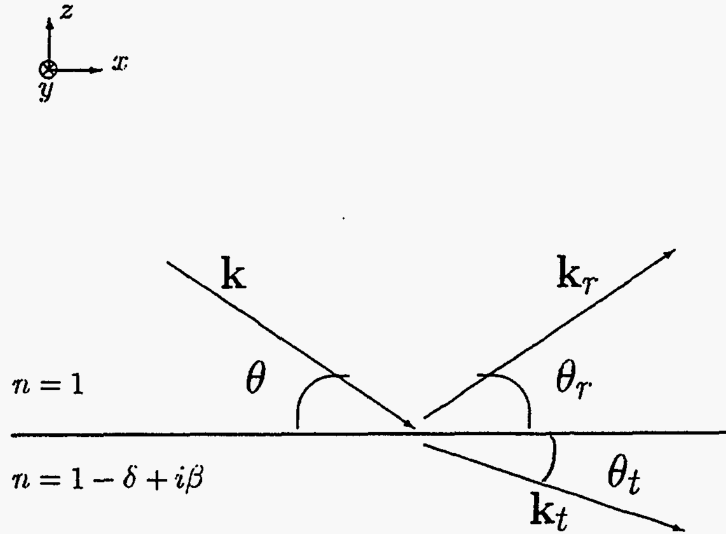

Figure 2.1: A schematic diagram of the incident ($\mathbf{k}$), reflected ($\mathbf{k}_r$) and refracted ($\mathbf{k}_t$) field wavevectors, for a wave traveling from vacuum to a material with refractive index $n = 1 - \delta + i\beta$.

and another part of $\mathbf{E}(\mathbf{r}, t)$ equal to

$$\mathbf{E}_t(\mathbf{r}, t) = \mathbf{E}_{r0}\ \exp\{-i(\omega t - \mathbf{k}_r \cdot \mathbf{r})\} \tag{2.28}$$

will be reflected back into the vacuum at an angle θ_r. Obviously, from eq.(2.20),

$$k_t = \frac{\omega}{c}\, n, \tag{2.29}$$

$$k = k_r = \frac{\omega}{c}, \tag{2.30}$$

where $\mathbf{k}, \mathbf{k}_r$ are real, $\mathbf{k}_t$ is in general a complex wavevector and all three $\mathbf{k}, \mathbf{k}_t, \mathbf{k}_r$ lie on the $x - z$ plane, termed "the plane of incidence" (see Fig. 2.1). According to the boundary conditions of Maxwell's equations, the tangential (x) components of the fields have to be continuous everywhere along the interface ($z = 0$), i.e.

$$k_x = k_{tx} = k_{rx}, \tag{2.31}$$

which, from Fig. 2.1 and eqs. (2.29), (2.30), leads to

$$\theta = \theta_r, \tag{2.32}$$

$$\cos(\theta) = n\cos(\theta_t). \tag{2.33}$$

In the regime of visible light wavelengths, n is a real number ≥ 1; then, from eq. (2.33) (known as "Snell's law") it follows that $\theta_t > \theta$, i.e. the transmitted ray is refracted closer to the surface normal than the incident ray. The effect of "total internal reflection" becomes possible at very small grazing angles of incidence (($\theta \rightarrow 0$), where the whole beam is refracted inside the second medium at an angle $\theta_t = \arccos(1/n)$ and there is no reflected ray ($\theta_r = \theta \rightarrow 0$). In the x-ray region, however, $n = 1-\delta+i\beta$, with $\delta, \beta \ll 1$ (see also previous section); thus, n is a complex number slightly less than unity and the refracted ray is bent away from the surface normal. If the imaginary part β of n is temporarily ignored (i.e. no absorption is present), then, eq. (2.33) becomes

$$\cos(\theta) = (1-\delta)\ \cos(\theta_t). \tag{2.34}$$

Therefore, if $\theta_t = 0$ is substituted in eq. (2.34), there is an angle of incidence θ_c (the "critical angle") for which there is no refracted beam and the whole incident field is reflected back into the vacuum:

$$\cos(\theta_c) = 1-\delta. \tag{2.35}$$

Since δ is a very small number in the x-ray region, θ_c is a very small angle (usually a fraction of a degree), so, the approximation $\cos(\theta_c) \simeq 1-\theta_c^2/2$ can be made, and eq. (2.35) becomes

$$\theta_c \simeq \sqrt{2\delta}. \tag{2.36}$$

Thus, for angles $\theta \leq \theta_c$, the phenomenon of "total external reflection" occurs for x-rays. If eq. (2.10) for δ is substituted in eq. (2.36),

$$\theta_c \simeq \lambda\sqrt{\frac{r_0 n_a}{\pi}\ f_1(\lambda)}. \tag{2.37}$$

Thus, the critical angle is proportional to the wavelength λ (i.e. becomes larger at the lower energies) and increases with increasing values of the real part of the atomic scattering factor $f = f_1 - if_2$ (which approaches Z at the high energies, as discussed in Sec. 2.1, eq. (2.6)). It is important to remember that the above analysis was performed for the idealized case of a non-absorbing medium ($\beta = 0$), in order to

obtain an approximate value for θ_c. In reality, $\beta > 0$ and $\mathbf{k}_t$ becomes complex, having its imaginary component only in the z-direction, since from eq. (2.31) k_{tx} has to be real. Thus,

$$k_t = n\frac{\omega}{c} = \sqrt{k_{tx}^2 + k_{tz}^2}, \qquad k_{tz} = k'_{tz} - ik''_{tz}, \tag{2.38}$$

where

$$k_{tx} = \frac{\omega}{c}\cos(\theta) \tag{2.39}$$

$$k'_{tz} = Re\{k_{tz}\} = \frac{\omega}{c}Re\left\{\sqrt{n^2 - \cos^2(\theta)}\right\} \tag{2.40}$$

$$k''_{tz} = Im\{k_{tz}\} = \frac{\omega}{c}Im\left\{\sqrt{n^2 - \cos^2(\theta)}\right\}. \tag{2.41}$$

Therefore, the field propagates inside the medium as an evanescent wave in a direction θ'_t almost parallel to the interface, where θ'_t is a real angle defined by

$$\tan(\theta'_t) = \frac{k'_{tz}}{k_{tx}} = \frac{Re\left\{\sqrt{n^2 - \cos^2(\theta)}\right\}}{\cos(\theta)} \tag{2.42}$$

and the critical angle can be obtained by solving the above equation for θ, with $\theta'_t = 0$. Furthermore, from eqs. (2.27), (2.38) it is concluded that the field amplitude undergoes absorptive losses given by $\exp\{-k''_{tz}z\}$, even for angles $\theta < \theta_c$. When solving eq. (2.42) for the critical angle, there are two cases where meaningful solutions for θ_c can not be obtained: 1) When β is comparable or greater than δ, usually in energy regions above absorption thresholds, and 2) when $\delta < 0$, around certain materials absorption edges (see discussion at the end of Sec. 2.1 on the sign reversal of δ). In these cases, the total external reflection effect vanishes and the reflected field decays fast with increasing angle of incidence θ, for every $\theta \geq 0$. These issues are further illustrated in the next paragraph, where analytic expressions and examples of reflectivity are given.

The relations for the field and intensity reflectivities can be obtained through the boundary conditions of Maxwell's equations for the electromagnetic fields at the interface between the two media. A detailed derivation of these formulae can be found in ref. 31. Two separate cases are considered: 1) $\mathbf{E}(\mathbf{r}, t)$ perpendicular to the plane of incidence (s-polarization) and 2) $\mathbf{E}(\mathbf{r}, t)$ parallel to the plane of incidence (p-polarization). The expressions for the fraction of the reflected field intensity

vs. grazing angle of incidence θ, also known as the "Fresnel coefficients" are, for s-polarized light,

$$R_s(\theta) = \left| \frac{\sin(\theta) - \sqrt{n^2 - \cos^2(\theta)}}{\sin(\theta) + \sqrt{n^2 - \cos^2(\theta)}} \right|^2 , \tag{2.43}$$

and for p-polarized light,

$$R_p(\theta) = \left| \frac{n^2 \sin(\theta) - \sqrt{n^2 - \cos^2(\theta)}}{n^2 \sin(\theta) + \sqrt{n^2 - \cos^2(\theta)}} \right|^2 , \tag{2.44}$$

where $n = 1 - \delta + i\beta$ is the refractive index of the medium. In reality, the interface between the two materials has always imperfections, described quantitatively by a roughness parameter with rms value σ. Eqs. (2.43), (2.44) should then be multiplied by the Névot-Croce factor [32] $\exp\{-4k_z k_{tz}\sigma^2\}$ which accounts for the loss of reflectivity due to scattering of radiation in directions different than the specular angle θ. From eqs. (2.43), (2.44), it is obvious that the reflectivity of a perfectly smooth surface depends only on the angle of incidence θ and the optical constants δ, β. Fig. 2.2 shows calculated reflectivity curves for a number of values for β/δ, in the case of s-polarization (eq. (2.43)). $\beta/\delta = 0$ corresponds to the idealized case of zero absorption, discussed in the previous paragraph, where the total field intensity is reflected ($R = 1$) for angles $\theta < \theta_c$ and a sharp, step-like decrease of R occurs for $\theta > \theta_c$. As the values of β/δ become larger, the effect of nonzero absorption creates a slight gradual decrease of R from unity for angles below the critical angle, and the transition from the region of total external reflection to $\theta > \theta_c$ becomes smoother compared to the step-like shape of R for $\beta = 0$. Finally, for $\beta/\delta \geq 1$, the reflectance curves become exponential-like, decreasing sharply from $R(\theta = 0) = 1$, therefore, total external reflection practically does not exist for this range of β/δ values, as was mentioned in the previous paragraph in the discussion of eq. (2.42). Eqs. (2.43), (2.44) will be used in Ch. 4 to determine the optical constants δ, β of Si by means of least-squares fitting of angle-dependent reflectance measurements; it will be shown that the behavior of R as a function of the ratio β/δ, illustrated in Fig. 2.2, has a serious effect on the ability of the fitting algorithm to extract accurately the values of δ, β, from experimental reflectance data.

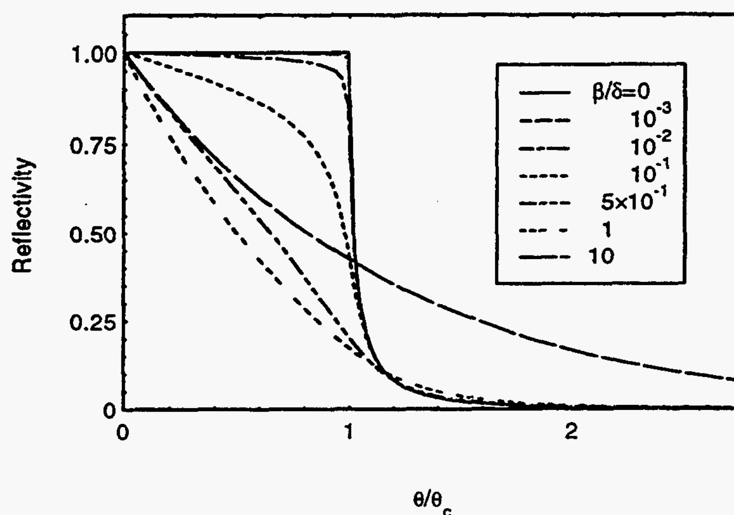

Figure 2.2: Calculated reflectivity curves for s-polarized radiation and a range of β/δ values: $\beta/\delta = 0$ (solid), $\beta/\delta = 10^{-3}$ (dash), $\beta/\delta = 10^{-2}$ (dash-dot), $\beta/\delta = 10^{-1}$ (short dash), $\beta/\delta = 5 \times 10^{-1}$ (dash-dot-dot), $\beta/\delta = 1$ (triple dash), $\beta/\delta = 10$ (long dash). On the horizontal axis, the grazing angle (θ) is normalized to the critical angle $\theta_c = \sqrt{2\delta}$. Similar results for the behavior of the reflectivity as a function of β/δ can be obtained in the case of p-polarized radiation.

One of the secondary processes occuring during an interaction of x-rays with matter, is photoemission. When the surface of a material is irradiated, electrons are excited inside the solid and, after a series of elastic and inelastic scattering events along their path, they migrate to the surface; then, if they have sufficient energy to overcome the potential barrier, they escape in the vacuum. Pepper [33] has given a detailed analysis of the photoemission from a film of thickness d on a semi-infinite substrate and the results are extended to $d \to \infty$ for the case of a bulk material. The central assumption in the theoretical model presented in ref. 33 is that any volume element in the solid is contributing a number of emitted electrons that is proportional to the number of photons absorbed inside that volume. The probability that an electron will be excited at a depth z below the surface (see Fig. 2.1) and enter the vacuum is given by $C \exp\{-z/L\}$, where C is an energy-dependent parameter describing the probability of success for the processes leading to emission of an electron from the solid (absorption of an incident photon by an electron, excitation of the electron at states above the vacuum level, penetration of the surface potential barrier). L is the energy-dependent electron attenuation length (or escape depth), describing all the physical mechanisms that can lead to de-excitation of the electron, for example, collisions with other electrons or phonons. By assuming that the motion of the electron becomes random after the excitation, C, L can be considered independent of the direction of the electric field. For a field incident at grazing angle θ, as shown in Fig. 2.1, on the surface of a film of thickness d on top of a semi-infinite substrate, the quantity used to describe the number of electrons emitted per incident photon is the quantum yield

$$Y(\theta) = C \int_0^d \exp\{-z/L\}\ \eta(z,\theta)\ dz = C\ F(\theta). \tag{2.45}$$

$\eta(z,\theta)$ is the volume absorptance of the material at depth z

$$\eta = \frac{-\nabla \cdot [(1/2)\ Re\{\mathbf{E} \times \mathbf{H}^*\}]}{I_0}, \tag{2.46}$$

where the nominator is recognized as the negative divergence of the Poynting vector, i.e. the energy flux into a unit volume of the solid, and I_0 represents the incident photon flux. It is convenient to define the relative gain

$$G(\theta) = \frac{Y(\theta)}{Y(\theta = 90^\circ)} = \frac{F(\theta)}{F(\theta = 90^\circ)}, \tag{2.47}$$

so that the dependence on the parameter C of eq. (2.45) cancels out. Ref. 33 contains a full manipulation of of eqs. (2.45)-(2.47) using electromagnetic laws. The result for $F(\theta)$ when the thickness d of the film goes to infinity (i.e. for a semi-infinite medium), written in terms of quantities derived in the previous paragraphs, is

$$F(\theta) = \frac{1 - R(\theta)}{1 + [L\ 2k''_{tz}(\theta)]^{-1}}, \qquad (2.48)$$

so that the relative gain of eq. (2.47) becomes

$$G(\theta) = \frac{1 - R(\theta)}{1 - R(90°)} \frac{1 + [L\ 2k''_{tz}(90°)]^{-1}}{1 + [L\ 2k''_{tz}(\theta)]^{-1}}. \qquad (2.49)$$

In the above equations, $R(\theta)$ is the reflectivity given by one of eqs. (2.43), (2.44) and k''_{tz} is the lossy component of the wavenumber k_t of the transmitted field, given by eq. (2.41) (note that $2k''_{tz}(90°) = 4\pi\beta/\lambda = \mu_l$, which is the linear absorption coefficient defined in eq. (2.23)). From eq. (2.49) it is concluded that the relative gain $G(\theta)$ depends only on the optical constants δ, β (included in the expressions for R and k''_{tz}) and on the escape depth L. Angle-dependent photoelectric yield measurements have been used in the literature [12,34] to determine the optical constants of a material, through fitting of experimental $G(\theta)$ curves, with δ, β, L as fitting parameters. New measurements are going to be presented in Sec. 4.6 for Si, around the $L_{2,3}$ edge energy region.

2.3 Dispersion Relations

From the above analysis it is concluded that the complex atomic scattering factor f represents the physical response of a system (the material) to a stimulus (the electromagnetic field of frequency ω). In such cases, when the system is linear, stable and causal, it can be shown [35] that the real (f_1) and imaginary (f_2) parts of the response function f are related through dispersion expressions, known as the "Kramers-Kronig" relations:

$$f_1(\omega) - Z^* = -\frac{2}{\pi}\int_0^\infty \frac{u f_2(u)}{u^2 - \omega^2} du, \tag{2.50}$$

$$f_2(\omega) = \frac{2\omega}{\pi}\int_0^\infty \frac{f_1(u) - Z^*}{u^2 - \omega^2} du, \tag{2.51}$$

where $Z^* = Z - \Delta$ is the atomic number reduced by the relativistic correction

$$\Delta \approx (Z/82.5)^{2.37}, \tag{2.52}$$

arising due to a relativistic increase in mass experienced by the core electrons, especially in heavy elements. These electrons have a slower response to the incident field which results in reduced oscillator strength. The expression of eq. (2.52) is given in ref. 3 by fitting tabulated values for Δ as a function of Z [36]. Eq. (2.50) demonstrates that knowledge of f_2 in the whole range of frequencies can determine f_1 at a frequency ω and vice versa. Since direct measurements of the dispersive part f_1 are relatively difficult, it is common to determine f_2 through absorption measurements, and then calculate f_1 from eq. (2.50).

A comprehensive compilation of x-ray data for all materials was published [3] by Henke, Gullikson and Davis in 1993 and will be referred to as the "1993 atomic tables" throughout this work. These tables use a compilation of published experimental data for the absorption for elements with atomic number $Z = 1$ to $Z = 92$, interpolated with the aid of a theoretical model [11], to determine f_2 in the range 10 - 30,000 eV. The real part is then calculated through dispersion (Kramers-Kronig) analysis, using eq. (2.50). The optical constants δ, β of the refractive index $n = 1 - \delta + i\beta$ can then be determined from eqs. (2.10), (2.11). An example of the published optical constants

for Si in the 1993 atomic tables is shown in Fig. 2.3. The updated atomic tables and related calculations are currently available in the World Wide Web [27].

It is important to keep in mind that the values for the refractive index in the 1993 atomic tables should be used with caution, since they have been derived in the independent atom approximation and the long wavelength/small scattering angle regime, as discussed in Sec. 2.1. Thus, calculated values at the very low energies, below about 50 eV, may be inaccurate. Furthermore, it is expected that the interpolations and calculations used for the tabulated values smooth out possible fine structure surrounding absorption thresholds, in the regions where detailed measurements are not available. An example of this effect is demonstrated in Fig. 2.3(b), where the values of β for Si from the 1993 tables are shown superimposed to experimental data for β [4] obtained through detailed photoemission measurements in the region of the Si $L_{2,3}$ edge. The same effect will be observed later in this thesis in the region around the Mo $M_{4,5}$ edge, in the light of the new measurements presented in Chapter 5.

The main weakness of the method implemented in the 1993 atomic tables for the determination of optical constants, is the requirement of accurate knowledge of the imaginary (absorptive) part of f in the entire spectrum, in order to calculate by means of eq. (2.50) the real (dispersive) part at a single frequency ω. This means that possible errors in the absorption measurements or calculations in some region of the spectrum will be reflected in the dispersion calculations at all frequencies. In particular, eq. (2.50) which is known as the "x-ray form" [37] of the Kramers-Kronig relations suffers from systematic errors in the calculation of f_1 at the low energies. This issue is discussed in Sec 4.1 for the case of Si. The methods for evaluating a set of optical constants are discussed in the next section.

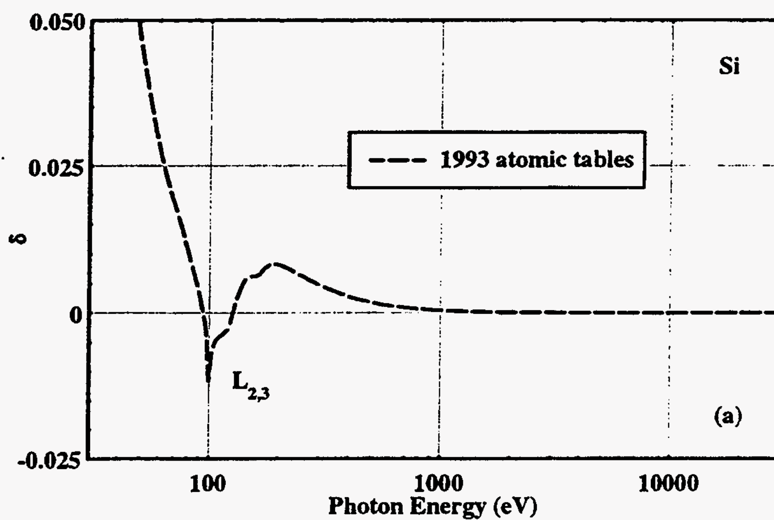

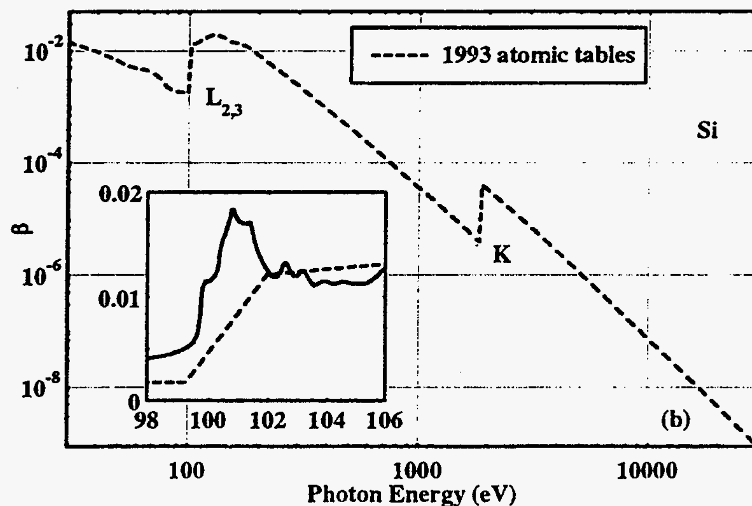

Figure 2.3: The values of (a) δ, (b) β, for Si from 30 to 30,000 eV, published in the 1993 atomic tables [3] (the β-axis scale is logarithmic). The sign reversal of δ in the region around the $L_{2,3}$ edge is shown in (a) (see Sec. 2.1). In the inset of plot (b), photoelectric yield measurements of β [4] reveal fine structure above the Si $L_{2,3}$ edge, possibly due to electron transitions from the 2p to conduction band states. Such details in the structure of β were omitted in the tabulated values.

2.4 Sum Rules

In the above discussions it was explained that several types of measurements and calculations in a wide energy range may be involved in the determination of the optical constants δ, β of a material in the entire spectrum. The accuracy and self-consistency of such a composite set of optical data may be assessed through a series of integral constraints, termed in the literature as the "f-sum rules" [5]:

$$\int_0^\infty u\ \epsilon_2(u)\ du = \frac{\pi}{2}\ \omega_p^2, \tag{2.53}$$

$$\int_0^\infty u\ \beta(u)\ du = \frac{\pi}{4}\ \omega_p^2, \tag{2.54}$$

$$\int_0^\infty u\ Im\{-\epsilon^{-1}(u)\}\ du = -\ \frac{\pi}{2}\ \omega_p^2, \tag{2.55}$$

where

$$\omega_p^2 = \frac{n_e e^2}{m\epsilon_0} = Z^* \frac{n_a e^2}{m\epsilon_0} \tag{2.56}$$

is the squared plasma frequency, and n_e, n_a have been defined in Sec. 2.1 as the electron and atomic densities of the material, respectively.

Eq. (2.53) is a direct consequence of the quantum mechanical Thomas-Reiche-Kuhn rule of eq. (2.4), since the oscillator strength $g(\omega)$ is related to the imaginary part $\epsilon_2(\omega)$ of the dielectric function through [38]

$$g(\omega) = \frac{2m\epsilon_0}{n_a \pi e^2}\ \omega\ \epsilon_2(\omega). \tag{2.57}$$

Thus, if eq. (2.57) is substituted in eq. (2.4), the result is

$$\int_0^\infty \frac{2m\epsilon_0}{n_a \pi e^2}\ \omega\ \epsilon_2(\omega)\ d\omega = Z^* \Rightarrow \int_0^\infty \omega\ \epsilon_2(\omega)\ d\omega = \frac{\pi}{2}\ \frac{Z^* n_a e^2}{m\epsilon_0} = \frac{\pi}{2}\ \omega_p^2,$$

which is the sum rule of eq. (2.53). Refs. 29, 39 present a rigorous derivation of eqs. (2.54), (2.55) by means of the dynamical, inertial and causality laws governing the short-time response of the material to an external field perturbation. Thus, the sum rules may be viewed as the frequency-space equivalent of the time-dependent dynamical laws of motion.

Another formulation of the sum rules can be obtained by substituting eq. (2.56) in eqs. (2.53)-(2.55):

$$\frac{2}{\pi}\frac{m\epsilon_0}{n_a e^2}\int_0^\infty u\ \epsilon_2(u)\ du = Z^*, \tag{2.58}$$

$$\frac{4}{\pi}\frac{m\epsilon_0}{n_a e^2}\int_0^\infty u\ \beta(u)\ du = Z^*, \tag{2.59}$$

$$\frac{2}{\pi}\frac{m\epsilon_0}{n_a e^2}\int_0^\infty u\ Im\{-\epsilon^{-1}(u)\}\ du = Z^*. \tag{2.60}$$

One may notice that eqs. (2.53)-(2.55) and (2.58)-(2.60) integrate from $\omega = 0$ to $\omega = \infty$, therefore, they can not reveal the source of an oscillator strength defect in an absorption spectrum, composed of several measurements and calculations. Thus, it would be practical to use eqs. (2.58)-(2.60) in their partial form [5]

$$N_{eff,\epsilon_2}(\omega) = \frac{2}{\pi}\frac{m\epsilon_0}{n_a e^2}\int_0^\omega u\ \epsilon_2(u)\ du, \tag{2.61}$$

$$N_{eff,\beta}(\omega) = \frac{4}{\pi}\frac{m\epsilon_0}{n_a e^2}\int_0^\omega u\ \beta(u)\ du, \tag{2.62}$$

$$N_{eff,\epsilon^{-1}}(\omega) = \frac{2}{\pi}\frac{m\epsilon_0}{n_a e^2}\int_0^\omega u\ Im\{-\epsilon^{-1}(u)\}\ du. \tag{2.63}$$

The above equations relate the effective number of electrons in the atom N_{eff,ϵ_2}, $N_{eff,\beta}$, $N_{eff,\epsilon^{-1}}$, contributing to the optical properties of a material up to frequency ω, to the dissipative (imaginary) parts of its dielectric function ϵ, refractive index n and energy-loss function ϵ^{-1}, respectively. As will be shown in the next paragraph, $N_{eff,\epsilon_2}, N_{eff,\beta}, N_{eff,\epsilon^{-1}}$ are not exactly equivalent quantities, since they account for slightly different physical processes: ϵ_2 is associated with the rate of energy dissipation from an electromagnetic wave, β with the amplitude decrease of the wave and $Im\{\epsilon^{-1}\}$ (known as the "energy-loss function") with the energy lost by fast charged particles going through the medium.

The behavior of the partial sum rules in eqs. (2.61)-(2.63) in the low energy range, where the refractive index n is greater than 1 (see Sec. 2.1), can be understood if $\epsilon_2, Im\{-\epsilon^{-1}\}$ are expressed in terms of the optical constants δ, β. Using eq. (2.8),

$$\epsilon_2 = 2\ (1-\delta)\ \beta, \tag{2.64}$$

$$Im\{-\epsilon^{-1}\} = \frac{1-\delta}{[(1-\delta)^2+\beta^2]^2}. \tag{2.65}$$

Thus, since for the low energies $(1-\delta) \gg 1$, it is obvious from eqs. (2.61), (2.64) and (2.63), (2.65) that

$$N_{eff,\epsilon_2} > N_{eff,\beta} > N_{eff,\epsilon^{-1}}. \tag{2.66}$$

As a result, N_{eff,ϵ_2} is much more sensitive to optical data from the lower portions of the spectrum, such as the infrared region. Analysis of the sum rules at higher energies, above the conduction/valence plasma frequency $\omega_{p,c}$ (see eq.(2.12)), is possible if the various absorption levels in the atom of the material are well separated from each other. For energies well below the onset of the core level excitations but much higher than $\hbar\omega_{p,c}$, the conduction/valence electrons can be regarded as imbedded in a transparent medium consisting of the ion cores with a real dielectric function ϵ_b. In this regime, it has been shown in ref. 5 that the dielectric function $\epsilon(\omega)$ of the material may be expanded in a series, with ϵ_b taken as constant, and the results for the finite f-sum rules are

$$N_{eff,\epsilon_2} \approx \frac{m\epsilon_0}{n_a e^2}\,\omega_{p,c}^2 \qquad \omega_{p,c} < \omega < \omega_1, \tag{2.67}$$

$$N_{eff,\beta} \approx \frac{m\epsilon_0}{n_a e^2}\,\frac{\omega_{p,c}^2}{\epsilon_b^{1/2}} \qquad \omega_{p,c} < \omega < \omega_1, \tag{2.68}$$

$$N_{eff,\epsilon^{-1}} \approx \frac{m\epsilon_0}{n_a e^2}\,\frac{\omega_{p,c}^2}{\epsilon_b^2} \qquad \omega_{p,c} < \omega < \omega_1, \tag{2.69}$$

where ω_1 represents the lowest core electron resonant frequency. Therefore, the ordering of inequality (2.66) is maintained above the conduction plasma frequency $\omega_{p,c}$ as well. The three sums rise monotonically with $N_{eff,\epsilon_2} > N_{eff,\beta} > N_{eff,\epsilon^{-1}}$, reaching gradually rising plateaus until the onset of the lowest core level absorption, where the valence electron oscillator strength should be completely exhausted for all three sum rules. From there on, if the optical constants have been obtained in a consistent manner, eqs. (2.61)-(2.63) should draw together until they reach asymptotically the value $N_{eff,\epsilon_2} = N_{eff,\beta} = N_{eff,\epsilon^{-1}} = Z^*$ for $\omega \rightarrow \infty$. The behavior of the three sum rules of eqs. (2.61)-(2.63) in the low energy range is illustrated in Fig. 2.4, borrowed from the literature [5]. Calculations of the sum rules are shown for a Drude metal, assuming the model of the conduction/valence electrons in a dielectric medium of the ion cores with $\epsilon_b = 1.05$.

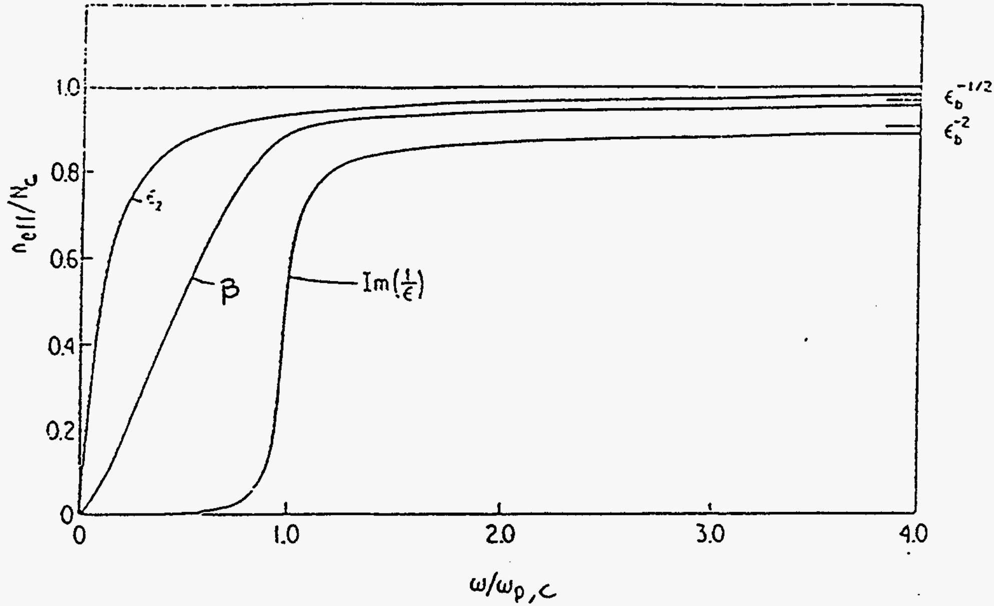

Figure 2.4: Calculated sum rules for a Drude metal in the low frequency range, from ref 5. For $\omega < \omega_{p,c}$, eqs. (2.14), (2.15) have been used for the dielectric function, with $\gamma = 0.1\ \omega_{p,c}$. For $\omega > \omega_{p,c}$, $\epsilon_b = 1.05$ has been used. The frequency axis is normalized with respect to $\omega_{p,c}$ and the results for N_{eff} are normalized with respect to the number of conduction electrons $N_c = \omega_{p,c}^2 n_a e^2/m\epsilon_0$ (see eq. (2.12)).

In the following sections, the partial sum rules will be used as a guide for the evaluation of the experimental data and dispersion calculations for Si, Mo and Be presented in the 1993 atomic tables. The values of $N_{eff,\epsilon_2}, N_{eff,\beta}, N_{eff,\epsilon^{-1}}$ will be determined using the expressions

$$N_{eff,\epsilon_2}(\omega) = Z^* - \frac{2}{\pi}\frac{m\epsilon_0}{n_a e^2}\int_\omega^\infty u\ \epsilon_2(u)du, \tag{2.70}$$

$$N_{eff,\beta}(\omega) = Z^* - \frac{4}{\pi}\frac{m\epsilon_0}{n_a e^2}\int_\omega^\infty u\ \beta(u)\ du, \tag{2.71}$$

$$N_{eff,\epsilon^{-1}}(\omega) = Z^* - \frac{2}{\pi}\frac{m\epsilon_0}{n_a e^2}\int_\omega^\infty u\ Im\{-\epsilon^{-1}(u)\}\ du, \tag{2.72}$$

which are equivalent to eqs. (2.61)-(2.63) combined with eqs. (2.58)-(2.60). The form "$\int_\omega^\infty$" (as opposed to "$\int_0^\omega$" in eqs. (2.61)-(2.63)) is used for the calculation of the partial

sum rules in order to be consistent with the "x-ray form" of the Kramers-Kronig relations (eq. (2.50)), which has been implemented in the 1993 atomic tables to calculate f_1. This formulation utilizes Z^* and is pinned at infinity, i.e. it is insensitive to inaccuracies in the experimental data when calculating $N_{eff,\epsilon_2}(\omega), N_{eff,\beta}(\omega), N_{eff,\epsilon^{-1}}(\omega)$ (eqs. (2.70)-(2.72)), or $f_1(\omega)$ (eq. (2.50)), for $\omega \rightarrow \infty$ (see also discussion at the end of Sec. 2.3). Indeed, eqs. (2.70)-(2.72) guarantee that $N_{eff,\epsilon_2} = N_{eff,\beta} = N_{eff,\epsilon^{-1}} = Z^*$ for $\omega \rightarrow \infty$, regardless of possible defects in the data used for $\epsilon_2, \beta, Im\{\epsilon^{-1}\}$. On the other hand, the results of eqs. (2.70)-(2.72) at $\omega \rightarrow 0$ depend on the values of $\epsilon_2, \beta, Im\{\epsilon^{-1}\}$. Thus, as ω goes to 0, the sum rules of eqs. (2.70)-(2.72) provide the test for the quality of the optical data used in the entire energy range. Accurate data should yield $N_{eff,\epsilon_2}, N_{eff,\beta}, N_{eff,\epsilon^{-1}} \rightarrow 0$ as $\omega \rightarrow 0$. Otherwise, non-zero results at $\omega \rightarrow 0$ would indicate missing or excess oscillator strength in some region of the spectrum, due to experimental errors or inconsistent dispersion calculations. Since the partial sum rule for β in eq. (2.71) depends only on the imaginary (absorptive) part of the refractive index, it will be used to characterize the absorption data in the 1993 atomic tables, independently of the Kramers-Kronig calculations. Eqs. (2.70), (2.72) will be implemented to examine both real and imaginary parts of the refractive index n.

Chapter 3

Instruments

The two instruments that were used for the measurements presented in this thesis are outlined below:

1) The EUV/soft x-ray reflectometer at CXRO is described in detail in ref. 6. The instrument, shown in Fig. 3.1, includes a laser-plasma source and a spherical grating monochromator, producing continuously tunable radiation in the range 30<E<300 eV. The radiation source is a laser produced plasma; 532 nm light pulses from a Continuum, Inc. Model YG661-10 Nd:YAG laser are focused on a Au target rod, forming a plasma. The laser operates at 10 Hz and delivers pulses of 8 ns duration and 330 mJ energy/pulse. A fraction of the radiation produced by the plasma in the target chamber is collected by a high throughput monochromator. The optical components of the monochromator include a cylindrical bent glass premirror, an adjustable aperture (baffle) determining the horizontal beam size, a fixed line spacing spherical grating and a fixed exit slit. Two interchangeable gratings are available, 800 and 2400 lines/mm in order to cover the energy range from 30 to 300 eV. With a 300 lines/mm grating the range can be extended down to 10 eV. Wavelength is scanned by rotating the grating about an axis parallel to the ruling using a sine bar drive. The exit slit is 12 mm long and its width can be adjusted from 10 to 300 μm. After the exit slit, the beam passes through a filter chosen to block the second harmonic of the energy, i.e. $\lambda/2$ of the wavelength λ selected by the monochromator. An I_0 detector is used to monitor the photon flux, so as to permit a correction of

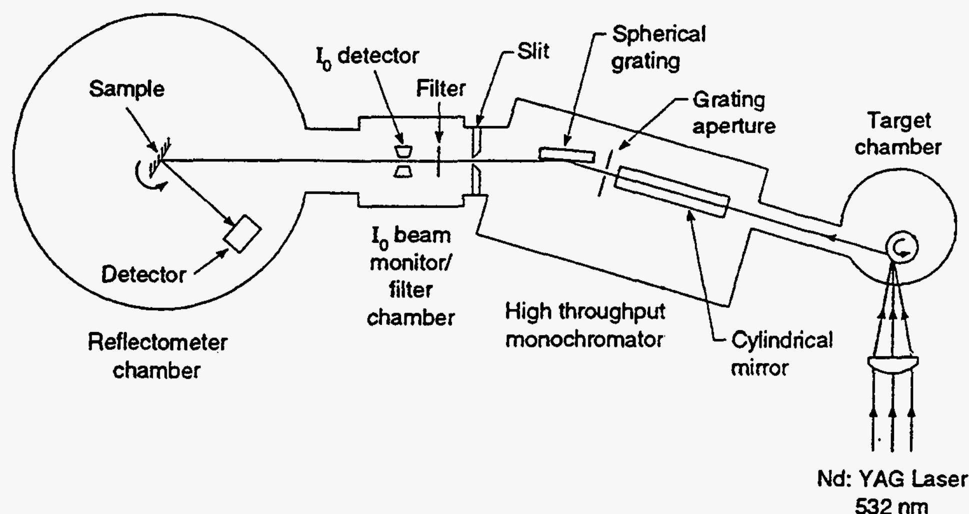

Figure 3.1: A schematic diagram of the EUV/soft x-ray reflectometer operating with radiation from a laser-plasma source [6], at the Center for X-ray Optics (CXRO).

the "shot-to-shot" noise from the source. Finally, the beam enters the reflectometer chamber (10^{-5} Torr pressure), where the sample is mounted on a holder having the ability to rotate and move in three dimensions and a detector collects the signal after the light has interacted with the sample. The sample position is reproducible to ± 4 μm and the minimum angle step size is 0.005°. The horizontal beam size at the sample can be varied from 30 mm down to less than 1 mm (according to the baffle size), and a vertical beam size of 0.3 mm FWHM has been measured, with the glass mirror focused at the sample. With the full horizontal beam accepted this system produces 2×10^8 photons/pulse at the output of the monochromator, with 1% bandwidth at 100 eV. The resolving power $E/\Delta E$ of the system varies from 100 to 500, depending on exit slit width and grating aperture. Polarization measurements have shown that the laser plasma source emits largely unpolarized radiation (to at least 95% in intensity), in the energy range of interest for the measurements presented in this work.

2) Beamline 6.3.2 at the ALS is described in detail in ref. 7. This beamline, shown in Fig. 3.2, uses radiation from a bending magnet in the energy range $50<E<1300$ eV.

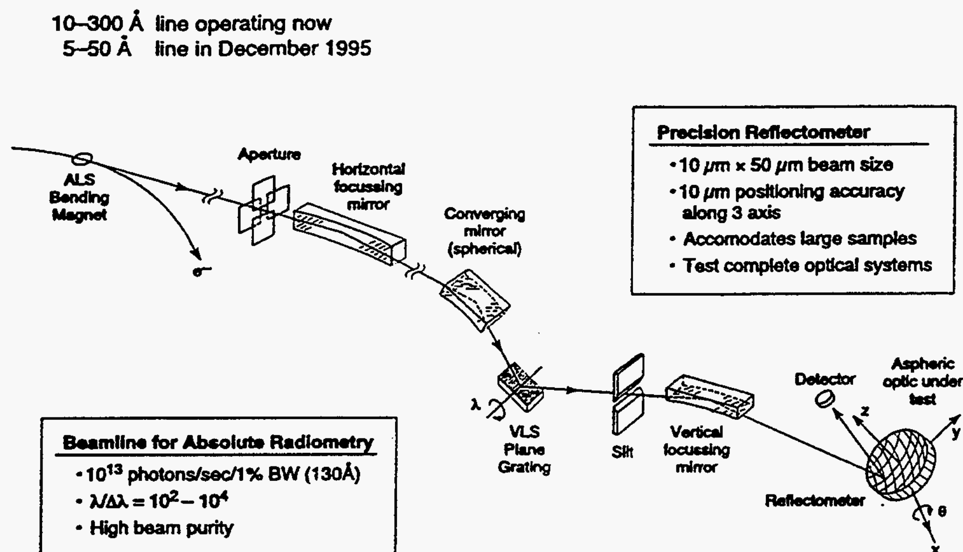

Figure 3.2: A schematic diagram of CXRO's beamline 6.3.2. reflectometer [7] at the Advanced Light Source (ALS).

The optics consist of a plane grating monochromator, a reflectometer chamber and refocusing mirrors to provide a small spot on the sample. There is no entrance slit in this monochromator design. A plane grating with varied line spacing operates on the converging light from a spherical mirror, working at high demagnification. Aberrations of the mirror are corrected by the line spacing variation, so that the spectral resolving power E/ΔE is limited by the ALS source size to about 7000. To demonstrate the resolving capabilities of the instrument, the ionization lines from a selection of gases such as Ar. Xe, Kr, N_2, shown in Fig. 3.3, were used. Energy is scanned by a simple rotation of the grating with a fixed exit slit. Three gratings, 300, 600 and 1200 lines/mm, are used in order to access the entire energy range of the instrument. A selection of filters is available for second order and stray light suppression at various energies. At the lower energies, where higher orders are present, an additional triple reflection low pass filter is used. In this way, spectral purity is achieved to better than

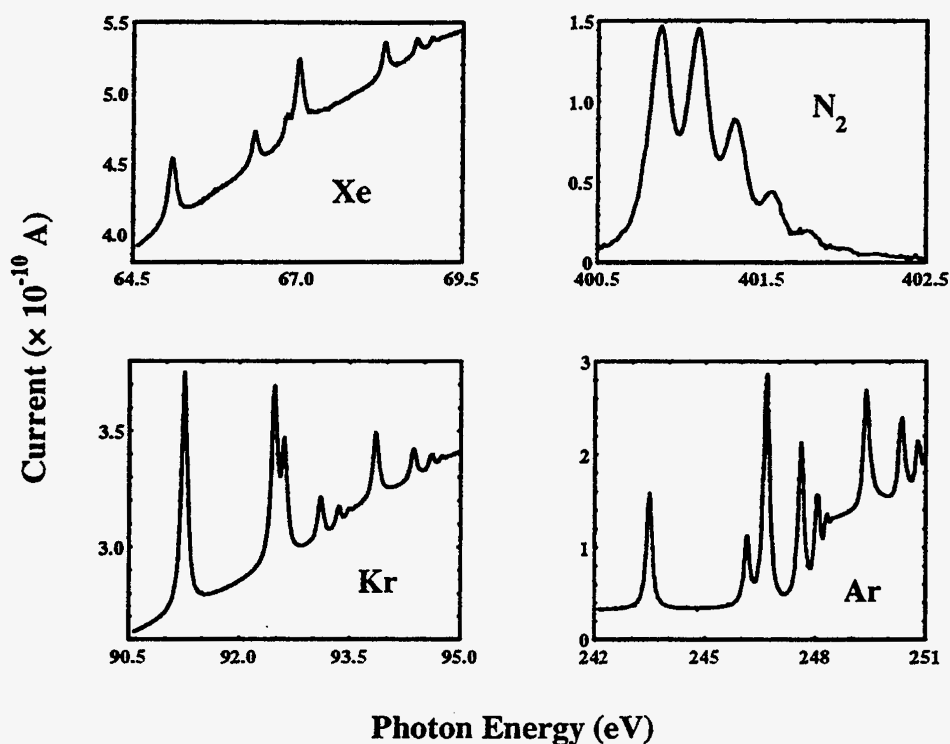

Figure 3.3: Absorption spectra [4] from various gases, aiming to demonstrate the resolution capabilities of beamline 6.3.2. Data were obtained using a gas-cell detector mounted in the reflectometer chamber, and are plotted as ion current vs. photon energy. UPPER LEFT: Xe gas at 100 mTorr. The ionization lines in the spectrum represent two Rydberg series, converging to the Xe 4d absorption edge ($4d_{5/2}$ at 67.5 eV, $4d_{3/2}$ at 69.5 eV). The resolution of the experimental data was $E/\Delta E = 550$, while $(E/\Delta E)_{theoretical} = 586$. LOWER LEFT: Kr gas at 100 mTorr. The lines compose two Rydberg series, converging to the Kr 3d absorption edge ($3d_{5/2}$ at 93.8 eV, $3d_{3/2}$ at 95 eV). $E/\Delta E = 970$, $(E/\Delta E)_{theoretical} = 1098$. UPPER RIGHT: N_2 gas at 30 mTorr. The $1s \rightarrow 1\pi^*$ spectrum of N_2 is shown. The resolution in this measurement was $E/\Delta E$=7000, limited by the source size only, and was achieved with an exit slit width of 5 μm. $(E/\Delta E)_{theoretical}$ is around 9000. LOWER RIGHT: Ar gas at 80 mTorr. The Rydberg series is converging to the Ar 2p edge ($2p_{3/2}$ at 248.4 eV, $2p_{1/2}$ at 250.6 eV). $E/\Delta E = 1675$, $(E/\Delta E)_{theoretical} = 1960$. The aforementioned instrumental resolutions are considered more than adequate for the type of experiments performed at beamline 6.3.2.

99%. Wavelength calibration was achieved by obtaining transmission spectra around absorption edges from a series of filters covering the range from the Al $L_{2,3}$ edge (72.5 eV) to the Cu $L_{2,3}$ edge (932.5 eV). After comparing the experimental data to the well-documented features of these absorption thresholds in the literature, spectral calibration was achieved with an accuracy of 0.05%. Additional optics are used in order to focus the beam in the horizontal and vertical directions and the current from the vertically focusing mirror is collected in order to normalize the signal against the storage ring current decay. The reflectometer chamber (10^{-8} Torr base pressure) can accomodate samples with size up to 8 inches and has the capability of positioning the sample to $\pm$ 4 μm and setting its angular position to 0.002°. Radiation emitted from beamline 6.3.2 is s-polarized to at least 90% in intensity, depending on the exact position and size of the vertical aperture at the entrance of the beamline with respect to the beam and on the energy of operation at the ALS (1.5 or 1.9 GeV).

Chapter 4

Silicon

4.1 Introduction

Silicon is among the materials of particular importance for practical applications in the EUV/soft x-ray range, due to its implementation as filter and spacer material in multilayer mirrors, for energies below the $L_{2,3}$ edge (99.8 eV). In this work, the method of angle dependent reflectance is evaluated and implemented in order to obtain the optical constants of Si in the region around the $L_{2,3}$ edge. The refractive index of Si in this energy range has been investigated by previous experimenters [8,10,12] using various methods such as reflectance, transmission and photoelectric yield. The discrepancies among their data arise mainly due to different sample preperation conditions, the surface quality of the samples used for the measurements and the inherent difficulties of each method. Angle dependent reflectance measurements have the advantage that both δ and β may be deduced experimentally, and thus provide an important test of the tabulated values of δ generated using the Kramers-Kronig relations. In addition, measurements may be performed on bulk samples without the need to fabricate the free standing thin films required for transmission measurements. The reflectance method has allowed measurements to be performed on amorphous Si where the high stress in sputtered films made the fabrication of free standing films difficult. Some of the possible pitfalls of the method include its sensitivity to surface roughness and contamination. On the other hand, the choice of silicon as the material for this study

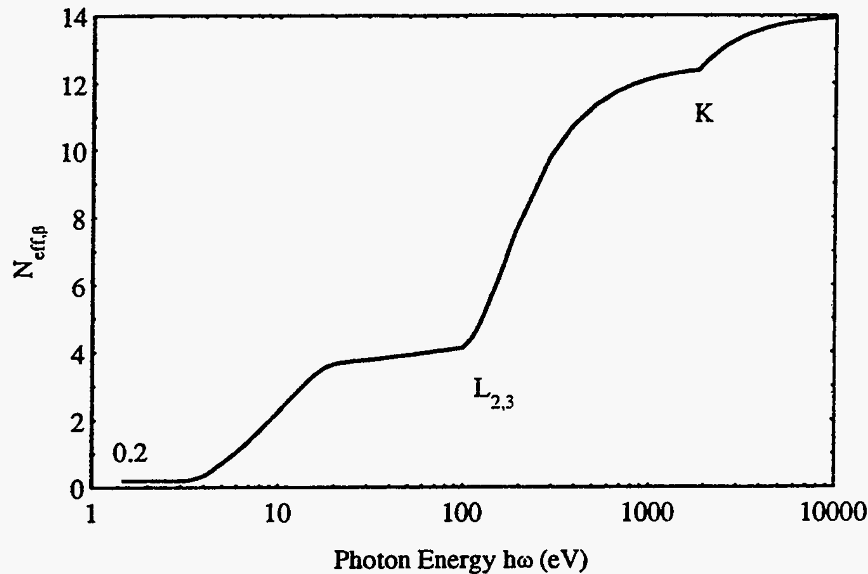

Figure 4.1: Calculation of $N_{eff,\beta}$ vs. photon energy for Si according to the partial sum rule of eq. (2.71), using the data for β from the 1993 atomic tables [3]. The result is $N_{eff,\beta}(\hbar\omega \rightarrow 0) = 0.2$, indicating a missing oscillator strength of 0.2 electrons. This lack in oscillator strength should cause overestimation of δ at low energies.

offered the ability to obtain highly polished wafers thus reducing the effects of surface roughness, and the possibility to chemically clean and passivate the surface against oxidation.

The quality of the absorption data for Si in the 1993 atomic tables is examined by means of the sum rule for β, eq. (2.71). This equation yields identically $N_{eff,\beta} \equiv Z^*$ and should give $N_{eff,\beta}(\omega = 0) = 0$ only if accurate absorption data have been used in the entire energy range, as discussed in Sec. 2.4. Fig. 4.1 shows a plot of $N_{eff,\beta}(\omega)$ for silicon using the experimental data for β from the 1993 atomic tables [3]. It is seen that the experimental $N_{eff,\beta}(\omega)$ is 0.2 as $\hbar\omega$ goes to zero. This implies, from eq (2.71), that there is a missing oscillator strength of 0.2 electrons in the absorption spectrum. One may ask, What effect will this missing oscillator strength have on the calculated values of f_1? The "x-ray form" of the Kramers-Kronig relation, eq. (2.50) has the property that it yields the correct result ($f_1 = Z$) in the high energy limit. Moreover, it can be shown [37] that if a defect in the data for the oscillator strength occurs around a frequency ω_d, then the values of f_1 determined using eq. (2.50) will

be correct in the region $\omega > \omega_d$ and eq. (2.50) will overestimate f_1 for $\omega < \omega_d$. Since the deficiency in oscillator strength in the data for silicon as shown in Fig. 4.1 is expected to lead to systematic errors in the determination of f_1 at low energies, it is particularly important to have an independent measurement such as provided by the reflectance method. In addition, it would be interesting to obtain both δ, β in an exclusively experimental manner in the $L_{2,3}$ absorption threshold energy region of silicon, where fine structure may possibly be present.

4.2 Contamination

Silicon grows a native oxide on its surface when it is exposed to air. Moreover, the hydrocarbons which exist in the atmosphere can be deposited in the form of an organic film on any surface exposed in air. Thus, oxide and carbon will be considered as the main two sources of contamination on a silicon surface in the analysis below. In order to examine if oxygen and carbon overlayers may cause serious alterations in the results of reflectance measurements for optical constant determination, the following tests are performed: A silicon sample is assumed to have a SiO_2 or a C overlayer of variable thickness, and for each thickness value the reflected intensity $R'(\theta)$ of the system "Si substrate + overlayer" is calculated, using for $R'(\theta)$ the expression from ref. 31 for the reflectance of a thin film on top of a semi-infinite substrate. The values from the 1993 atomic tables are used for the optical constants of the substrate (Si) and the overlayer (SiO_2 or C). This procedure is repeated for a number of energies within the range of interest. For each of these energies, the optical constants (δ, β) are obtained from a fitting algorithm which determines the best fitted δ, β using as closeness criterion the "squared error"

$$S = \sum_{i=1}^{N} \frac{[R'(\theta_i) - R(\theta_i)]^2}{\sigma_i^2}, \tag{4.1}$$

where N is the number of angles considered and σ_i^2 represents the uncertainty (noise) at each angle point. $R(\theta_i)$ is the Fresnel reflectance, given by eq.(2.43) for s-polarized radiation, using the pair of (δ, β) that is being evaluated by the algorithm. The best fitted (δ, β) pair is determined by the least value of the statistic S. The purpose of this procedure is to predict what would happen in an actual experimental determination of the optical constants through measurements on surface contaminated samples (the calculated $R'(\theta)$ curves represent the "experimental" data). Thus, the errors in the determination of δ, β with respect to the tabulated values in ref. 3 may be predicted. Since the sample surface is assumed to be perfectly flat and smooth in these calculations, the deviations from the tabulated values of the optical constants should be due to the presence of surface contamination. The values reported in the literature [12,40] for the thickness of SiO_2 and C overlayers on a commercially avail-

able Si wafer are in the range 10-15 Å and 5 Å, respectively. These values are also verified in this work, from the surface analysis results presented in Sec. 4.3. Thus, SiO_2 thicknesses from 0 to 15 Å and C thicknesses from 0 to 5 Å were used for the determination of the "experimental" $R'(\theta_i)$ in eq. (4.1). Since the purpose of these calculations is to simulate experimental data, the range of angles considered in each case is $0 \leq \theta \leq \theta_{max}$ such that $R'(\theta_{max}) \sim 10^{-3}$ and the "experimental" uncertainty σ_i^2 was $\sigma_i^2 = [0.01 \times R'(\theta_i)]^2$, in agreement with the detection limitations of the reflectometers used for the measurements, described in Sections 3, 4.4.

SiO_2 on Si, 60 eV					
SiO_2 thickness (Å)	δ ($\times 10^{-2}$)	$(\delta - \delta_0)/\mid \delta_0 \mid$ ($\times 100\%$)	β ($\times 10^{-3}$)	$(\beta - \beta_0)/\beta_0$ ($\times 100\%$)	S
0	2.860		4.70		
1	2.866	0.21	4.66	-0.85	51.17
2	2.830	-1.05	4.64	-1.28	192.42
5	2.732	-4.47	4.62	-1.70	937.53
10	2.616	-8.53	4.84	2.98	1901.35
15	2.574	-10.00	5.42	15.32	1572.88

C on Si, 60 eV					
C thickness (Å)	δ ($\times 10^{-2}$)	$(\delta - \delta_0)/\mid \delta_0 \mid$ ($\times 100\%$)	β ($\times 10^{-3}$)	$(\beta - \beta_0)/\beta_0$ ($\times 100\%$)	S
0	2.860		4.70		
1	2.846	-0.49	4.70	0	5.97
2	2.838	-0.77	4.72	0.42	14.67
3	2.832	-0.98	4.78	1.70	18.2
4	2.830	-1.05	4.84	2.98	17.85
5	2.832	-0.98	4.96	5.53	22.62

Table 4.1: The effects of various thicknesses of SiO_2 and C in the determination of the optical constants of Si are calculated at 60 eV. The sixth column contains the values of the least squared error from eq. (4.1), which determines the best fitted (δ, β). The results presented in this table are also illustrated in Figs. 4.2(a), 4.3(a).

Tables 4.1, 4.2 summarize the results of the fitting for two energy points, representing two energy regions; below the Si $L_{2,3}$ edge (60 eV) and above the edge (130 eV). The algorithm evaluated a number of (δ, β) pairs around the tabulated values in increments of 2×10^{-5}, in order to find the best fitted pair. Figs. 4.2, 4.3 illustrate the results of Tables 4.1, 4.2 for the errors in the fitting of δ, β vs. thickness of contamination. At 60 eV (Table 4.1), the presence of a SiO_2 overlayer with thickness up to 15 Å leads to errors in δ and β of up to 10% and 15%, respectively (Fig. 4.2(a)). The errors introduced by a 5 Å C overlayer in the determination of δ and β are 0.98% and 5.53%, respectively (Fig. 4.3(a)). At 130 eV (Table 4.2), contamination seems to lead to much greater errors in the fitting of the optical constants. For instance, in the case of δ, these deviations exceed 100% of its tabulated value for SiO_2 thicknesses greater than 5 Å (Fig. 4.2(b)) and C thicknesses greater than 3 Å (Fig. 4.3(b)). It will be shown in Sec. 4.4 that such large deviations are characteristic of the fitting algorithm in the region above the Si $L_{2,3}$ edge, and are due to the relationship between δ and β in this energy range. It is obvious from the results of Tables 4.1, 4.2 that the value of the least squared error S, which determines the goodness of fit, becomes larger with increasing overlayer thickness. This means that the fitting ability of the algorithm gets worse if reflectance data from a contaminated Si surface are used.

In summary, the presence of oxide and organic contamination on a Si surface used for reflectance measurements and subsequent fitting of δ, β may result in serious errors in the determination of the optical constants. Therefore, cleaning of the Si surface is required prior to reflectance measurements. The experimenter should also be aware of the remaining amount of contamination, if any, after the cleaning treatment, so that it can be taken into account after the measurements. For this reason, the procedure outlined in Tables 4.1, 4.2 was repeated for more energy points, below, above and at the edge, in order to be able to correct the experimental results for the optical constants for possible residual SiO_2 and C contamination, after the cleaning procedure and surface analysis are performed, as described in the following section.

SiO$_2$ on Si, 130 eV					
SiO_2 thickness (Å)	δ ($\times 10^{-3}$)	$(\delta - \delta_0)/\mid \delta_0 \mid$ ($\times$100%)	β ($\times 10^{-2}$)	$(\beta - \beta_0)/\beta_0$ ($\times$100%)	S
0	1.81		1.907		
1	1.38	-23.76	1.976	3.62	10.73
2	0.9	-50.28	2.044	7.18	37.39
5	-0.4	-77.9	2.232	17.04	158.29
10	-2.1	-216.02	2.506	31.41	338.92
15	-2.72	-250.28	2.728	43.05	409.63

C on Si, 130 eV					
C thickness (Å)	δ ($\times 10^{-3}$)	$(\delta - \delta_0)/\mid \delta_0 \mid$ ($\times$100%)	β ($\times 10^{-2}$)	$(\beta - \beta_0)/\beta_0$ ($\times$100%)	S
0	1.81		1.907		
1	1.12	-38.12	2.008	5.30	21.39
2	0.48	-73.48	2.104	10.33	73.33
3	-0.20	-111.05	2.200	15.36	142.34
4	-0.92	-150.83	2.296	20.40	218.67
5	-1.52	-183.98	2.386	25.12	296.65

Table 4.2: The effects of various thicknesses of SiO_2 and C in the determination of the optical constants of Si are calculated at 130 eV. The 3rd and 5th columns show the error in the fitting of δ and β respectively, expressed as a persentage of the tabulated values δ_0 and β_0. The sixth column contains the values of the least squared error from eq. (4.1), which determines the best fitted (δ, β). The results presented in this table are also illustrated in Figs. 4.2(b), 4.3(b).

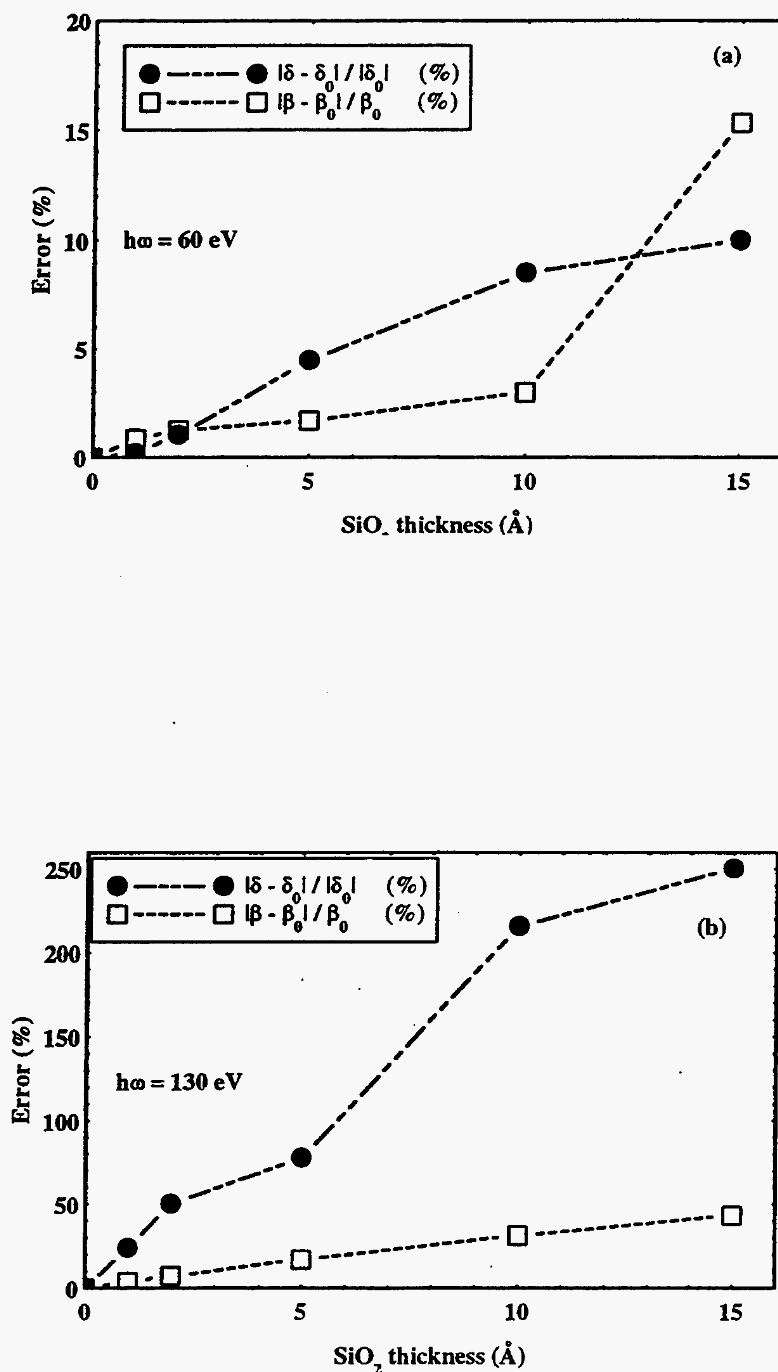

Figure 4.2: The effect of SiO_2 overlayers on the determination of the optical constants of Si is calculated for two energies: (a) 60eV and (b) 130eV. The error in the fitting of δ and β is expressed as a persentage of the tabulated values δ_0 and β_0 at each energy, and is plotted vs. SiO_2 thickness. These results are also presented in Tables 4.1, 4.2. Note that the y-axis scale in (a), (b) is different: the effect of SiO_2 surface contamination at 130 eV is much more pronounced than at 60 eV.

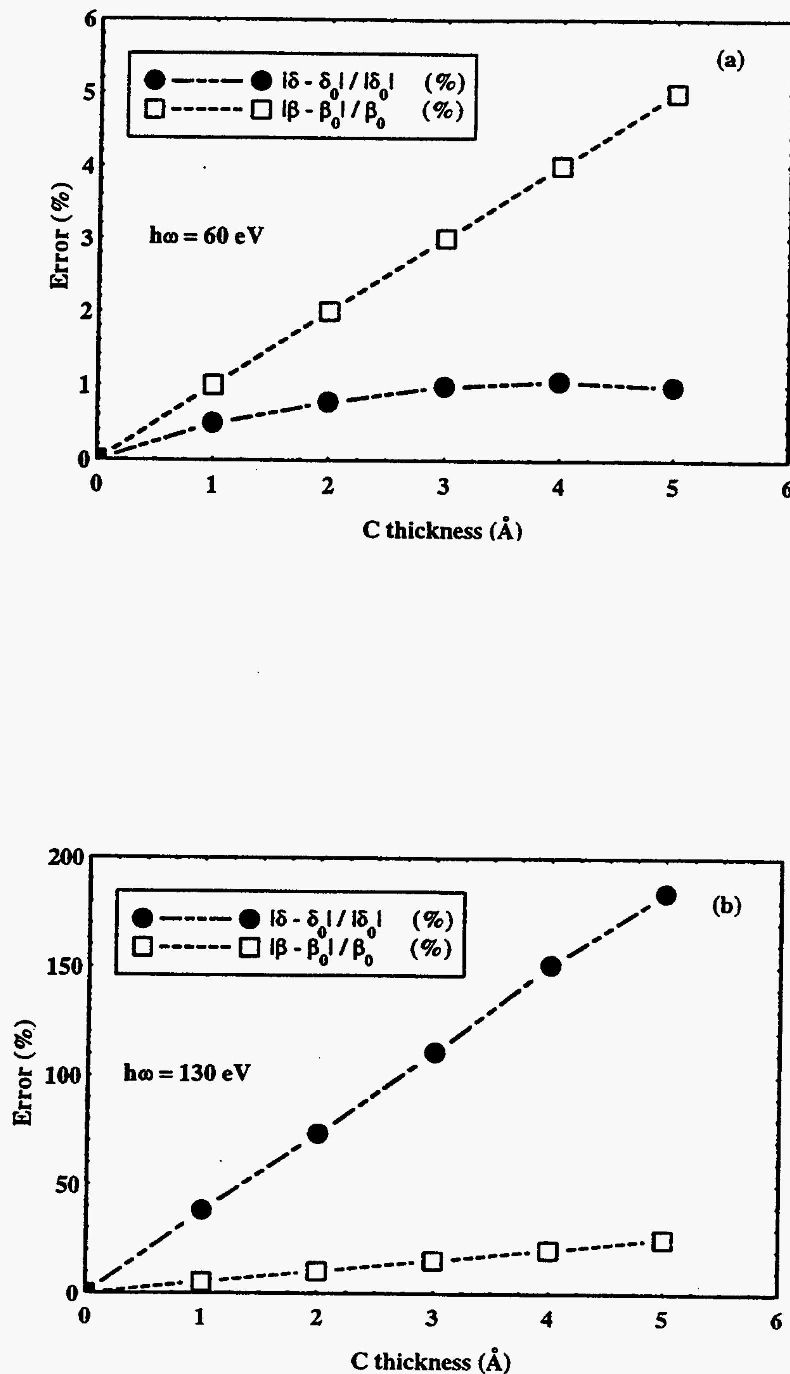

Figure 4.3: The effect of C overlayers on the determination of the optical constants of Si is calculated for two energies: (a) 60eV and (b) 130eV. The error in the fitting of δ and β is expressed as a persentage of the tabulated values δ_0 and β_0 at each energy, and is plotted vs. C thickness. These results are also presented in Tables 4.1, 4.2. Note that the y-axis scale in (a), (b) is different: the effect of C surface contamination at 130 eV is much more pronounced than at 60 eV.

4.3 Sample Preparation and Surface Analysis

The samples used in this experiment are: *a)* Si(111) wafers, "prime" grade, n-doped with As atoms, with resistivity $\rho = 0.005 - 0.013\ \Omega$ cm and thickness 330-530 μm, *b)* Si(100) wafers, "prime" grade, n-doped with P atoms, with resistivity $\rho = 3 - 7\ \Omega$ cm and thickness $356 - 406\ \mu$m, *c)* amorphous Si (3000 Å sputtered Si on a Si(111) wafer). There is extensive literature on Si surface passivation due to the importance of clean and smooth Si surfaces and Si/SiO_2 interfaces in the performance of integrated circuits. Among the most common techniques used in the semiconductor industry for Si surface cleaning and passivation, are:

(i) Ar or He ion sputtering or reactive ion sputtering at low temperature, in order to remove the oxide layer. Post-annealing at high temperature is required in this technique, due to the damage on the surface lattice by the etching procedures.

(ii) High temperature treatment (above 800°C) in ultra high vacuum (UHV) , for removal of the oxide.

(iii) RCA-type cleaning (dipping in aqueous mixtures of unstabilized hydrogen peroxide with ammonia and HCl) for removal of organic contamination, particles and metals, followed by H-passivation in dilute HF acid.

(iv) UV treatment in O_2 enhanced atmosphere, in order to remove organic contaminants, followed by etching in aqueous solutions of NH_4F or HF, or ethanol solutions of HF, in order to achieve H-passivation of the Si surface [40–42].

In this work, method *(iv)* was applied. High temperature and ion sputttering treatments outlined in methods *(i), (iii)* are not possible without the appropriate equipment. Moreover, there is evidence [43] that RCA cleaning results in a relatively rough surface ($\simeq$ 5 Å reported) while cleaning in NH_4F or HF solutions provides smoother surfaces and also ordered with respect to lattice positions [44]. The cleaning and surface passivation steps are described below.

Each sample was placed for 8-12 hours on a hot plate (200-250°C) under UV rays emitted from a low-pressure mercury discharge lamp, with input power 10 W. The purpose of this step is to remove the organic contamination which exists in the form of hydrocarbons on the surface of the sample. The UV rays from the

lamp have two bands at 1849 Å and 2537 Å which are shown to be important in cleaning. The 1849 Å light dissociates oxygen molecules and produces ozone (O_3). The 2537 Å light initiates photodecomposition of ozone into an oxygen molecule and an activated oxygen atom which reacts with the hydrocarbons on the sample surface and decomposes them into volatile compounds such as H_2O and CO_2. The 2537 Å light is also believed [45] to photosensitize organic contamination and results in enhanced cleaning rates. The activated oxygen atoms which react to remove the organic contamination from the surface, cause at the same time further oxidation of the Si surface, as it will be later shown in surface analysis results. However, this "side effect" is not a problem at this stage of the cleaning procedure because the HF etching step that follows, removes the SiO_2 from the surface. The fact that the 1849 Å light (responsible for the creation of O_3) has a low penetration depth in air and the 2537 Å light (responsible for the dissociation of O_3) has a long penetration depth, results in a strong ozone concentration gradient around the UV source. As a result, the cleaning rates are strongly dependent on the lamp distance from the sample and it is found [45] that a distance $\sim$ 10 mm is required for effective cleaning. At this distance, studies [45] have shown that ordinary air is nearly the optimum environment, and a slight increase of oxygen would enhance the cleaning rate. Therefore, small amounts of oxygen were provided during the UV irradiation of the samples. The teflon and glass vessels used during the H-passivation procedure were degreased in a inorganic oxidizer-H_2SO_4 ("reagent" grade) solution and then rinsed thoroughly with ultrapure water (ρ = 18 MΩ cm, total organic carbon (TOC) = 17 ppb). Each sample was dipped in a 5% HF:ethanol solution for 5-10 minutes. The solution was prepared by diluting a 50% HF solution ("certified particle" grade) in ethanol ("reagent" grade, consisting of 5 volumes of methanol and 100 volumes of 200 proof ethanol). Then, the sample was rinsed in ethanol for 30 seconds and finally dried in N_2 atmosphere for a few seconds. The HF solution etches SiO_2 from the surface and then terminates the dangling bonds mainly with H atoms. The H-passivated surface is much more stable toward oxidation compared to a conventional surface, which has many dangling bonds left. This etching step was also performed with aqueous HF solutions and subsequent rinsing in ultrapure water. However, using ethanol solutions gave consistently better

results. This has also been verified in the literature, where ethanol was found to have the following advantages over aqueous solutions: 1) Water rinsing has been shown [41] to initiate new oxidation of the surface, a process most probably nucleated by Si-OH sites formed by hydrolysis of Si-F. 2) Any organic contamination picked up after the UV cleaning may be dissolved by the ethanol, thus reducing the remaining amount of C on the surface.

Immediately after the cleaning, the piece of Si wafer on which the reflectance measurements are going to be performed is loaded in the reflectometer chamber in order to prevent new oxidation and carbon contamination of the H-passivated surface. At the same time, witness samples of the same cleaned wafer are taken to an x-ray photoelectron spectroscopy (XPS) system, in order to perform surface analysis and check the results of the cleaning procedure. Ideally, if perfect H-passivation of the surface took place (i.e. SiO_2 completely removed and all dangling bonds terminated by H atoms), the surface should be stable against any new oxidation. However, the cleaning is not 100% effective, and there are always remaining dangling bonds or oxidized sites that initiate a slow degradation of the surface. In general, the cleaning results depend highly on the amount of organic substance in the atmosphere and also on other undetermined factors such as re-contamination from vessels and handling. All the above effects are observed quantitatively at the surface analysis results shown later in this section. Surface analysis was performed in a PHI 5300 [46] system at the Lawrence Berkeley National Laboratory, using the XPS method, outlined in the diagram of Fig. 4.4, also known as electron spectroscopy for chemical analysis (ESCA), which is accomplished by illuminating the sample with monoenergetic x-rays and by analyzing with an electron spectrometer the photoelectrons emitted, according to their kinetic energy. The presence of an element on the sample surface is identified by the binding energy E_b of its atomic core electrons

$$E_b = \hbar\omega - E_k, \tag{4.2}$$

where $\hbar\omega$ is the source photon energy and E_k is the measured kinetic energy of the emitted photoelectrons. A Mg Kα anode ($\hbar\omega$ = 1253.6 eV) was used by the ESCA instrument for all of the measurements in this work. The analyzer is normally

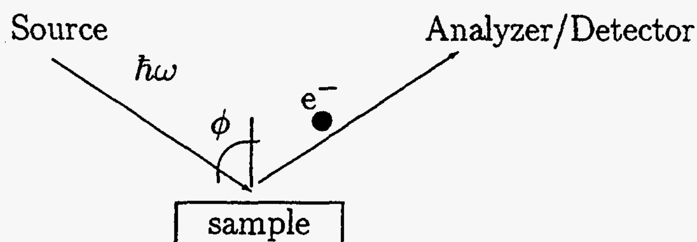

◇ *Source:* Mg Kα anode (1253.6 eV)

◇ *Analyzer/Detector:* Electron spectrometer ($E_k = \hbar\omega - E_b$)

Figure 4.4: Outline of the x-ray photoelectron spectroscopy (XPS) method.

operated as an energy "window", accepting only those electrons having an energy within this fixed window, referred to as "pass energy". Investigating different energies is accomplished by applying a variable electromagnetic field before the analyzer is reached by the electrons. Thus, an analysis of the spectrum after an energy scan provides information on the elemental composition and chemical state of the sample surface. The results are shown in the form of peak areas, as a function of electron binding energy. The peak areas, which represent the integrated photoelectron signal (IPS), are proportional to the concentration of an element in the surface region of the sample. The peak widths of the experimental spectra depend on three factors; the natural photoemission linewidth of the peak, the linewidth of the x-ray source (in this case δE_{Mg} = 0.65 eV) and the energy resolution of the analyzer. Assuming Gaussian peaks, the observed linewidth should be the square root of the sum of the squares of these terms. The resolution of the ESCA energy analyzer is about 2.5% of the pass energy and the electron counting time is inversely proportional to the pass energy [47]. Two types of scans were used in this experiment: *(i)* "Survey" scans, with a pass energy of 178.95 eV (fast, low resolution scans) and *(ii)* "multiplex" scans, with a pass energy of 35.75 eV (slower, high resolution scans), for a more detailed inspection of the peaks. The discussion in the next paragraph describes how the results of the

XPS scans are being implemented for overlayer thickness calculations.

The thicknesses of SiO_2 and C are calculated from the x-ray photoelectron spectra by means of the equation [48]:

$$\frac{Y_o}{Y_s} = \frac{\mu_o \, M_s \, \sigma}{\mu_s \, \rho_s \, N \, L \, \cos\phi} \, T, \tag{4.3}$$

where Y_o is the IPS from the overlayer (O 1s or C 1s) and Y_s is the IPS from the substrate (Si 2p) photoelectrons, obtained from the ESCA system as diagnostics of a "multiplex" scan; μ_o and μ_s (barns/atom) are the overlayer and substrate photoionization cross sections respectively, where 1 barn = 10^{-24} atoms/cm^2; σ (atoms/cm^2) is the surface coverage of overlayer atoms; M_s (gr/mole) is the molecular weight of the substrate; ρ_s (gr/cm^3) is the mass density of the substrate; L (Å) is the escape depth for the substrate (Si 2p) photoelectrons; ϕ is the angle of collection of photoelectrons by the analyzer with respect to the sample normal, as shown in Fig. 4.4 ($\phi = 45°$ in this case); N is Avogadro's number ($N = 6.022 \times 10^{23}$ molecules/mole). The factor T accounts for the transmission efficiency of the ESCA energy analyzer. When the system is operated in a constant "pass energy" mode, as in this case, the transmission efficiency of the analyzer is inversely proportional to the kinetic energy of the detected photoelectrons. Since Y_o/Y_s is on the left hand side of eq. (4.3), T should be equal to

$$T = \frac{E_{k,s}}{E_{k,o}} = \frac{\hbar\omega - E_{b,s}}{\hbar\omega - E_{b,o}}, \tag{4.4}$$

where, as usual, "s", "o" stand for the substrate and overlayer respectively. The surface coverage σ can be further analyzed as follows:

$$\sigma = n_o d_o, \tag{4.5}$$

where n_o (atoms/cm^3) is the overlayer element atomic density and d_o (Å) is the overlayer thickness. After replacing eqs. (4.4, 4.5) in eq. (4.3) and solving for d_o, the result is

$$d_o = \frac{\mu_s \, \rho_s \, N \, L \, \cos\phi}{\mu_o \, n_o \, M_s} \, \frac{\hbar\omega - E_{b,o}}{\hbar\omega - E_{b,s}} \, \frac{Y_o}{Y_s}. \tag{4.6}$$

For a Si substrate, $M_s = 28$ gr/mole and $\rho_s = 2.33$ gr/cm^3. Moreover, for the Si 2p subshell ($E_{b,s} = 99.8$ eV) and the Mg Kα emission line ($\hbar\omega = 1253.6$ eV): $L =$ 24 Å [49], $\mu_s = 20 \times 10^3$ barns/atom [3].

For SiO_2 as the overlayer, the oxygen atomic density n_O is calculated from the expression

$$n_O = \frac{\rho_{SiO_2}\, 2\, N}{M_{SiO_2}}, \tag{4.7}$$

where $\rho_{SiO_2} = 2.3$ gr/cm^3 is the SiO_2 mass density, M_{SiO_2}=28+32=60 gr/mole is the SiO_2 molecular weight and the factor 2 accounts for 2 oxygen atoms per SiO_2 molecule. The result of eq. (4.7) is $n_O = 4.6 \times 10^{22}$ atoms/cm^3. Finally, from eq. (4.6), using the above calculations, the photoionization cross section for the O 1s subshell [3] $\mu_O = 67.22 \times 10^3$ barns/atom [3] and the binding energy $E_{b,O} = 543.1$ eV, the thickness d_O of the oxide is given by

$$d_O = 3.4\, \frac{Y_O}{Y_s} \qquad (\text{Å}). \tag{4.8}$$

For C as the overlayer, the atomic density n_C is given by

$$n_C = \frac{\rho_C\, N}{M_C}, \tag{4.9}$$

which, for $\rho_C = 2.2$ gr/cm^3 and $M_C = 12$ gr/mole, yields $n_C = 11.1 \times 10^{22}$ atoms/cm^3. So, from eq.(4.6), using the photoionization cross section for the C 1s subshell [3] $\mu_C = 23.34 \times 10^3$ barns/atom and the binding energy $E_{b,C} = 284.2$ eV, the carbon overlayer thickness d_C becomes

$$d_C = 5.5\, \frac{Y_C}{Y_s} \qquad (\text{Å}). \tag{4.10}$$

If one wants to express the thicknesses d_O, d_C in terms of oxygen or carbon monolayers (ML) respectively, the substrate orientation should be taken into account. In general, if D represents the thickness of the overlayer in ML, then

$$D = \frac{d_o\, n_o}{[\text{number of atoms per ML of overlayer per cm}^2 \text{ of substrate}]} \qquad (\text{ML}), \tag{4.11}$$

where $d_o\, n_o$ is the surface coverage σ of the overlayer. In the case of oxygen overlayer (in the form of SiO_2) on a Si(111) substrate, using simple geometry considerations and the cubic lattice constant $\alpha = 5.43$ Å of the Si crystal, it is found that 1 ML of Si(111) = 7.8 $\times 10^{14}$ atoms/cm^2. In a similar way, when the Si substrate has the (100)

orientation, it is found that 1 ML of Si(100) = 6.8 $\times 10^{14}$ atoms/cm^2. In the case of SiO_2 on a Si substrate, it will be assumed that two oxygen atoms correspond to each Si atom in the SiO_2 molecule. This is a simplified model which somewhat overestimates the number of oxygen atoms, because it does not account for the irregularities of the Si/SiO_2 interface for each of the (111), (100) orientations [50]. Nevertheless, it is giving a quite good estimate for the oxygen monolayers. Therefore, according to the calculations above: 1 ML of O_2 on Si(111) = 1.56 $\times 10^{15}$ atoms/cm^2; 1 ML of O_2 on Si(100) = 1.36 $\times 10^{15}$ atoms/cm^2. Finally, on amorphous Si substrate [51], 1 ML of O_2 on amorphous Si $\simeq 1.5 \times 10^{15}$ atoms/cm^2. Using each the above results in of eq. (4.11), with $d_O = 3.4(Y_O/Y_s)$ Å from eq. (4.8) and $n_O = 4.6 \times 10^{22}$ atoms/cm^3, yields

$$\text{on Si(111) substrate, } D_O = 1 \, \frac{Y_O}{Y_s} \quad (\text{ML}), \tag{4.12}$$

$$\text{on Si(100) substrate, } D_O = 1.15 \, \frac{Y_O}{Y_s} \quad (\text{ML}), \tag{4.13}$$

$$\text{on amorphous Si substrate, } D_O \simeq 1.04 \, \frac{Y_O}{Y_s} \quad (\text{ML}). \tag{4.14}$$

For a C overlayer in the form of hydrocarbons, it is found [41,42] that 1 ML C = 1.05×10^{15} atoms/cm^2. Using this in eq. (4.11) with $d_C = 5.5 \, (Y_C/Y_s)$ Å from eq. (4.10) and $n_C = 11.1 \times 10^{22}$ atoms/cm^3, yields

$$D_C = 5.8 \, \frac{Y_C}{Y_s} \qquad (\text{ML}). \tag{4.15}$$

The model of uniform overlayers covering the whole surface which is assumed in these calculations does not account for the possible overlayer inhomogeneities and stoichiometry variations on a contaminated or a cleaned surface. However, it gives an estimate for the "average" overlayer coverage, which is useful for quantitative analysis. It should also be mentioned that the above method is accurate for submonolayer thicknesses on the surface and underestimates the overlayer coverage by a maximum of 10% if several monolayers are present [48]. Another source of uncertainty is the attenuation length L of Si 2p photoelectrons in equation (4.6). L can be determined only through experiments and the values provided by various authors over the years

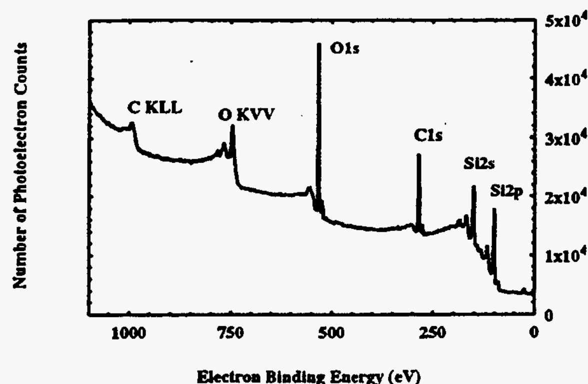

Figure 4.5: Measured XPS analysis results and inferred overlayer thicknesses for a Si(111) wafer, "as received".

Element	Integrated Photoelectron Signal Y (counts $\times$ eV/sec)	Thickness d (Å)	Number of Monolayers D (ML)
Si 2p	54580		
O 1s	113000	7	2.1
C 1s	47127	4.8	5

do not always agree (see also discussion on photoemission in Sections 2.2, 4.6). In this work $L = 24$ Å is used, which agrees within $\pm 20\%$ with most experimental data [49].

Surface analysis results are shown, with the accompanying tables presenting quantitatively the oxide and carbon contamination on the surface. The first two columns of the tables are obtained from the ESCA system after a "multiplex" scan, the third column is calculated using eqs. (4.8),(4.10) and the fourth column using eqs. (4.12)-(4.15). Initially, a few pieces of "as received" samples were examined, in order to check the surface contamination before any cleaning is applied. Figs. 4.5, 4.6 show the results for a Si(111) wafer and an amorphous silicon piece (sputtered Si on a Si wafer), respectively. This measurement was repeated for several silicon surfaces before cleaning. The results have shown that the native oxide is ~ 7 Å and the organic contamination ~ 5 Å. The result of Fig. 4.5 for the oxide on an "as received" Si(111) wafer is in very good agreement with the oxide thickness reported in ref. 40 for a commercially available silicon wafer. Next, the efficiency of the UV treatment described in Sec. 4.3 was tested, by performing surface analysis on samples UV cleaned only, without any further treatment. The results for a Si(111) sample are shown in

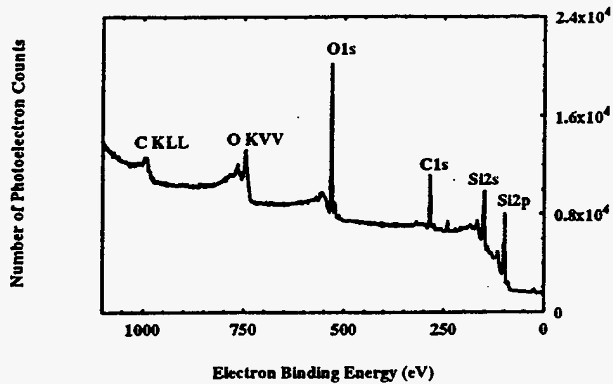

Figure 4.6: Measured XPS analysis results and inferred overlayer thicknesses for an amorphous Si sample, "as received".

Element	Integrated Photoelectron Signal Y (counts × eV/sec)	Thickness d (Å)	Number of Monolayers D (ML)
Si 2p	29470		
O 1s	47600	5.5	1.7
C 1s	18946	3.5	3.7

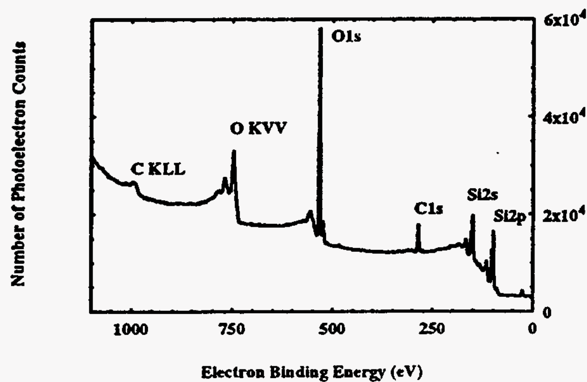

Figure 4.7: Measured XPS analysis results and inferred overlayer thicknesses for a Si(111) wafer after UV treatment is applied.

Element	Integrated Photoelectron Signal Y (counts × eV/sec)	Thickness d (Å)	Number of Monolayers D (ML)
Si 2p	57620		
O 1s	175200	10.3	3
C 1s	18969	1.8	1.9

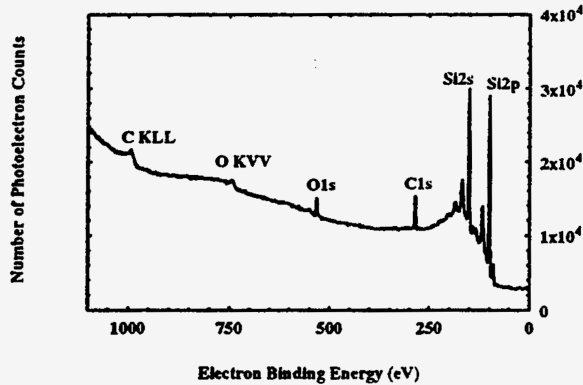

Figure 4.8: Measured XPS analysis results and inferred overlayer thicknesses for a H-passivated Si(111) wafer.

Element	Integrated Photoelectron Signal Y (counts $\times$ eV/sec)	Thickness d (Å)	Number of Monolayers D (ML)
Si 2p	69880		
O 1s	11451	0.5	0.2
C 1s	14527	1.1	1.2

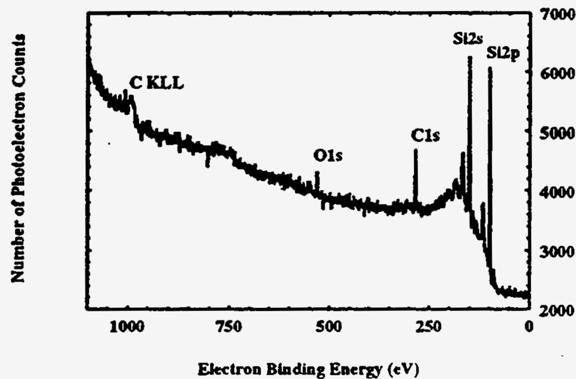

Figure 4.9: Measured XPS analysis results and inferred overlayer thicknesses for a H-passivated Si(100) wafer.

Element	Integrated Photoelectron Signal Y (counts $\times$ eV/sec)	Thickness d (Å)	Number of Monolayers D (ML)
$Si2p$	9972		
$O1s$	1960	0.7	0.2
$C1s$	3265	1.8	1.9

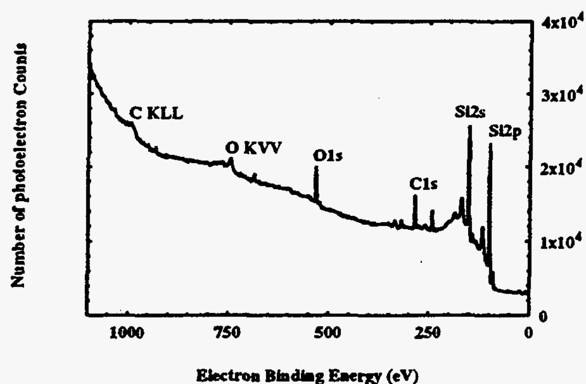

Figure 4.10: Measured XPS analysis results and inferred overlayer thicknesses for a H-passivated amorphous Si sample.

Element	Integrated Photoelectron Signal Y (counts × eV/sec)	Thickness d (Å)	Number of Monolayers D (ML)
Si 2p	61100		
O 1s	22042	1.2	0.4
C 1s	11711	1	1.1

Fig. 4.7. The organic contamination has decreased by ~ 3 Å compared to a sample "as received" (see Fig. 4.5). An increase in the oxide thickness also happens, which is expected due to the nature of this method (see discussion in page 46). This effect is eliminated in the cleaning step which normally follows the UV treatment (dipping in HF: ethanol solution). Testing of UV cleaned amorphous silicon pieces gave results consistent with those of Fig. 4.7. ESCA results for silicon wafers of (111) and (100) orientations and for an amorphous silicon sample, after the complete H-passivation procedure has been performed, are shown in Figs. 4.8, 4.9, 4.10. These are witness pieces from the samples used for the reflectance measurements described in Sec. 4.4. An additional verification of the effectiveness of the H-passivation was performed for an actual reflectance sample at the ALS beamline 6.3.2, as shown in Fig. 4.11. The electron yield measurements in the oxygen K edge (543.1 eV) energy region show that the oxide is indeed removed after the surface treatment. In general, after the cleaning the samples are usually left with sub-monolayer thickness of oxide and ~ 1 ML of carbon on the surface, as it is demonstrated in Figs. 4.8, 4.9, 4.10.

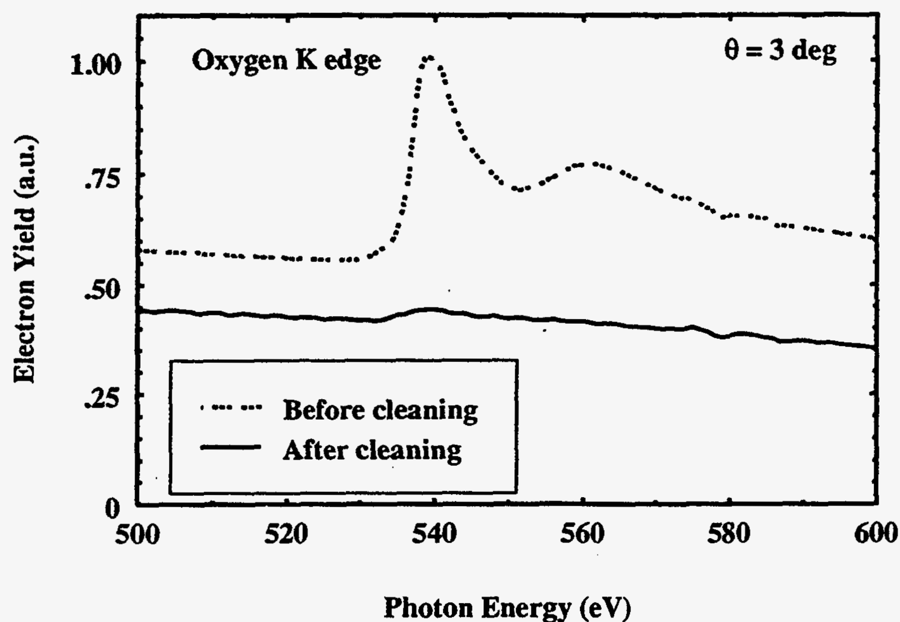

Figure 4.11: Electron yield measurements (arbitrary units) on a Si(100) wafer at $\theta = 3$ deg (grazing angle), performed at the ALS beamline 6.3.2. Before cleaning (dashed line), there is a pronounced peak at the oxygen K edge (543.1 eV) due to the presence of the silicon oxide on the surface; the peak becomes barely visible after surface cleaning is applied (solid line).

4.4 Reflectance Measurements

Reflectance measurements on the H-passivated silicon surfaces were performed using the instruments described in Ch. 3. Data were collected in the form of reflectance curves $R'(\theta)$ for a number of energies in the region 50-180 eV. The software of the instrument allowed for 2-dimensional scans, thus, R vs. θ scans were performed for a large number of closely separated energy points (0.5 eV or 1 eV steps). The experimental curves were fitted by means of a least squares fitting algorithm using the Fresnel equations for the reflected field intensities. The algorithm determines the best fitted δ, β according to a least "squared error" defined in eq.(4.1), repeated below,

$$S = \sum_{i=1}^{N} \frac{[R'(\theta_i) - R(\theta_i)]^2}{\sigma_i^2},$$

with $R'(\theta_i)$ being the experimental data obtained in the range $\theta_{min} \leq \theta_i \leq \theta_{max}$ in 1° steps and $R(\theta_i)$ the theoretical reflectance calculations. $R(\theta_i) = 1/2\ [R_s(\theta_i) + R_p(\theta_i)]$ (unpolarized radiation) was used for the laser plasma source measurements, $R(\theta_i) = R_s(\theta_i)$ was used for beamline 6.3.2, and R_s, R_p were obtained from the Fresnel equations (2.43), (2.44). At the laser plasma source reflectometer, the sources contributing to σ_i^2 were Poisson noise and electronic noise from the detector (Si photodiode), resulting in an expression of the form: $\sigma_i^2 = c_1 R'^2(\theta_i) + c_2$. The parameters c_1, c_2, were determined separately for each energy and had values $\sim 10^{-4}$. Thus, only data with $R'(\theta_i) \geq 1\%$ were used, meaning that the θ_{max} considered in each θ scan was between 8° and 20°, depending on the energy. At the ALS, the dominant source of noise was electronic noise, which yielded $10^{-5} \leq c_1, c_2 \leq 10^{-4}$, thus making possible to use data $R'(\theta_i) \geq 0.3\%$, corresponding to θ_{max} in the range 15° to 35°. All angle scans started at $\theta_{min} = 1°$, due to the incident photon beam over-illuminating the sample at grazing angles $\leq 1°$.

The (δ, β) values provided after the fitting procedure are shown in Fig 4.12. The results look smooth for a range of energies well below the edge, while for the rest of the energies the (δ, β) points look noisy and fluctuating. This behavior is better illustrated in Fig. 4.13 where contour plots of the statistic S of eq. (4.1) are drawn

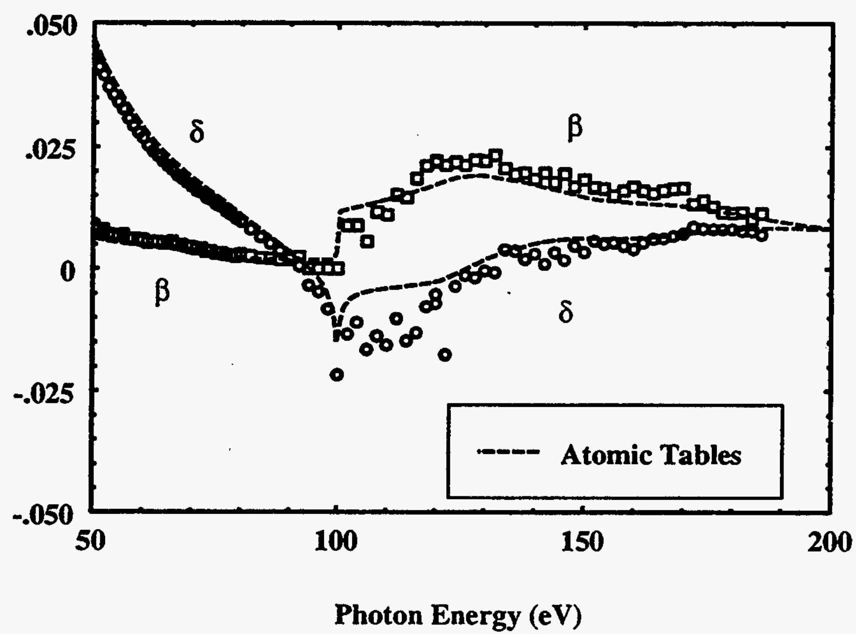

Figure 4.12: The optical constants δ (○), β (□), for a Si(100) sample measured at the ALS beamline 6.3.2. The values for δ, β (dash) from the atomic tables [3], are also shown.

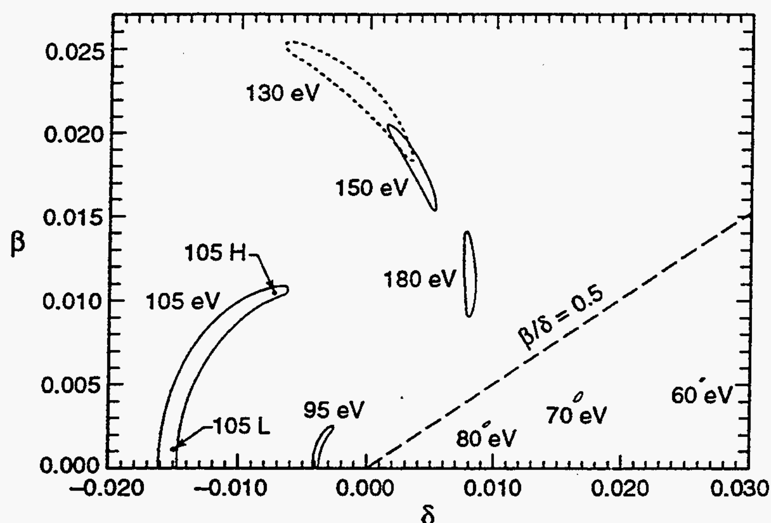

Figure 4.13: Contour plots of S from eq. (4.1) generated with data on a Si(100) sample measured at the ALS. The energies shown are 60, 70, 80, 95, 105, 130, 150 and 180 eV in a $\delta - \beta$ axis system. Each contour area encloses the optical constant pairs fitted by the least squares algorithm within $\pm 1\sigma$ of their actual values. This is equivalent to drawing the contours containing the (δ, β) fitted with $S \leq S_{min} + 2.3$, where S_{min} is the least squared error, at each energy [8,9]. Small contour areas indicate high confidence data, while large areas indicate that a wide range of (δ, β) values meet the fitting criteria, leading to significant uncertainty. The line $\beta/\delta = 0.5$ indicates the boundary between regions of reliable and uncertain fitting. As an example, the reflectivity curves corresponding tc two distant points inside the 105 eV contour, labeled 105H, 105L, are shown in Fig. 4.14.

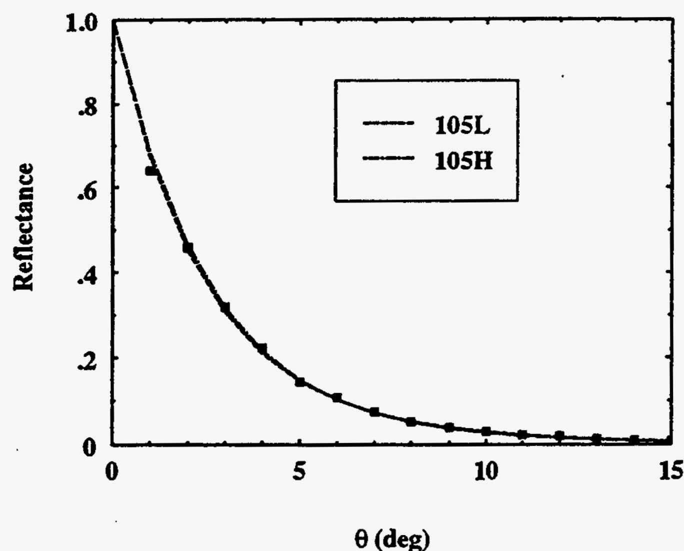

Figure 4.14: Reflectivity curves calculated for s-polarized light and (i) δ = -0.00725, β = 0.0105, (dash-dot), shown as point 105H in Fig. 5, (ii) δ = -0.015, β = 0.001, (dash), shown as point 105L in Fig. 4.13. The reflectance data at 105 eV for a Si(100) sample measured at the ALS beamline 6.3.2, are also shown.

in (δ, β) parameter space for a few energies chosen from the data which were fitted to generate Fig. 4.12. Each contour area encloses the (δ, β) pairs determined by the algorithm with 68% probability of being the actual values ("68% confidence region"), according to the χ_2^2 criterion [8,9]. It can also be shown [9] that these contour areas include the "true values" of the optical constants within $\pm 1\sigma$ error. The two optical constants δ, β are regarded as independent in this parameter estimation model [9]. Fig. 4.13 shows that, for the energies well below the edge, the confidence regions are small indicating that the fitting determines the optical constants with a high degree of certainty (corresponding to the region in Fig. 4.12 where the data look smooth), while for energies close to the $L_{2,3}$ edge and above the contour areas become quite extended, indicating that the fitting is not reliable (leading to the region of fluctuating data in Fig. 4.12). For instance, in Fig. 4.14 the reflectance curves are calculated for two distant (δ, β) pairs inside the 105 eV confidence region (points 105H, 105L, in Fig. 4.13) and the experimental reflectance data are superimposed. All three curves look similar, which explains why the experimental data could be fitted to any of the two points 105H, 105L, or any other point inside the confidence region. Nevertheless, the large extent of the 105 eV confidence region indicates that the results of the fitting

at this energy can not be used to accurately determine both δ, β. This behavior of the fitting algorithm can be related to the shape of the reflectance curves at different energy regions, which depends on β/δ. Fig. 2.2 shows calculated reflectances for a number of β/δ values. For $\beta/\delta << 1$ the reflectance curves have a well defined "shoulder", while as β/δ approaches 1 the curves become exponential-like (negative δ values also result in exponential-like reflectance curves). Obviously, the fitting is successful for energies with β/δ sufficiently below 1, while for $\beta/\delta \sim 1$ or $\delta < 0$ the results for the optical constants are not reliable. This behavior is inherent to the shape of $R(\theta)$ which only depends on β/δ, therefore, it should not be unique to silicon or to this particular energy range. For instance, Hunter [52] has observed, by means of isoreflectance curves, a correlation between the sensitivity of the reflectance method and the real and imaginary parts of n.

For the case of silicon, it is demonstrated in Fig. 4.13 that the region in $\delta - \beta$ space where $\beta/\delta \leq 0.5$ (corresponding to energies ≤ 90 eV) may be chosen as a conservative guide for a region with reliable fitting results. However, the value $\beta/\delta = 0.5$ is not rigorous and certainly depends on experimental conditions such as noise and photon flux, which may vary for different measurements.

The effect of residual contamination on the sample surface after the H-passivation procedure, discussed in Secs. 4.2, 4.3, was taken into account in the fitted values of the optical constants and a correction was applied each time. In the range 50 - 90 eV, for submonolayer oxide and $\simeq 1$ ML organic contamination (typical amounts of residual contamination), the correction for δ was $\pm 1 - 2\%$ and β was overestimated by less than 10%. Separate calculations and corrections were made for each sample, according to the surface analysis results for the residual thicknesses. Furthermore, it should be noted that reflectance values in the EUV/soft X-ray range are sensitive to the state of polarization of the photon beam and the roughness of the sample surface. Previous workers [8,12] have used polarization and roughness as adjustable parameters in addition to δ, β in the fitting model. The analysis presented above assumes a known state of polarization of the source, and perfectly flat and smooth samples. Radiation from the laser plasma source has been assumed unpolarized and the ALS beamline 6.3.2 light has been assumed s-polarized in the fitting model. Both

assumptions approximate the true state of the source polarization by at least 90%, as explained in Sec. 3. There is small but nonzero roughness on the sample surface (see Sec. 4.3), which has not been taken into account in the fitting of the present reflectance data. This choice was made after noticing how sensitive the fitting algorithm is with only two adjustable parameters (δ, β). Introduction of more parameters would make the confidence regions larger, thus introducing greater uncertainty in the fitting results. Calculations have shown that the presence of a possible correction in the state of polarization of the source ($\leq$ 10%) and the effect of surface roughness ($\leq$ 4 Å) in the fitting algorithm, would modify the fitted values of δ, β by less than 0.1% in the range 50 - 90 eV. Thus, polarization and roughness, as fixed parameters, might introduce only a trivial error in the values of the optical constants derived from these measurements.

4.5 Discussion of Reflectance Data

The derived optical constants of silicon will be discussed in the 50 - 90 eV range only, since the fitting algorithm fails to produce reliable results for the rest of the energies considered in this work. It was found that the absorptive part β of the refractive index n for crystalline silicon exhibits structure in the region 60-80 eV, as shown in Fig. 4.15. This effect was observed for both Si(111) and Si(100) samples and is in agreement with previous transmission data for crystalline silicon [10]. It is shown in Fig. 4.15(c) that the structure is not present in the case of amorphous silicon, thus indicating that this effect is probably related to the geometric periodicity of the crystalline silicon lattice. Another possibility would be that oxygen was incorporated into the film during deposition. However, by modeling this it does not appear possible to fit the measured β. The new absorption data were combined with the tabulated values [3] and experimental data at the low energies [28], in order to form a set of values for the absorption in the complete spectrum (1.5 - 30,000 eV) and δ was calculated again from dispersion analysis, using absorption data which satisfied the sum rule in eq. (2.71). This was achieved by adjusting the fitted absorption coefficient in the energy region above the silicon $L_{2,3}$ edge (150-300 eV) where the absorption is high. Modifications were made within the error bars of the available experimental data [53], until the sum rule was satisfied. The modified absorption data were also closer to the photoabsorption calculations using a linear response approximation, by Doolen and Liberman [11]. The sum rules of eqs. (2.70)-(2.72) were then plotted with the new set of optical data for Si, as shown in Fig. 4.16. All three rules behave very well down to 1.5 eV, except for $N_{eff,\epsilon^{-1}}$ below 10 eV, which, according to the theory discussed in Sec. 2.4 should fall off faster than N_{eff,ϵ_2} and $N_{eff,\beta}$. This indicates probable inconsistencies in the calculations for δ at the very low energies. The β-sum rule with the new data yields the correct result $N_{eff,\beta}(0) = 0$, thus the missing oscillator strength of 0.2 electrons is recovered.

In Fig. 4.17 the measured values of δ are plotted in the energy range 55 - 90 eV. The values as determined by the Kramers-Kronig relations in the 1993 atomic tables are shown as a dotted curve. It appears that the Kramers-Kronig method in

the 1993 atomic tables overestimated δ in this region by 8 - 15 %. As discussed in Sec. 2.4 , this is qualitatively consistent with the observed missing oscillator strength in the absorption spectrum. As can be seen in Fig. 4.17, the new Kramers-Kronig calculation is in remarkably good agreement with the present measurements.

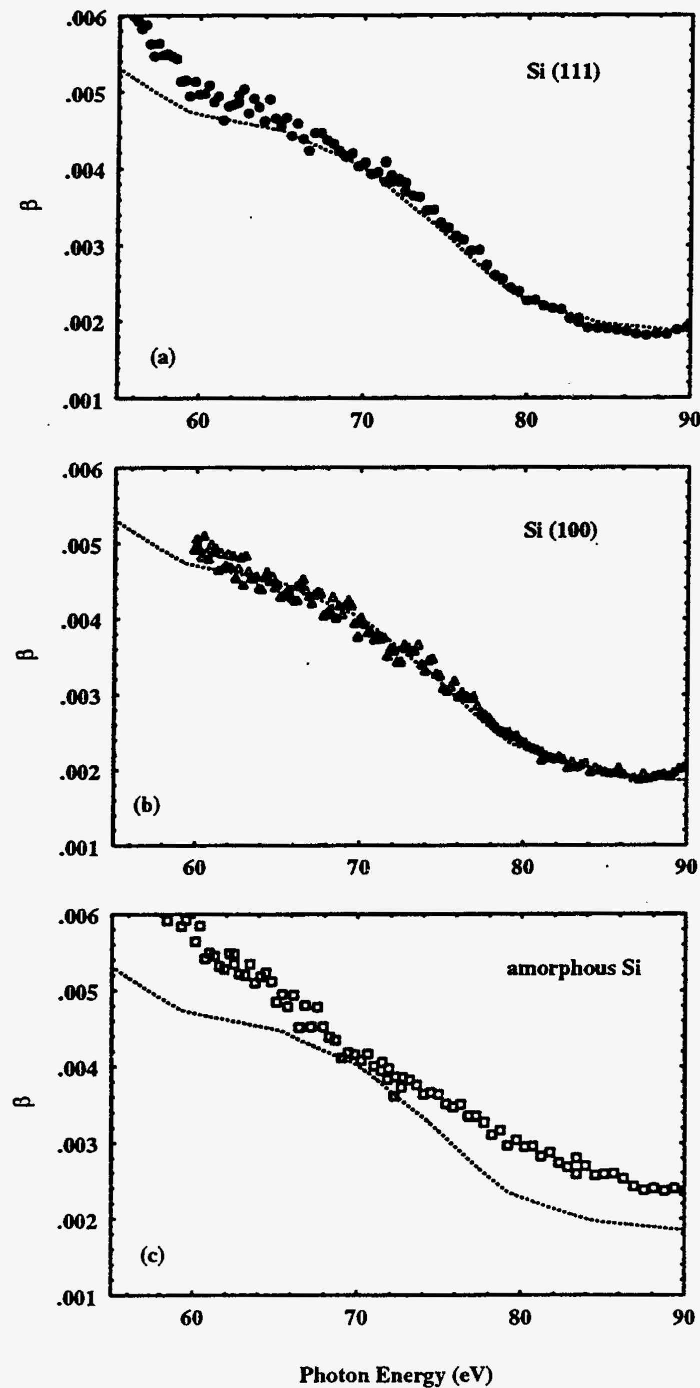

Figure 4.15: Fitted values of β determined from reflectance measurements at the laser-plasma source for (a) Si(111), (b) Si(100) and (c) an amorphous Si sample. Corrections ($\leq$ 10%) for the presence of residual contamination were applied. The dashed line in (a), (b), (c), represents transmission data for Si(111) from ref. 10.

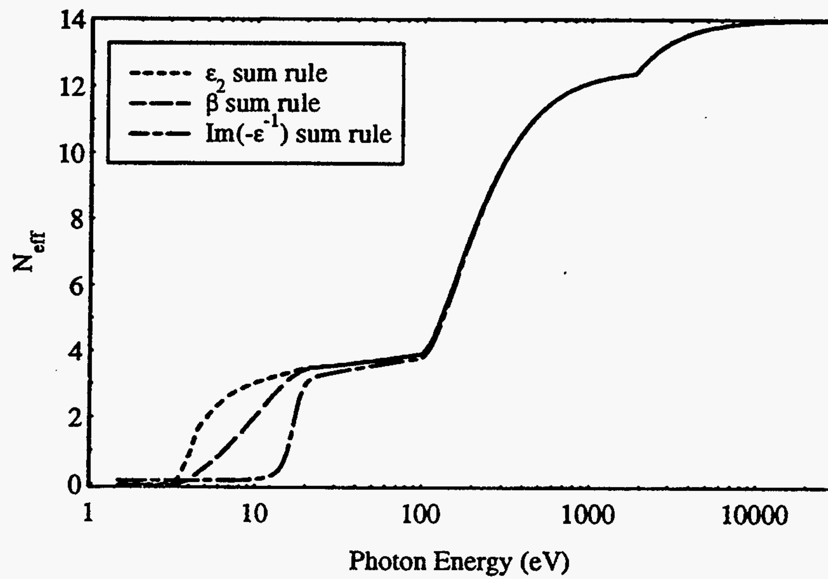

Figure 4.16: Partial sum rules for Si, derived from the new compilation of optical constants including the experimental data presented in this work. The results demonstrate that accurate absorption data have been used and dispersion calculations have been performed self-consistently.

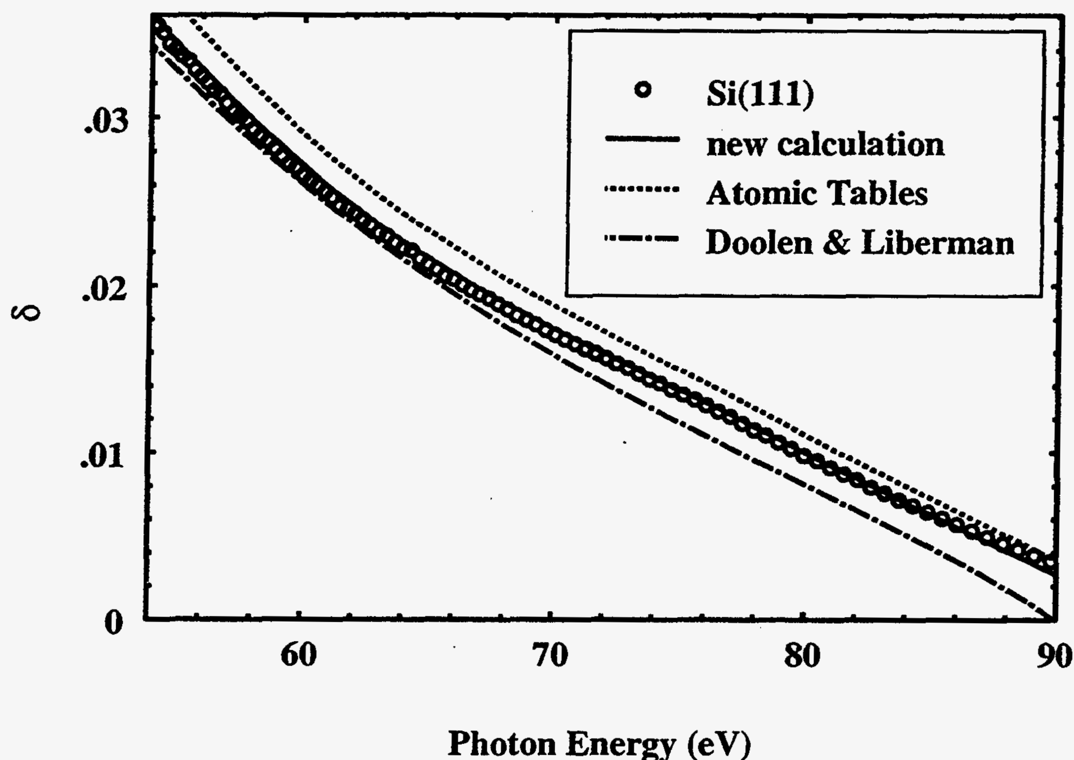

Figure 4.17: Fitted values of δ determined from reflectance measurements on a Si(111) sample measured at the laser-plasma source in the region 55 - 90 eV are shown to be in agreement with the new Kramers-Kronig calculations for δ (solid line), using a revised set of absorption data which satisfy the β-sum rule (see Fig. 4.16). Consistent experimental results for δ in this energy range were obtained from measurements on several Si(100) and Si(111) samples using both the laser-plasma source and the ALS. The Kramers-Kronig calculations from the tables in ref. 3 (dashed line) appear to overestimate the values for δ by 8 - 15%. Theoretical calculations using a linear response approximation model [11] (dash-dot line) are also shown.

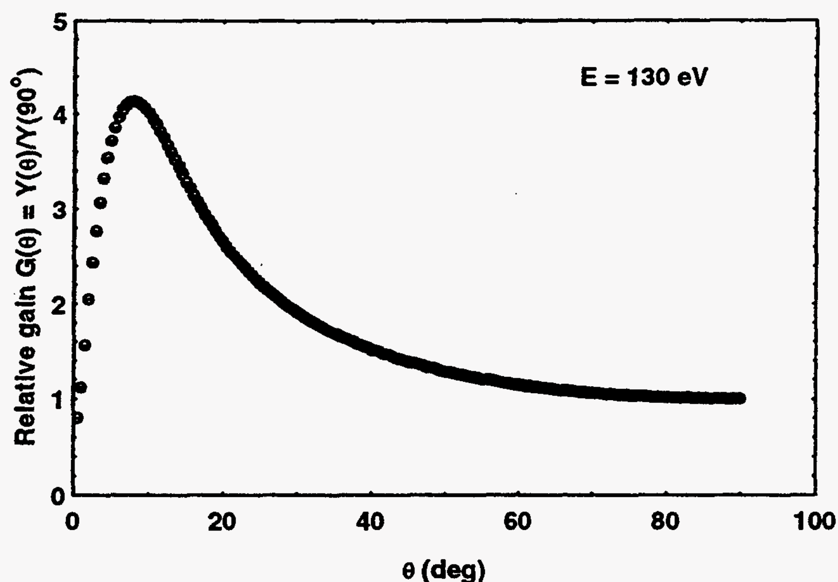

Figure 4.18: Photoelectric yield data from a Si(100) wafer at 130 eV, taken at beamline 6.3.2 at the ALS. The y-axis is the current from the sample, normalized by its value at $\theta = 90°$.

4.6 Photoelectric Yield Measurements

In the range of energies where the reflectance method failed to determine reliably δ, β, i.e. from just below the Si $L_{2,3}$ edge to several tens eV above the edge, angle-dependent photoelectric yield measurements were performed. A Si(100) wafer was used, surface-passivated according to the procedure described in Sec. 4.3. In the reflectometer chamber, the sample was electrically isolated from the holder with mica foils and a wire was used to collect the photoemitted current. Photoelectric yield data vs. angle were taken at various energies. An example of an experimental curve is shown in Fig. 4.18, demonstrating a typical photoelectric yield behavior vs. grazing angle of incidence. At small grazing angles, the emitted current is small, at the expense of high reflectance. The photoemission is increased in the angle region where the reflectance has decreased adequately and the penetration depth of the x-rays is still relatively small, so that most of the photon intensity is concentrated close to the sample surface; in general this region is the critical angle region, although for Si at 130 eV, shown in Fig. 4.18, the critical angle is not well-defined (see Sec. 2.2).

The emitted signal decreases again for angles beyond the critical, since the photon intensity is deposited in deeper regions inside the material.

Data were collected for several energy points and the $G(\theta)$ curves at each energy were fitted for δ, β, L using a least-squares algorithm with best fit criterion the statistic

$$S = \sum_{i=1}^{N} \frac{[G'(\theta_i) - G(\theta_i)]^2}{\sigma_i^2}, \tag{4.16}$$

in the same manner as was explained in Sec. 4.4, for the case of reflectance measurements for Si. The fitted values of δ, β, from the photoemission measurements are shown in Figs. 4.19 (a), (b). The values from photoelectric yield measurements from ref. 12 are also shown in Fig. 4.19 (b). The agreement with the present measurements is partially good; the authors in ref. 12 acknowledge the presence of oxide on the Si wafer from which data were taken. Fitting photoelectric yield data has the disadvantage of one extra parameter, the escape depth L. Fitted values of L using this method are not always meaningful. Furthermore, it has been found [34] that the ability of the fitting algorithm of eq. (4.16) to obtain accurately δ, β, L is sensitive to the ratio L/λ at each energy point (in the same way that the ratio β/δ was found to affect the efficiency of the reflectance method, in Sec. 4.4). By drawing consecutive curves of constant $G(\theta)$ in $\epsilon_1 - \epsilon_2$ space ($\epsilon = \epsilon_1 + i\epsilon_2$ being the dielectric function) for different values of the parameter L/λ, the authors in ref. 34 have concluded that fitting of ϵ_1, ϵ_2 (equivalent to δ, β) is effective for $\lambda >> L$, while for wavelengths $\lambda \approx L$ the fitting is sensitive only to data $G(\theta)$ from a small range of grazing incidence angles. For instance, in these measurements, the fitted results for δ, β in the region 200 - 300 eV were noisy and sensitive to the range of angles chosen for the fitting, and therefore they are not used in Fig. 4.19 (a). An advantage of the photoelectric yield method over the reflectance, is its insensitivity to roughness *, which degrades reflectance measurements and makes reflectance data practically useless at large grazing angles of incidence. Thus, although the photoelectric yield method does not always guarantee successful results in the cases where the reflectance method fails, it can always be

*This is true assuming moderate values of the roughness and large spatial periods of the imperfections on the sample surface. Under these conditions, the sum of specularly reflected and diffusely scattered light is equal to the specularly reflected light from a perfectly smooth surface.

used as an independent method, or to verify the results obtained by the reflectance method on a bulk sample.

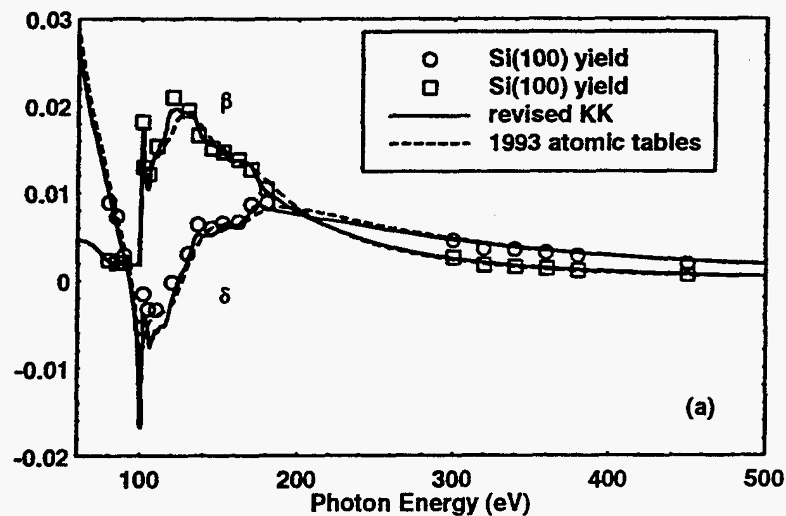

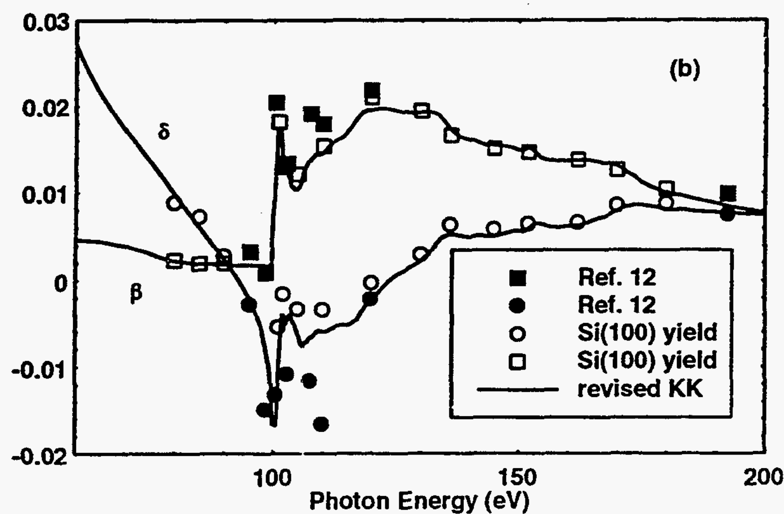

Figure 4.19: (a) The results of the fitting of δ, β from the present photoelectric yield measurements on Si.The data are in quite good agreement with the revised atomic tables for Si, after the new Kramers-Kronig (KK) calculations were performed (see previous section). (b) The results of (a) are shown in detail in the region 60 - 200 eV, and photoelectric yield data from ref. 12 are superimposed. The agreement is good for data points around 95, 100, 120 and 190 eV.

4.7 Conclusions

Reflectance data for the optical constants of crystalline and amorphous silicon in the region 50 - 180 eV are presented in this paper. Surface analysis and photoelectric yield measurements show that a two-step procedure, including UV irradiation and subsequent HF etching of the samples, is successful in removing carbon contamination and native oxide and in achieving hydrogen passivation of the sample surface. A least squares fitting algorithm is used in order to derive the optical constants δ, β from the experimental data; this method is reliable only in regions where β/δ is sufficiently small, while producing results with large uncertainties in the energy range where $\beta/\delta \geq 1$. The effect of the β/δ ratio in the fitting of a reflectance curve has a purely mathematical nature, thus, the above reliability criteria should apply to the fitting of reflectance data from any material in any energy range. However, the exact value of β/δ which marks the boundary between reliable and uncertain fitting should depend on the particular experimental conditions and therefore it has to be determined separately in each case. In this experiment, reliable data are obtained in the range 50 - 90 eV (below the silicon $L_{2,3}$ edge at 99.8 eV), corresponding to $\beta/\delta \leq 0.5$. It is shown that crystalline Si exhibits structure from 60 to 80 eV, also observed in previous transmission data. Furthermore, when the fitted values for δ are compared to the tabulated values [3], it is demonstrated through the sum rule that the tabulated values in ref. 3 overestimate δ because of missing oscillator strength in the absorption coefficient data used. This effect is verified by the present reflectance results for δ. The above discussion suggests that least squares fitting of reflectance data may not be a suitable method for the determination of the refractive index in certain energy regions; different techniques should be explored in the regions where the fitting algorithm becomes problematic. For Si in particular, there is a need for improved measurements in the region above the $L_{2,3}$ edge, where the reflectance method fails to provide reliable results. The photoelectric yield method is attempted as an alternative technique in this energy region, with partially successful results; it is found that fitting of angle-dependent photoelectric yield data has weaknesses similar to the reflectance method, and also involves the escape depth as a third parameter

necessary for the fit, in addition to δ, β. It could be possible to obtain improved data for Si in the energy range above the $L_{2,3}$ edge , by means of transmission measurements on very thin, free-standing films, using a radiation source with adequate photon flux such as beamline 6.3.2 at the ALS.

Chapter 5

Molybdenum

5.1 Introduction

Molybdenum has emerged as an important material for EUV lithography applications, due to its implementation as the absorber layer for Mo/Si and Mo/Be multilayer mirrors. These optics operate at energies below the Si $L_{2,3}$ edge (99.8 eV) and the Be K edge (111.5 eV) respectively, where silicon and beryllium exhibit low absorption. In order to successfully predict the performance of these mirrors, precise knowledge of the optical properties of their materials is required. Information on the dispersive and absorptive behavior of each material can be obtained from the real and imaginary part of the energy dependent refractive index n, which has to be measured to a great degree of accuracy. A collection of experimental data from previous workers [14,15] for the refractive index of Mo from 0.1 to 37 eV, derived from calorimetric and reflectance measurements, has been published in the "Handbook of Optical Constants of Solids" [13]. Windt *et al.* [16,17] have also provided reflectance data in the range 10 - 928 eV. In the infrared and visible regimes, reflectance measurements are relatively insensitive to surface oxide, contamination and roughness. On the other hand, reflectance data may be severely influenced by these factors in the EUV and soft x-ray regions, as discussed in the previous chapter for the case of silicon. All authors in the aforementioned references acknowledge the presence of roughness, oxide and contamination on the surface of their Mo samples. The au-

thors in refs. 16, 17 have measured the roughness and have included it in the fitting model for the experimental reflectance curves. However, its presence combined with the surface oxide and contamination is expected to lead to uncertainties or errors in the determination of the refractive index (see discussion in Sec. 4.2 for the case of silicon). The above published optical data for Mo have been used in combination with theoretical calculations [11], in order to determine the imaginary part of the refractive index of Mo in the range 10 - 30,000 eV in the 1993 atomic tables [3]. The real part is then calculated through dispersion (Kramers-Kronig) analysis, as explained in Sec. 2.1. It should be noted that the values for n in these tables have been determined according to the independent atom approximation, which is not true at low energies and around absorption edges, as discussed in Sec. 2.1. Therefore, it is expected that the interpolations and calculations used for the tabulated values will smooth out the fine structure surrounding absorption thresholds, if detailed measurements are not available in these regions.

The tabulated optical constants δ, β of molybdenum are tested for accuracy and self-consistency through the sum rules of eqs. (2.70)-(2.72). Fig. 5.1 shows the results for $N_{eff,\beta}$ according to eq. (2.71), using the data in the 1993 atomic tables. The result is $N_{eff,\beta}(\omega \rightarrow 0) = 2.3$ electrons, while accurate data should yield $N_{eff,\beta}(0) = 0$, as explained in Sec. 2.4. Furthermore, the results of the ϵ_2 and $Im\{-\epsilon^{-1}\}$ sum rules, eqs. (2.70), (2.72), demonstrate inconsistencies below 40 eV in the calculated values of δ from the Kramers-Kronig relations in the 1993 atomic tables. The reason for these errors is the lack of reliable experimental data for molybdenum. Especially in the EUV/soft x-ray range, most of the published experimental values are obtained from reflectance measurements [13,16,17], which are subject to large deviations from the true values of the optical constants due to surface roughness and contamination. On the other hand, photoabsorption data are insensitive to micro-roughness (see Ch. 1, Table 1.1, Sec. 2.2) and can be corrected for surface contamination and oxide, as it is going to be shown in later sections in this chapter. Thus, transmission measurements provide an alternative approach for obtaining optical constants in this energy region, if thin unsupported films are possible to fabricate.

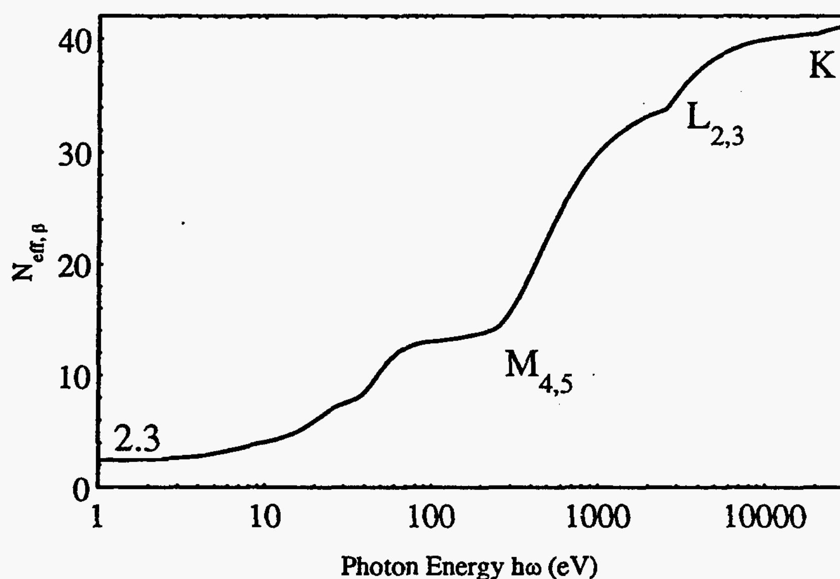

Figure 5.1: Calculation of $N_{eff,\beta}$ vs. photon energy for Mo according to the partial sum rule of eq. (2.71), using a collection of previous experimental data and calculations for β [3,13]. The formulation of eq. (2.71) imposes that $N_{eff,\beta}(\omega \rightarrow \infty) = Z^*$ (for Mo, from eq. (2.52), $Z^* = Z - \Delta = 42 - 0.2 = 41.8$), independently of the values used for β. On the other hand, eq. (2.71) gives $N_{eff,\beta}(\omega \rightarrow 0) = 0$ only if accurate data are used, thus, the result $N_{eff,\beta}(\omega \rightarrow 0) = 2.3$ implies inaccuracies in the values for β in refs. 3, 13.

5.2 Sample Preparation

The samples used for the photoabsorption measurements consisted of a Mo film enclosed between two thin C layers ($\approx$ 145 Å), in order to prevent oxidation. Samples were deposited by magnetron sputtering with 2.5 mTorr of argon, in a chamber with a base vacuum pressure of 10^{-6} Torr. Since the sputtering system allowed for multiple target materials, each C/Mo/C sample was fabricated during a single run, without contact with air between each layer deposition. The substrate used was a Si(111) wafer coated with photoresist (Microposit^R, consisting of 82% 2-ethoxyethyl acetate, 9% n-butyl acetate and 9% xylene) to assist in the removal process and baked in 100° C for 30 min prior to deposition. Five different Mo thicknesses were fabricated, ranging from 300 Å to 1900 Å. Support rings with an open area of 7 mm^2 were attached to the films using an acetone resistant glue and the supported films were removed from the substrate by soaking in acetone.

The thicknesses of C and Mo were verified using reflectance measurements on the samples prior to removal, at the Cu K_α (8047.8 eV) and Al K_α (1486.7 eV) energies. Each reflectance curve was fitted using the Fresnel equations for a three layer system, using the carbon and molybdenum thicknesses and the interfacial roughness as parameters in the model. For 4 of the 5 samples fabricated, this procedure yielded Mo thickness values of 305, 460, 925 and 1510 Å respectively, with an accuracy of $\pm$ 2%. The carbon layer thickness took values between 140 and 145 Å. In the case of the thickest sample, reflectance measurements with the available radiation sources produced very low visibility fringes, therefore fitting was not possible and the nominal thickness was assumed for the Mo layer (1900 Å), as determined from the sputtering process.

5.3 Transmission measurements

Transmission measurements on the five free standing C/Mo/C foils were performed in the energy range 60 - 930 eV, with steps ranging from 2 eV down to 0.25 eV in regions where fine structure was present. Measurement reproducibility was better

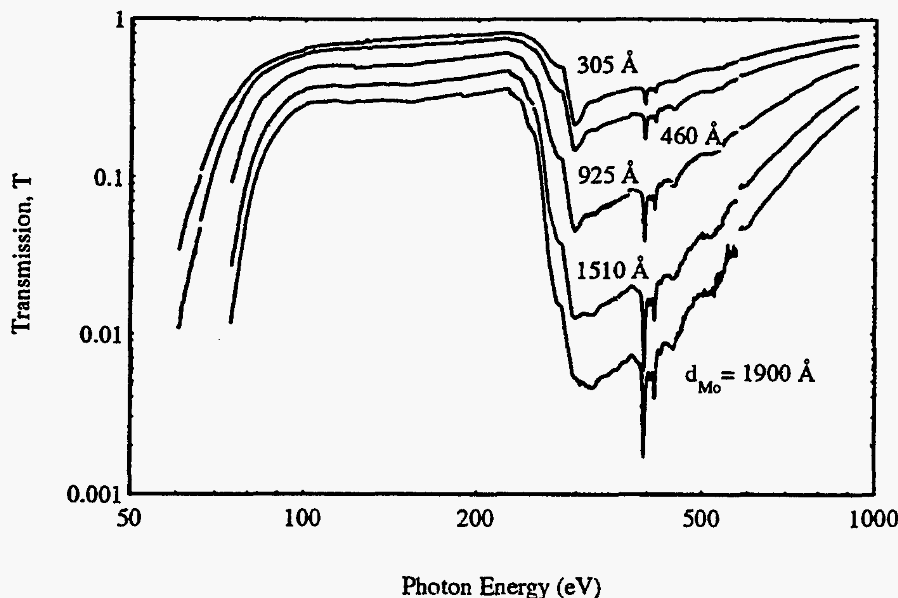

Figure 5.2: Transmission data from the five C/Mo/C films are shown, corresponding to molybdenum layers of 305, 460, 925, 1510 and 1900 Å each, deposited between two 145 Å thick carbon layers.

than 0.5% except for the regions of very high absorption and the lowest energies, where it was around 1%. The results for the absolute photoabsorption are shown in Fig. 5.2. These curves were obtained by applying the expression $T = I/I_0$ for the transmission T of a foil, where I is the intensity transmitted through the sample and I_0 is the intensity of the direct beam (see also Sec. 2.2). The most pronounced features of the five transmission curves are the dip at the molybdenum $M_{4,5}$ edge (227.9 eV) and the structure around the molybdenum $M_{2,3}$ edge (394 eV).

The energy dependent absorption coefficient μ (cm^2/g) of molybdenum was obtained through eq. (2.26) for T, also displayed in Fig. 5.3. $\rho = 10.22$ g/cm^3 was used for Mo, x is the Mo thickness in the C/Mo/C foil and T_0 represents the transmission from layers of other materials present in the foil (in this case the two layers of carbon). An example of the μ determination procedure for a few different energies is shown in Fig. 5.3. For each energy, a plot of T vs. x was produced using the transmission results for the five different Mo thicknesses measured. Fewer samples were used at the energies where high absorption led to poor experimental data from the thick films. On a logarithmic scale for T, the experimental data points should form

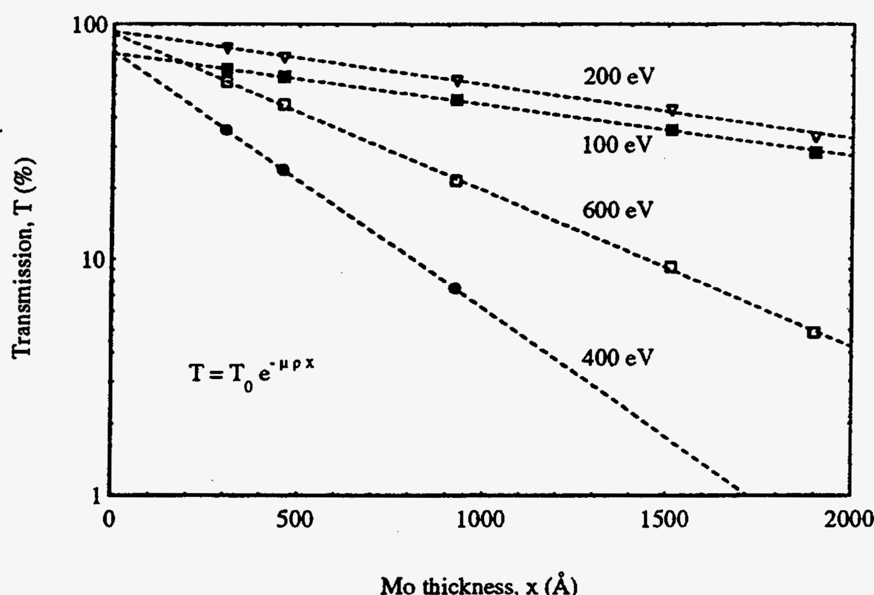

Figure 5.3: Fitting procedure for μ at 4 energies. The data points represent the transmission of the C/Mo/C foils plotted vs. Mo thickness. At 400 eV, high absorption prevented reliable measurements from the thick samples, so, only data from the foils with 305, 460 and 925 Å Mo thickness were used. The dashed lines represent the fit to the experimental results at each energy which yields the values of μ (cm^2/g) and T_0.

a straight line and its slope should yield μ according to eq.(2.26). In addition, the point of interception of the curve with the T axis (corresponding to zero molybdenum thickness) gives T_0, assuming that the carbon layer thicknesses are the same for all 5 samples used in the measurements. This assumption is indeed justified from the fitting results discussed in Sec. 5.2.

It is worthwhile examining a plot of the results for the carbon transmission T_0 vs. energy, shown in Fig. 5.4, since it provides information on the sample deposition conditions and the possible sources of contamination. The dip around 248.4 eV is attributed to the argon $L_{2,3}$ edge. It reveals the presence of a small amount of argon in the samples, coming from the Ar^+ ions used for target bombardment in the sputtering chamber. Similarly, it might be assumed that the reason for the feature at the oxygen K edge (543.1 eV) is the presence of oxygen in the chamber, which was incorporated in the foils during deposition. However, since this feature is absent from the results for the Mo absorption coefficient as shown in Fig. 5.5, it is concluded that there was no

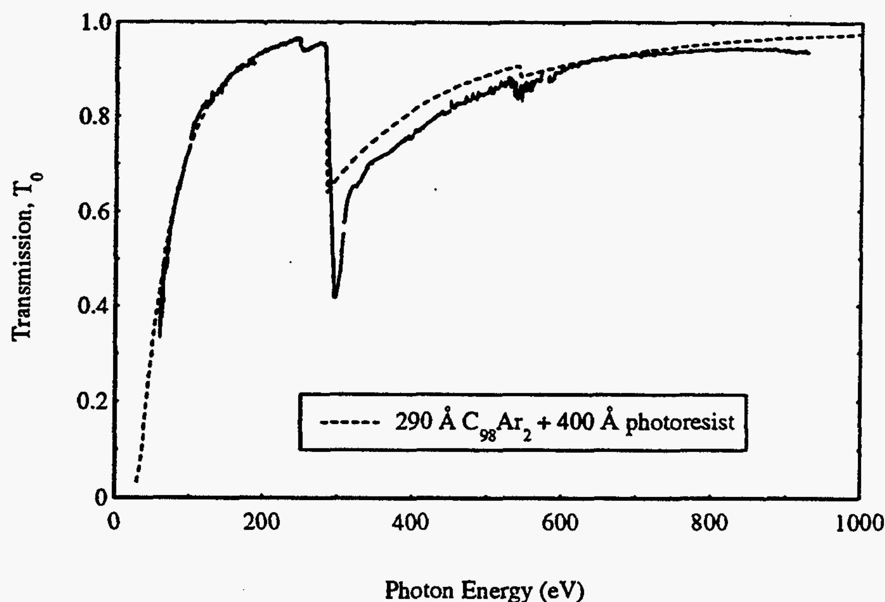

Figure 5.4: The results for T_0 are plotted vs. photon energy. The most prominent feature is the carbon K edge at 284.2 eV. The small edge at the Ar $2p_{3/2}$ energy (248.4 eV) indicates the presence of argon in the samples. The oxygen K edge feature at 543.1 eV is attributed to a layer of photoresist left on the samples. The experimental results are fitted to a calculated transmission of 290 Å of $C_{98}Ar_2$ with 400 Å of photoresist, shown with the dashed line.

oxygen present during the sputtering process. Another explanation for the appearance of oxygen in the results for T_0 could be that some photoresist was left on the foils after removal. The effect of this additional layer together with the carbon layers cancels out in the determination of μ using the above method. These conclusions were verified in a model calculation used to approximate the experimental results for T_0. It is illustrated in Fig. 5.4 that the experimental T_0 curve was found in quite good agreement with the calculated transmission of a film consisting of 290 Å of carbon with a 2% atomic content of argon (corresponding to the two carbon layers of 145 Å each in the C/Mo/C sample), and a 400 Å overlayer of photoresist. From the above discussion it is concluded that the molybdenum foils used to obtain the absorption coefficient were free of oxygen and contained no other significant contamination except for the aforementioned small amount of argon.

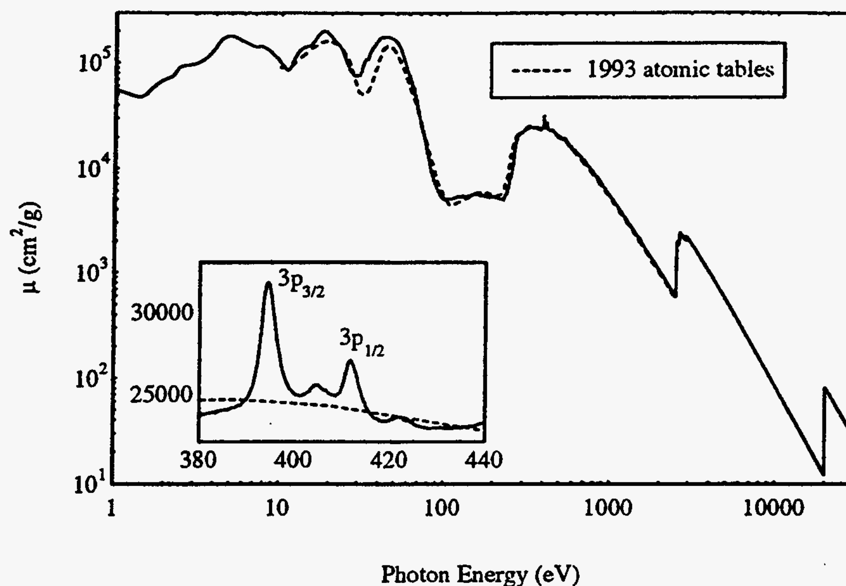

Figure 5.5: The new set of data for the Mo absorption coefficient from 1 eV to 30 keV is shown with the solid line. The values of μ in the range 60 - 930 eV are obtained from the present measurements. Data from refs. 13–15 are used in the low energy region (1 - 35 eV). In the rest of the spectrum, the values of the 1993 atomic tables are used with small corrections around the energy region of the present work. In the inset, the molybdenum $M_{2,3}$ structure and its deviation from the smoothed tabulated values are shown in detail.

5.4 Discussion

The absorption coefficient μ for Mo derived from the measurements in this work in the energy range 60 - 930 eV is plotted in Fig. 5.5. In order to construct a set of values for μ in the complete spectrum, values outside this range were obtained from previous work as follows: In the range 1 - 35 eV, experimental data from refs. 13–15 were used. From 35 to 60 eV, the values from the 1993 atomic tables were somewhat modified in order to agree better with the new absorption data starting at 60 eV. These modifications are justified, considering the uncertainties in the previous experimental data in this energy range, discussed in Sec. 5.1. For energies above 930 eV, the data for μ in the atomic tables were normalized by a 5% increase in the range 930 - 2520 eV (Mo $L_{2,3}$ edge), in order to obtain a smooth transition between the new absorption data below 930 eV and the values in the atomic tables above 930 eV. The

values for the absorption coefficient used in the atomic tables are shown in Fig. 5.5 as a dashed line. The structure due to the splitting of the Mo $3p_{1/2}$, $3p_{3/2}$ peaks, which was absent from the simplified calculations in the atomic tables, is revealed in the new absorption measurements.

Fig. 5.6 (a), (b) shows the optical constants δ, β of the refractive index n for molybdenum, obtained from the new set of absorption data. The values of β were determined from μ through

$$\beta = \mu \; (\lambda\rho/4\pi) \tag{5.1}$$

where λ is the wavelength of the radiation. δ was then calculated from dispersion (Kramers - Kronig) analysis according to eqs. (2.50), (2.10). The new set of results for δ, β includes the region from 1 to 30 eV, which does not exist in the 1993 atomic tables.

A first check of the accuracy of the the absorption data can be made by applying the sum rule for $N_{eff,\beta}(\omega)$. The results are plotted in Fig. 5.7 (a), together with the previous calculation of $N_{eff,\beta}$ using the data from the 1993 atomic tables. It is shown that the previously missing oscillator strength of 2.33 electrons is now completely recovered, since the new absorption data yield the correct result $N_{eff,\beta}(0) \rightarrow 0$ for $\omega \rightarrow 0$, in agreement with the requirements of eq. (2.71). This indicates that the measurements and data compilation in this work resulted in an improved set of values for the absorption coefficient of molybdenum, compared to the 1993 atomic tables. In order to examine the consistency of the new Kramers - Kronig calculations for δ, the sum rules for $N_{eff,\epsilon_2}, N_{eff,\epsilon^{-1}}$ are also applied as shown in Fig. 5.7 (b). The results for $N_{eff,\epsilon_2}, N_{eff,\epsilon^{-1}}$ are consistent with the theory discussed in Sec. 2.4 throughout the energy range 1 eV - 30 keV. This indicates that the dispersion analysis with the new absorption data gave acceptable values for δ in the whole spectrum. Compared to the calculations in the atomic tables, the values for δ were improved and the low energy range was extended down to 1 eV.

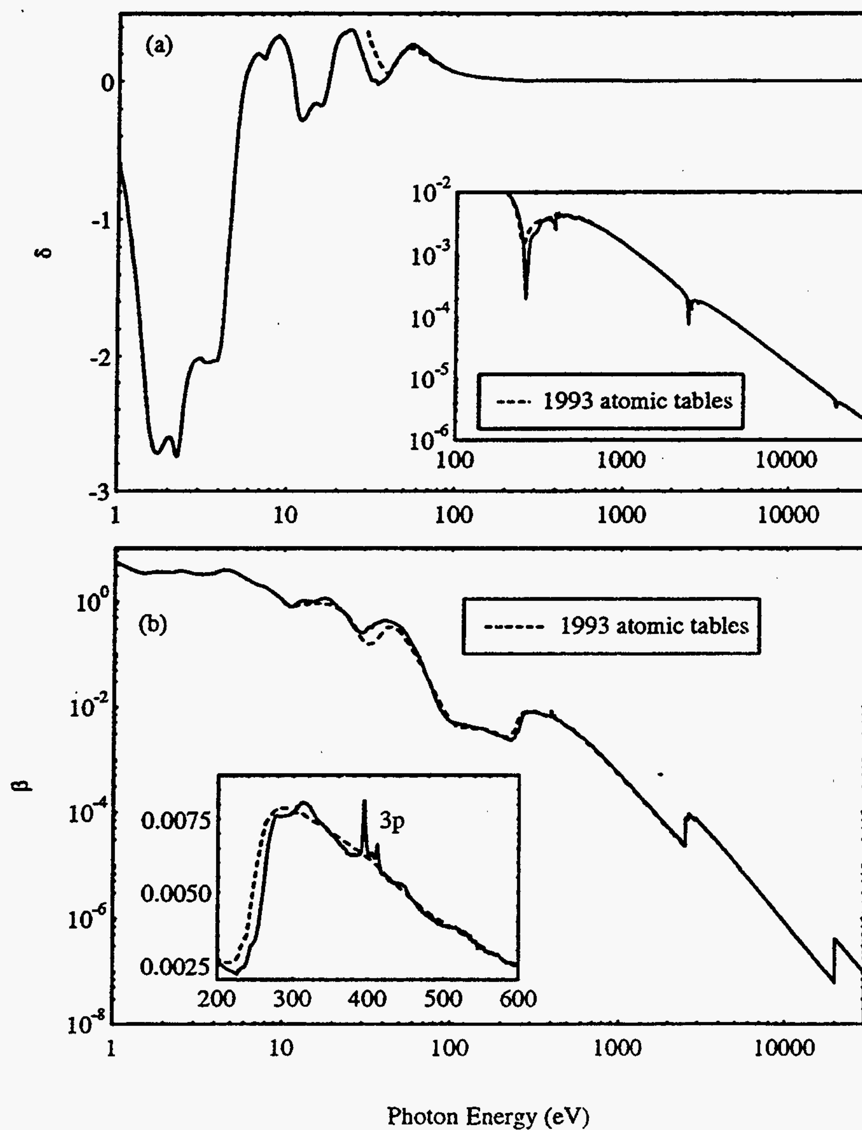

Figure 5.6: The optical constants δ, β of the refractive index $n = 1 - \delta + i\beta$ are plotted vs. photon energy, using the new absorption data in the complete spectrum. (a) δ is calculated from dispersion analysis and (b) β is derived directly from μ. The values in the 1993 atomic tables [3] are also shown (dashed line) for comparison.

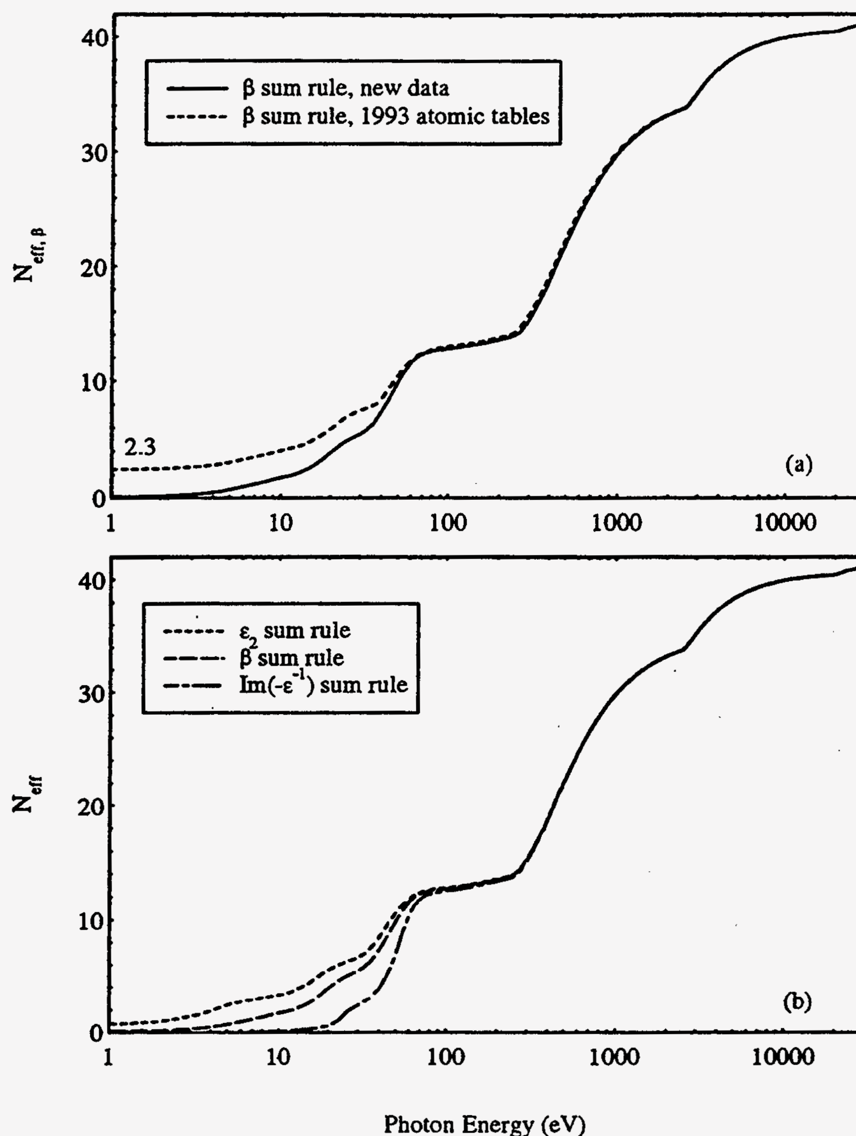

Figure 5.7: (a) The β - sum rule is shown for the new Mo absorption data (solid line) and for the data from the 1993 atomic tables (dashed line). As the photon energy approaches 0, there is an oscillator strength deficiency of 2.3 electrons in the tabulated values. The new data give the correct result of zero electrons. (b) The sum rules for ϵ_2, β, $\text{Im}\{-\epsilon^{-1}\}$ are shown, using the values from the new set of data. In the low energy region, they behave exactly as predicted by the theoretical model discussed in Sec. 2.4, Fig. 2.4. The agreement of all three sum rules at the energies above the first Mo core absorption level demonstrates self-consistency among all the calculations performed.

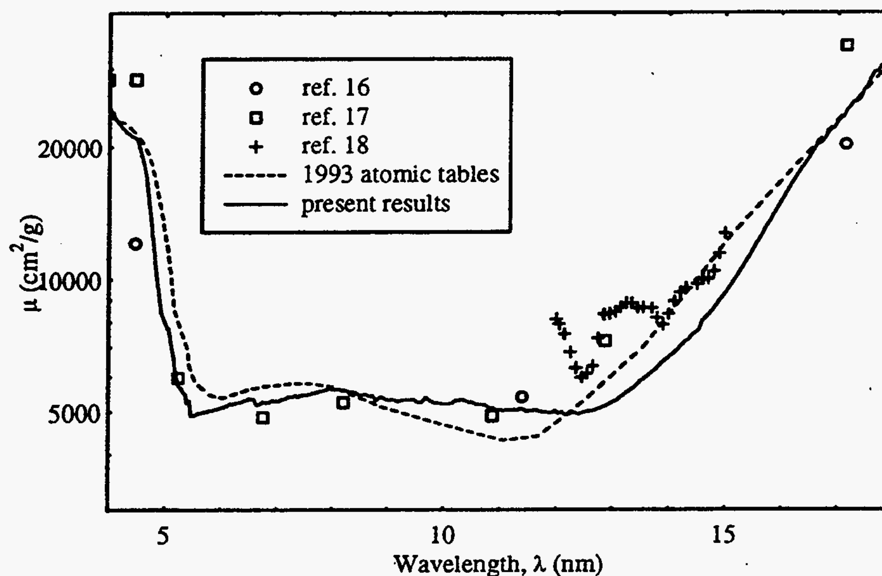

Figure 5.8: The new experimental values for μ (solid line) are shown in comparison with previous reflectance data from refs. 16–18 in the wavelength range of interest for Mo/Si and Mo/Be multilayer mirror applications. The values in the 1993 atomic tables (dashed line) in this range were based on refs. 16,17 combined with theoretical calculations [11].

5.5 Mo-based Multilayer Mirrors

The energy region below the Si $L_{2,3}$ edge (99.8 eV) and below the Be K edge (111.5 eV), corresponding to wavelengths longer than 12.4 nm and 11.1 nm respectively, is of particular importance for applications since it is the range of operation of the Mo/Si and Mo/Be multilayer mirrors fabricated for EUV lithography. Compared to the tabulated values, the new measurements produced lower values for the absorption in the Mo/Si wavelength regime and higher values in the Mo/Be regime, as shown in Fig. 5.8. The experimental data from refs. 16,17 are too sparse and are subject to large uncertainties, due to the effects of roughness and surface contamina-

tion in the reflectance measurements. The same effects are present in the data from ref. 18. It should also be noted that Mo samples in ref. 16 were made by evaporation, while sputtering was used for the samples in refs. 17, 18 (different deposition conditions often affect the optical properties of the material, to some extent). The values of δ in this wavelength range did not change significantly after the new dispersion calculations. Fig. 5.9 (a) shows the calculated reflectivity vs. wavelength for a typical Mo/Si multilayer mirror used in lithography applications. At 13.4 nm (the wavelength of choice for EUV lithography optics) the theoretical value of the reflectance at the Bragg peak was increased by 2% with the new molybdenum absorption data. The same procedure is applied in Fig. 5.9 (b) for Mo/Be mirrors. It is shown that for wavelenghts just longer than 11.1 nm, the reflectivity is lower with the new absorption values. These improved calculations using the theoretical model should lead to better fitting of experimental multilayer reflectance results, which is essential for the testing of the performance of these mirrors. Fig. 5.10 demonstrates the effect of the new, lower values for the Mo absorption around 13.4 nm in the fitting of multilayer experimental data. The experimental Bragg reflectance of a Mo/Si multilayer mirror measured at the ALS has been fitted to a theoretical model using the Mo/Si layer thickness d, the ratio Γ of Mo thickness in the layer and the interlayer roughness σ as adjustable parameters. Such parameters characterize the experimental conditions during the mirror deposition. The calculations were performed for two sets of Mo optical constants: the 1993 atomic tables and the revised tables using the present photoabsorption measurements. The results show that both sets of optical constants for Mo were able to produce a very good fit to the experimental data. However, they achieved it by producing two different sets of d and Γ. Thus, since by fitting experimental data one aims in obtaining information (or in verifying) the experimental conditions during the fabrication of the mirror, it is important to use accurate values for the optical constants in order to obtain meaningful results from the fit.

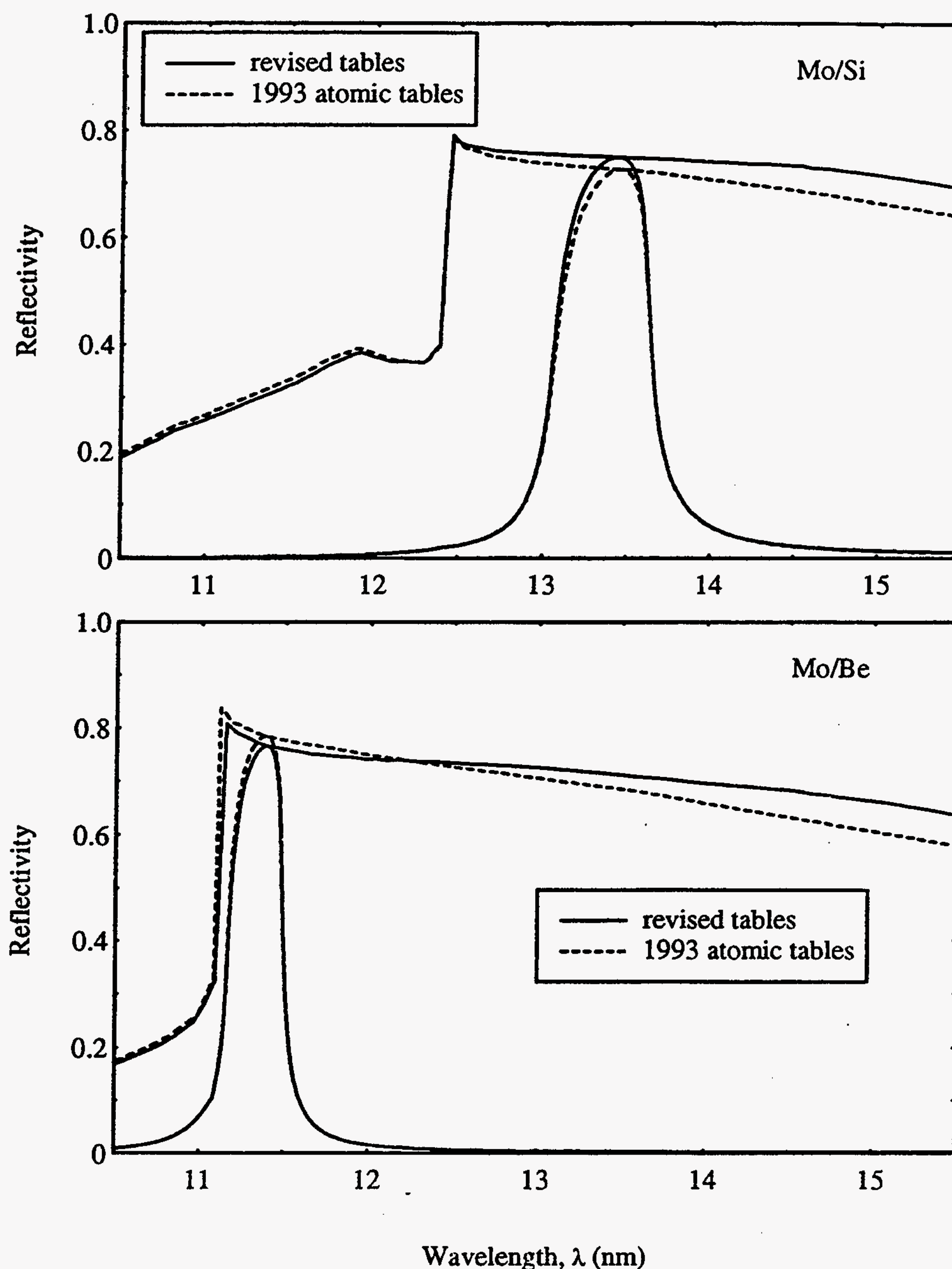

Figure 5.9: The envelope of peak (Bragg) reflectivities at normal incidence for an infinite multilayer stack of Mo/Si and Mo/Be is plotted vs. wavelength. The ratio of the Mo thickness to the multilayer period was 0.4 and the period was optimized for each wavelength point. The Bragg peak is shown in detail for a Mo/Si mirror with 6.87 nm period and for a Mo/Be mirror with 5.75 nm period. These theoretical calculations predict the reflectance to be 2% higher for Mo/Si and 1.8% lower for Mo/Be, compared to calculations using the values in the 1993 tables [3].

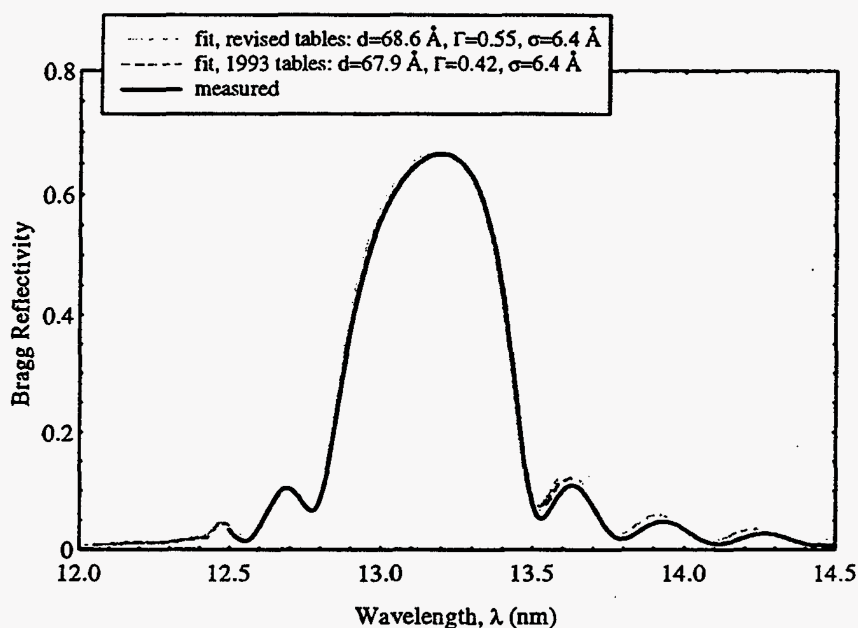

Figure 5.10: Fitting of the measured reflectivity vs. wavelength (solid line), for a Mo/Si mirror (40 layer pairs) at normal incidence. This optic was fabricated by C. Montcalm and measured by C. Montcalm and D. Gaines (Lawrence Livermore National Lab), at the ALS and at the BESSY synchrotron source. The difference in the absorption values around the Bragg peak in the two sets of optical constants used for the fitting, led to two different estimates for Γ and d. A simplified model of the multilayer structure was used, just to demonstrate the effect of optical constants in the fitting of Γ and d.

5.6 Conclusions

Precise transmission measurements in the range 60 eV - 930 eV for the determination of the optical constants of molybdenum are presented in this work. The results reveal the fine structure in the absorption coefficient of Mo around the $M_{2,3}$ edge. The new experimental data also give different values for the absorption in the range 11 nm - 14 nm, which is important for normal incidence Mo/Be and Mo/Si multilayer mirror applications. A complete set of absorption data in the range 1 - 30,000 eV is formed by using the new measurements and previously published values [3,13–15] in order to apply the Kramers - Kronig relations for the real part of the refractive index. Sum rule tests show that the missing oscillator strength from the absorption coefficient in the 1993 tables is recovered and that the new set of optical constants is self-consistent. The results presented have been used in order to revise the atomic scattering factors for Mo which are available on the World Wide Web [27].

Chapter 6

Beryllium

6.1 Introduction

Beryllium has been studied in the past [21] as a material useful in EUV astronomy observations; its continuously increasing transmission in the wavelength range from 1000 Å down to the Be K edge (111.2 Å), makes it a suitable component of bandpass filters operating in this region. Furthermore, as a light metal with relatively simple band structure, Be has been a favorable material for K edge EXAFS investigations, by means of photoabsorption [54,55] and x-ray Raman scattering [56,57] experiments. Recently, there has been increased interest in Be due to the high reflectivity achieved by Mo/Be multilayer mirrors [1,25] at wavelengths just longer than the Be K edge, establishing them as potential optics for EUV lithography (see also discussion in Ch. 1 and Sec. 5.5).

A compilation of previously published values for the optical constants of Be in the range 0.06 - 250 eV has been performed in the "Handbook of Optical Constants of Solids II" [19]. In the 1993 atomic tables [3], the values for the Be absorption coefficient in the range 10 - 30,000 eV are based mostly on photoabsorption calculations [11]; experimental data points were interpolated in the region from 111.5 eV (Be K edge) to 10 keV. In Fig. 6.1, the absorption sum rule of eq.(2.71) is applied using the data for β from the 1993 tables in the energy range above the Be K edge, combined with data from ref. 19 in the low energy range (from 0.06 eV to the Be K edge). The

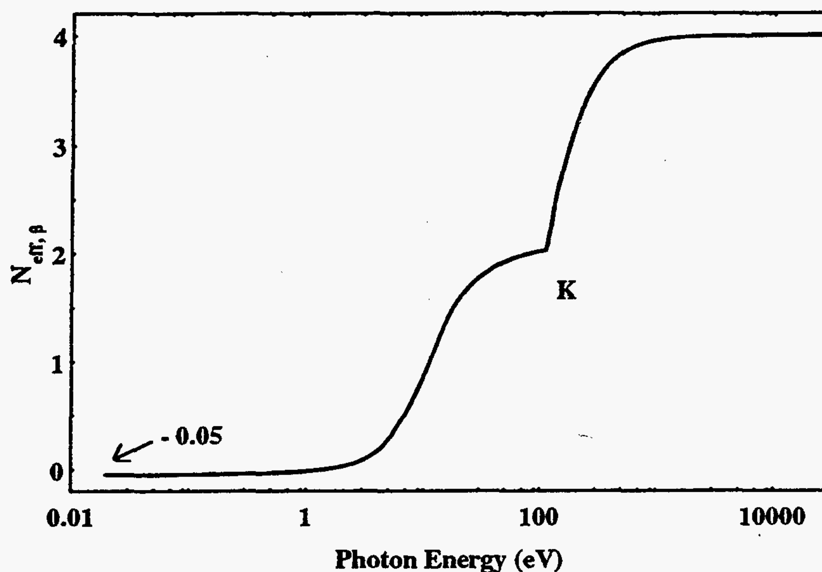

Figure 6.1: Calculation of the sum rule of eq. (2.71) for Be, using data for β from ref. 3, 19 in the range 0.06 - 30,000 eV. At $\omega \rightarrow 0$ the sum rule yields -0.05 electrons, which means there is excess oscillator strength in the absorption values for Be in some region of the spectrum.

result is $N_{eff,\beta}(\omega \rightarrow 0)$ = -0.05 electrons, while $N_{eff,\beta}(\omega \rightarrow 0) = 0$ would be expected from an accurate set of data (see Sec. 2.4). Thus, there are deficiencies in the published experimental data, resulting in an excess oscillator strength (see formulation in eq.(2.71)) equal to 1.25% of the total number of electrons $Z = 4$ of Be, and leaving room for improved absorption measurements for this material. For instance, the authors in ref. 19, 55 acknowledge error bars of up to ± 20% in their experimental values for β. Apart from the usual difficulties associated with thin film fabrication for photoabsorption measurements in the EUV/soft x-ray range, discussed in Ch. 1 and Sec. 5.1, Be has an additional pitfall: in powder form it is toxic, thus it requires specially equipped facilities for thin foil deposition and handling. Such facilities exist at Lawrence Livermore National Lab (LLNL), where collaborators [1,25,58] have produced

the Be foils used for the transmission measurements presented in this work.

6.2 Sample Preparation

The samples used for the measurements were fabricated at LLNL [25,58]. Be was deposited on an approximately 500 Å thick silicon nitride membrane, using a DC magnetron sputtering system. The stoichiometry of the membrane was 10(Si) : 11(N) and its density was determined at the time of fabrication to be $\rho \approx 3$ g/cm^3. The membranes were deposited on a Si(111) 4-inch wafer, using the "low pressure chemical vapor deposition" (LPCVD) method. A 10% thickness gradient was present throughout the wafer surface, and about 10% reproducibility was achieved between membrane depositions on several wafers, using this technique [58]. A grid of 5 × 5 membrane windows was patterned with photoresist and etched on the wafer, using the "parallel plate reactive ion etching" technique. Each window had a 1.25 × 1.25 mm^2 size. Be was then sputtered on the wafers, using an Ar^+ discharge; TEM studies have shown [25] that this deposition procedure results in Be foils of crystalline structure. 4 different thicknesses were deposited, with nominal values equal to 105, 210, 316 and 632 Å. Thus, free-standing Be/silicon nitride windows were prepared for the transmission measurements.

Reflectance measurements at 90 and 95 eV were performed on the coated Si wafers in order to determine, through fitting of the experimental curves, the thickness and density of Be on the samples. Due to the thickness non-uniformity of the silicon nitride layers, a spot very close to the actual window used for the transmission was chosen for the reflectance measurements on each wafer. The fitting also included as parameters the thickness and density of: Silicon nitride, BeO (grown on Be upon exposure in air) and SiO_2 (native oxide on the Si wafer) layers. This method, used in all four samples, yielded $\rho_{Be} = 1.65$ g/cm^3 and Be thicknesses of 90, 202, 320 and 627 Å, respectively, with about 1% accuracy. Silicon nitride took values ranging from 400 to 450 Å in the four samples and its density was fitted to $\rho_{Si_{10}N_{11}} = 2.9$ g/cm^3. BeO thickness was fitted at values ranging from 35 to 40 Å and at a density of ρ_{BeO} = 1.6 g/cm^3, consistent in all four samples. SiO_2 was found to be 10 Å thick with a

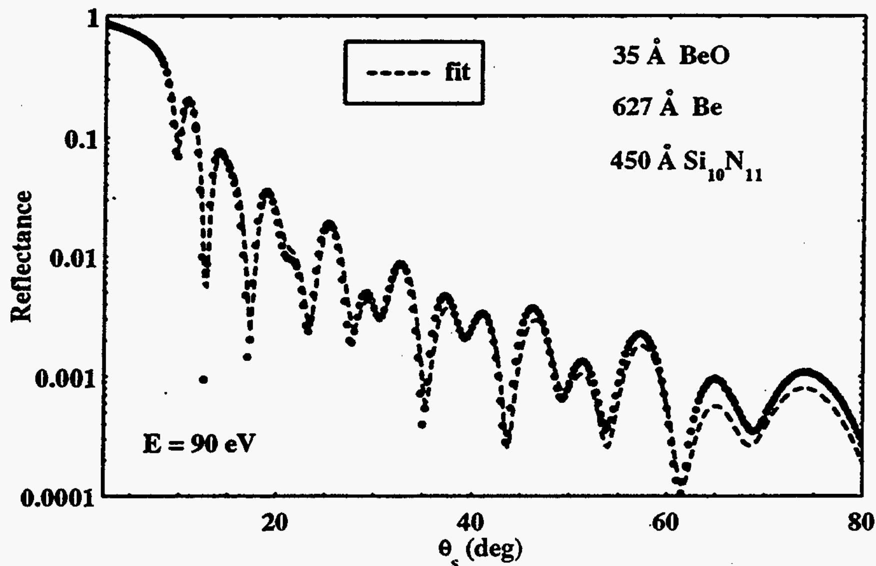

Figure 6.2: Fitting of experimental reflectance data (o-points) at 90 eV from a Be/$Si_{10}N_{11}$ film deposited on a Si(111) wafer, aiming in the determination of the thickness and density of Be. The nominal thicknesses of the two layers, as reported by their manufacturers, were 632 Å for Be and 500 Å for $Si_{10}N_{11}$. The results of the fit are: For Be, thickness $d = 627$ Å, density $\rho = 1.65$ g/cm^3. For $Si_{10}N_{11}$: $d = 450$ Å, $\rho = 2.9$ g/cm^3. A BeO layer was assumed on top of Be, fitted at $d = 35$ Å, $\rho = 1.6$ g/cm^3. Native oxide SiO_2 was assumed on top of the Si wafer, fitted at $d = 10$ Å, $\rho = 2.2$ g/cm^3. For the Si wafer, $\rho = 2.33$ g/cm^3 was used. An interface roughness of 2 Å was assumed for all layers. The "fringes" of the reflectance curve are the result of interference among reflected rays from the various layers in the sample.

density of $\rho_{SiO_2} = 2.2$ g/cm^3. Interlayer roughness of 2 Å was used in the fitting. An example of the fitting results is shown in Fig. 6.2.

6.3 Transmission measurements

Photoabsorption measurements at the ALS beamline 6.3.2 were performed in 0.5 eV steps in the energy range 50 - 930 eV, on the free-standing Be/silicon nitride films, for the 4 different Be thicknesses shown in Fig. 6.3. On each coated Si wafer, a window in the 5 × 5 grid was chosen and the transmission $T = I/I_0$ was measured. Because of the small size of the windows, the edges of the photon beam (mostly "tails" due to scattered light from the beamline), especially in the horizontal direction, were partially blocked by the window; it was found that 1.2% of the signal was "chopped off" in this way. For this reason, an empty (open) window was used for the normalization (I_0) measurements, instead of the direct beam. Measurements of T were reproducible to better than 0.4% during this experiment. The procedure presented in Sec. 5.3 and eq. (2.26) were used to determine the absorption coefficient μ vs. photon energy, for Be. The density $\rho_{Be} = 1.65$ g/cm^3, determined from the fitting of reflectance data presented in the previous section, was used for μ. In order for this method to be successful in determining μ, it is required that any additional layers apart from Be in the foil (in this case BeO, silicon nitride) have the same thickness in every sample. In other words, T_0 of eq. (2.26) should remain a constant (see also Sec. 5.3). In the present set of foils, this is true within a margin of a few percent, as explained in the previous section. This uncertainty did not seem to have a serious effect in the determination of μ, as no inconsistencies were noted during the fitting of μ at each energy.

The results for μ are shown in Fig. 6.4, superimposed to the values in the 1993 atomic tables. Due to their relatively small thicknesses, in the energy regions of low absorption (below the Be K edge and above about 250 eV) all four samples exhibited high transmission values, very close to each other, as is shown in Fig. 6.3. In these regions, the fitting algorithm discussed in Sec. 5.3, Fig. 5.3, had difficulty determining the slope of the "transmission vs. Be thickness" curve, i.e. μ, and gave very noisy

results; thus, the results of the present measurements from these regions were omitted in Fig. 6.4 and only the data in the region 111.5 - 250 eV are shown. Due to practical difficulties with the deposition system, it was not possible to fabricate thicker samples for measurements in the regions of low absorption and measure them at beamline 6.3.2, in a timely manner before the completion of this thesis. Instead, in the energy region below the Be K edge, previous absorption data obtained from 0.5, 1 and 2 μm thick Be foils at CXRO's laser-plasma source * are shown. The data from ref. 19 are also superimposed, for comparison. In the region above the Be K edge, the present measurements reveal EXAFS fine structure, associated with transitions of 1s electrons to unoccupied states above the vacuum level and many-body effects [56,57]. As it was discussed in the case of Mo in Sec. 5.4, Fig. 5.5, such effects get smoothed out in the 1993 tables calculations, unless detailed experimental data have been interpolated. In the case of Be, there were some experimental data points available in the 1993 tables in the region above the K edge, however, the present measurements demonstrate the fine structure in more detail. In the region below the edge, there is large disagreement between the various experimental results and calculations shown. One of the possible reasons for the experimental data discrepancies may be the different deposition conditions used by various experimenters: For the present measurements, as well as for the measurements performed at the laser-plasma source*, Be foils were fabricated by DC magnetron sputtering; the authors in ref. 19 note that the Be samples from refs. 20,21 are made by evaporation and that optical properties depend critically on the evaporation technique used. Furthermore, the authors in ref. 21 acknowledge the presence of a BeO layer on their sample which is not normalized out of their results for the linear absorption coefficient of Be. However, it appears that the discrepancy between the compilation in ref. 19 and the laser-plasma measurements is too large to be attributed to sample preparation conditions only. Furthermore, it is demonstrated in Fig. 6.4 that the calculations (ref. 11) implemented in the 1993 atomic tables and the laser-plasma measurements are also in great disagreement. Since the energy region below the Be K edge is of interest for Mo/Be multilayer mirror applications,

*Unpublished measurements by Eric M. Gullikson.

as discussed in Sec. 5.5, more measurements on thick Be foils at beamline 6.3.2 are planned for this energy region and for the rest of the energy range of the instrument.

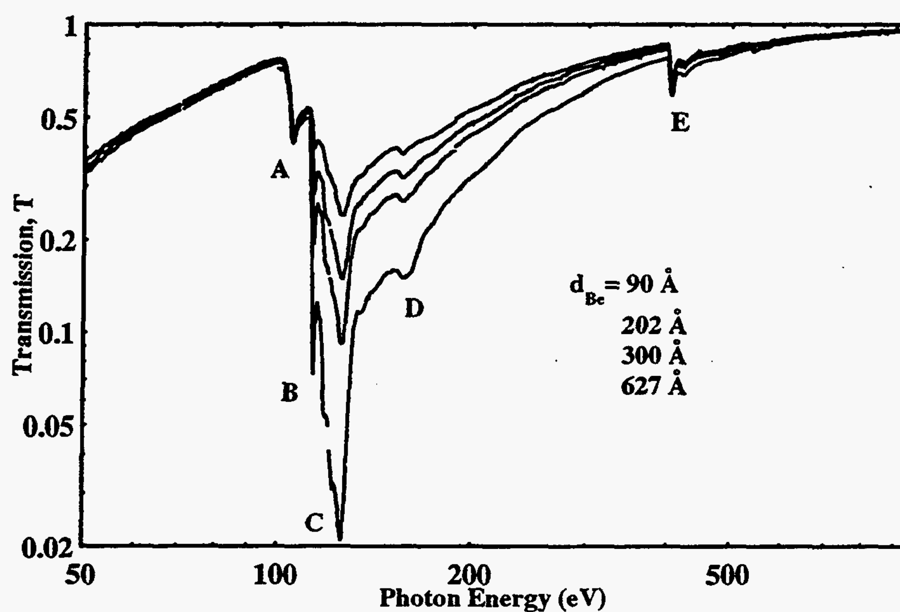

Figure 6.3: Transmission measurements on 4 Be samples, 90, 202, 300 and 627 Å thick respectively, supported on a silicon nitride membrane. 35 - 40 Å BeO is also expected to be present on top of Be. The presence of these additional layers in the Be samples cancels out in the determination of the absorption coefficient of Be, as explained in Sec. 5.3. Feature A in the transmission curves is attributed to the Si $L_{2,3}$ edge, B is the Be K edge, C is a feature of the silicon nitride absorption spectrum, D is the Si L_1 edge and E is the nitrogen K edge.

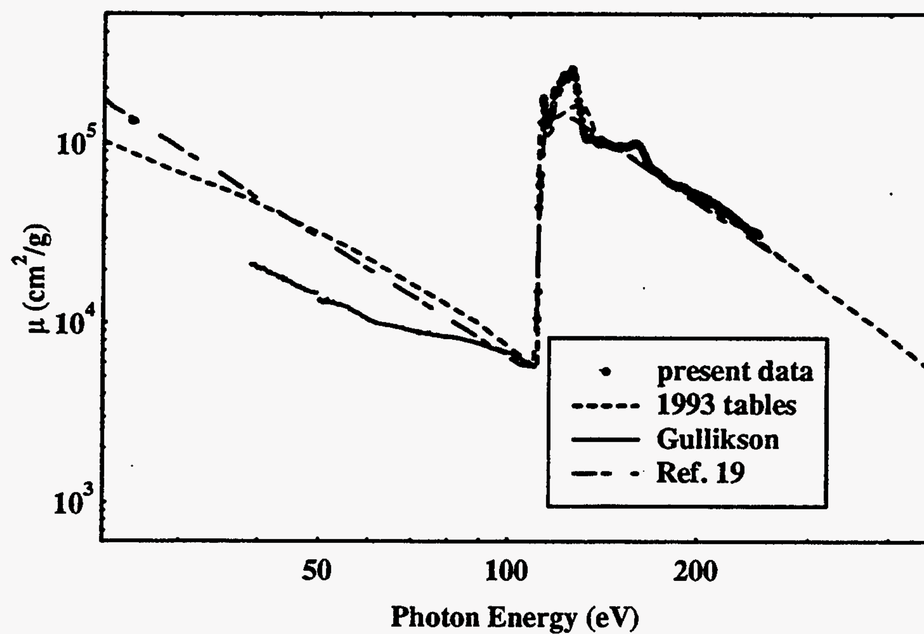

Figure 6.4: Values of the absorption coefficient of Be from different experimenters are shown, and the data from the 1993 tables are also used for comparison. All data shown in this figure are normalized, using eq. (2.23), to correspond to the tabulated value 1.8 g/cm^3 for the density of Be. The values from ref. 19 are compiled from previously published transmission measurements on evaporated Be samples [20,21]. The measurements denoted by the solid line were performed by E. M. Gullikson at CXRO's laser-plasma source, on sputtered Be foils provided by the authors in ref. 1.

6.4 Conclusions

New, improved photoabsorption measurements for Be are presented in the energy region from the Be K edge (111.5 eV) to 250 eV. EXAFS structure is present, also investigated in the literature [56,57] by means of x-ray Raman scattering. Due to practical difficulties, it was not possible to obtain absorption results of good quality in the region below the Be K edge (111.5 eV), which is of most interest for EUV applications. Data from previous experimenters in this range are plagued by large discrepancies, owing in part to different sample preparation conditions and sample contamination. Furthermore, the model of ref. 11 used for the calculations in the 1993 atomic tables [3], seems to be in serious disagreement with recent photoabsorption results, in the region below the Be K edge. Obviously, more measurements in this region are needed, so that an accurate data set for the absorption (β) of Be can be constructed in the entire spectrum and a self-consistent calculation of the dispersion relations (δ) can be performed.

Bibliography

[1] K. M. Skulina, C. S. Alford, R. M. Bionta, D. M. Makowiecki, E. M. Gullikson, R. Soufli, J. B. Kortright, and J. H. Underwood, "Molybdenum/beryllium multilayer mirrors for normal incidence in the extreme ultraviolet," Appl.Opt. **34**, 3727–3730 (1995).

[2] X. Lu, T. D. Nguyen, R. Soufli, E. M. Gullikson, and J. H. Underwood, "Microstructure, stress and optical properties of Ge/C multilayers," In *Tech. Digest, OSA Conference on the Physics of X-Ray Multilayer Structures, Jackson Hole, WY, March 14-17, 1994*, pp. 83–86 (1994).

[3] B. L. Henke, E. M. Gullikson, and J. C. Davis, "X-ray interactions: Photoabsorption, scattering, transmission and reflection at E = 50 - 30,000 eV, Z = 1 - 92," Atomic Data and Nuclear Data Tables **54**, 181–343 (1993).

[4] E. M. Gullikson and R. Soufli, unpublished measurements, beamline 6.3.2, ALS, 1995-7.

[5] D. Y. Smith and E. Shiles, "Finite - energy f - sum rules for valence electrons," Phys. Rev. B **17**, 4689–4694 (1978).

[6] E. M. Gullikson, J. H. Underwood, P. J. Batson, and V. Nikitin, "A soft x-Ray/EUV reflectometer based on a laser produced plasma source," X-Ray Sci. Technol **3**, 283–299 (1992).

[7] J. H. Underwood, E. M. Gullikson, M. Koike, P. J. Batson, P. E. Denham, K. D. Franck, R. E. Tackaberry, and W. F. Steele, "Calibration and standards beamline

6.3.2 at the Advanced Light Source," In *Conference on Synchrotron Radiation Instrumentation '95*, **67**, available in CD ROM only (1996).

[8] D. L. Windt, J. W. C. Cash, M. Scott, P. Arendt, B. Newnam, R. F. Fisher, A. B. Swartzlander, P. Z. Takacs, and J. M. Pinneo, "Optical constants for thin films of C, Diamond, Al, Si, and CVD SiC from 24 Å to 1216 Å," Appl. Opt. **27**, 279–295 (1988).

[9] M. Lampton, B. Margon, and S. Bowyer, "Parameter estimation in x-ray astronomy," Astrophys. J. **208**, 177–190 (1976).

[10] E. M. Gullikson, P. Denham, S. Mrowka, and J. H. Underwood, "Absolute photoabsorption measurements of Mg, Al, and Si in the soft-X-ray region below the $L_{2,3}$ edges," Phys. Rev. B **49**, 16283–16288 (1994).

[11] G. Doolen and D. A. Liberman, "Calculations of photoabsorption by atoms using a linear response method," Phys. Scripta **36**, 77–79 (1987).

[12] F. R. Bartsch, H. G. Birken, C. Kunz, and R. Wolf, "Reflectance and total photoelectric yield measurements of silicon wafers in the XUV spectral range," Semicond. Sci. Technol. **5**, 974–979 (1990).

[13] D. W. Lynch and W. R. Hunter, "Optical constants of metals," in *Handbook of Optical Constants of Solids*, E. D. Palik, ed., (Academic Press, San Diego, 1985), pp. 303–313.

[14] J. H. Weaver, D. W. Lynch, and C. G. Olson, "Optical properties of V, Ta, and Mo from 0.1 to 35 eV," Phys. Rev. B **10**, 501–516 (1974).

[15] D. W. Juenker, L. J. LeBlanc, and C. R. Martin, "Optical properties of some transition metals," J. Opt. Soc. Am. **58**, 164–171 (1968).

[16] D. L. Windt, J. W. C. Cash, M. Scott, P. Arendt, , B. Newnam, R. F. Fisher, and A. B. Swartzlander, "Optical constants for thin films of Ti, Zr, Nb, Mo, Ru, Rh, Pd, Ag, Hf, Ta, W, Re, Ir, Os, Pt, and Au from 24 Å to 1216 Å," Appl. Opt. **27**, 246–278 (1988).

[17] D. L. Windt, "XUV Optical constants of single-crystal GaAs and sputtered C, Si, Cr_3C_2, Mo, and W," Appl. Opt. **30,** 15–25 (1991).

[18] D. L. Windt, Lucent Technologies - Bell Laboratories, unpublished measurements, 1992.

[19] E. T. Arakawa, T. A. Callcott, and Y.-C. Chang, "Beryllium (Be)," in *Handbook of Optical Constants of Solids II*, E. D. Palik, ed., (Academic Press, San Diego, 1991), pp. 421–433.

[20] B. L. Henke and R. L. Elgin, "X-ray absorption tables for the 2-to-200 Å region," In *Advances in X-ray Analysis*, B. L. Henke, J. B. Newkirk, and G. R. Mallett, eds., pp. 639–665 (Plenum, London, UK, 1970), conference on Advances in X-ray Analysis, Denver, CO, 6-8 August 1969.

[21] M. A. Barstow, M. Lewis, and R. Petre, "Linear absorption coefficient of beryllium in the 50 - 300 Å wavelength range," J. Opt. Soc. Am. **73,** 1220–1222 (1983).

[22] J. H. Underwood, "X-ray optics," American Scientist **66,** 476–486 (1978).

[23] J. H. Underwood and T. W. Barbee, Jr., "Layered synthetic microstructures as Bragg diffractors for x-rays and extreme ultraviolet: theory and predicted performance," Appl. Opt. **20,** 3027–3034 (1981).

[24] J. H. Underwood and D. T. Attwood, "The renaissance of x-ray optics," Physics Today pp. 44–51 (1984).

[25] S. Bajt, R. D. Behymer, M. Wall, C. Montcalm, S. P. Vernon, F. J. Weber, F. R. Grabner, and J. A. Folta, "Mo/Be multilayer mirrors for extreme ultraviolet lithography," In *Tech. Digest, The 4th International Conference on The Physics of X-Ray Multilayer Structures, Breckenridge, CO, March 1-5, 1998*, (1998), to be presented.

[26] T. W. Barbee, Jr., S. Mrowka, and M. C. Hettrick, "Molybdenum-silicon multilayer mirrors for the extreme ultraviolet," Appl. Opt. **24,** 883–886 (1985).

[27] E. M. Gullikson, *http://www-cxro.lbl.gov/optical_constants*, currently available on the World Wide Web.

[28] D. F. Edwards, "Silicon (Si)," in *Handbook of Optical Constants of Solids*, E. D. Palik, ed., (Academic Press, San Diego, 1985), pp. 547–569.

[29] M. Altarelli and D. Y. Smith, "Superconvergence and sum rules for the optical constants: Physical meaning, comparison with experiment, and generalization," Phys. Rev. B **9,** 1290–1298 (1974).

[30] D. Y. Smith and J. H. Barkyoumb, "Sign reversal of the atomic scattering factor and grazing-incidence transmission at x-ray-absorption edges," Phys. Rev. B **41,** 11529–11535 (1990).

[31] F. Stern, "Elementary Theory of the Optical Properties of Solids," in *Solid State Physics, Vol. 15* (Academic Press, 1963), pp. 299–408.

[32] L. Névot and P. Croce, "Caractérisation des surfaces par réflexion rasante de rayons X. Application à l' étude du polissage de quelques verres silicates," Revue Phys. Appl. **15,** 761–779 (1980).

[33] S. V. Pepper, "Optical Analysis of Photoemission," J. Opt. Soc. Am **60,** 805–812 (1970).

[34] H.-G. Birken, C. Blessing, and C. Kunz, "Determination of Optical Constants from Angular-Dependent Photoelectric-Yield Measurements," in *Handbook of Optical Constants of Solids II*, E. D. Palik, ed., (Academic Press, San Diego, 1991), Chap. 12, pp. 279–292.

[35] F. Wooten, *Optical Properties of Solids* (Academic Press, New York, 1972).

[36] L. Kissel and R. H. Pratt, "Corrections to Tabulated Anomalous-Scattering Factors," Acta Cryst. **46,** 170–175 (1990).

[37] D. Y. Smith, "X-ray optical properties: A review of the constraints and the data base," In *Proc. SPIE, X-Ray and VUV Interaction Data Bases, Calculations,*

and Measurements, Los Angeles, CA, 14-15 January 1988, D. Grande, N. Kerr, P. Lee, J. A. R. Samson, and D. Y. Smith, eds.,**911**, 86–99 (1988).

[38] L. D. Landau and E. M. Lifshitz, in *Electrodynamics of Continuous Media* (Pergamon, Oxford, England, 1960), p. 261.

[39] M. Altarelli, D. L. Dexter, H. M. Nussenzveig, and D. Y. Smith, "Superconvergence and sum rules for the optical constants," Phys. Rev. B **6**, 4502–4509 (1972).

[40] T. Takahagi, I. Nagai, A. Ishitani, and H. Kuroda, "The formation of hydrogen passivated silicon single-crystal surfaces using ultraviolet cleaning and HF etching," J. Appl. Phys. **64**, 3516–3521 (1988).

[41] M. C. Thornton and R. H. Williams, "A photoemission study of passivated silicon surfaces produced by etching in solutions of HF," Semicond. Sci. Technol. **4**, 847–0000 (1989).

[42] M. C. Thornton and R. H. Williams, "An S/XPS study of hydrogen terminated, ordered silicon (100) and (111) surfaces prepared by chemical etching," Physica Scripta **41**, 1047–1052 (1990).

[43] M.-T. Tang, K. W. Evans-Lutterodt, G. S. Higashi, and T. Boone, "Roughness of the silicon (001)/SiO_2 interface," Appl. Phys. Lett. **62**, 3144–3146 (1993).

[44] G. S. Higashi, R. S. Becker, Y. J. Chabal, and A. J. Becker, "Comparison of Si(111) surfaces prepared using aqueous solutions of NH_4F versus HF," Appl. Phys. Lett. **58**, 1656–1658 (1991).

[45] R. W. C. Hansen, J. Wolske, D. Wallace, and M. Bissen, "Cleaning of optical surfaces with photogenerated reactants," Nuclear Instrum. Methods A **347**, 249–253 (1994).

[46] Perkin-Elmer Corporation, Physical Electronics Division, 6509 Flying Cloud Drive, Eden Prairie, Minnessota 55344.

[47] *Handbook of X-ray Photoelectron Spectroscopy*, Perkin-Elmer Corporation, 1978.

[48] A. F. Carley and M. W. Roberts, "An X-ray photoelectron spectroscopic study of the interaction of oxygen and nitric oxide with aluminium," Proc. R. Soc. London Ser. A **363**, 403–424 (1978).

[49] C. J. Powell and M. P. Seah, "Precision, accuracy and uncertainty in quantitative surface analyses by Auger-electron spectroscopy and x-ray photoelectron spectroscopy," J. Vac. Sci. Technol. A **8**, 735–763 (1990).

[50] F. J. Himpsel, F. R. McFeely, A. Taleb-Ibrahimi, and J. A. Yarmoff, "Microscopic structure of the SiO_2/Si interface," Phys. Rev. B **38**, 6084–6096 (1988).

[51] Y. Kunii, M. Tabe, and Y. Sakakibara, "Effects of substrate-surface cleaning on solid phase epitaxial Si films," Jap. Journal of Appl. Phys **20**, 1008–1013 (1987).

[52] W. R. Hunter, "Measurement of optical properties of materials in the vacuum ultraviolet spectral region," Appl. Opt. **21**, 2103–2114 (1982).

[53] C. Gähwiller and F. C. Brown, "Photoabsorption near the $L_{II,III}$ edge of silicon and aluminum," Phys. Rev. B **2**, 1918–1925 (1970).

[54] A. P. Lukirskii and I. A. Brytov, "Investigation of the energy structure of Be and BeO by ultra-soft X-ray spectroscopy," Soviet Physics-Solid State **6**, 33–41 (1964).

[55] R. Haensel, G. Keitel, B. Sonntag, C. Kunz, and P. Schreiber, "Photoabsorption Measurement of Li, Be, Na, Mg, and Al in the XUV Range," Phys. Stat. Sol. **2**, 85–90 (1970).

[56] H. Nagasawa, "Near edge fine structure of Li, Be and graphite by X-ray Raman scattering," Journal de Physique **48**, C9, 863–866 (1987).

[57] H. Nagasawa and S. Mourikis and W. Schülke, "X-Ray Raman Spectrum of Li, Be and Graphite in a High-Resolution Inelastic Synchrotron X-Ray Scattering Experiment," J. Phys. Soc. Japan **58**, 710–717 (1989).

[58] D. Ciarlo, Lawrence Livermore National Lab, personal communication.

M98052324

Report Number (14) LBNL-- 41258

Publ. Date (11) 199712

Sponsor Code (18) DOE/ER, XF

UC Category (19) UC-404, DOE/ER

DOE